

**SATELLITE-BASED FLOOD  
MAPPING FOR HYDRODYNAMIC  
FLOOD MODEL ASSESSMENT:  
ACCRA, GHANA**

REBECCA AMOAH ADDAE

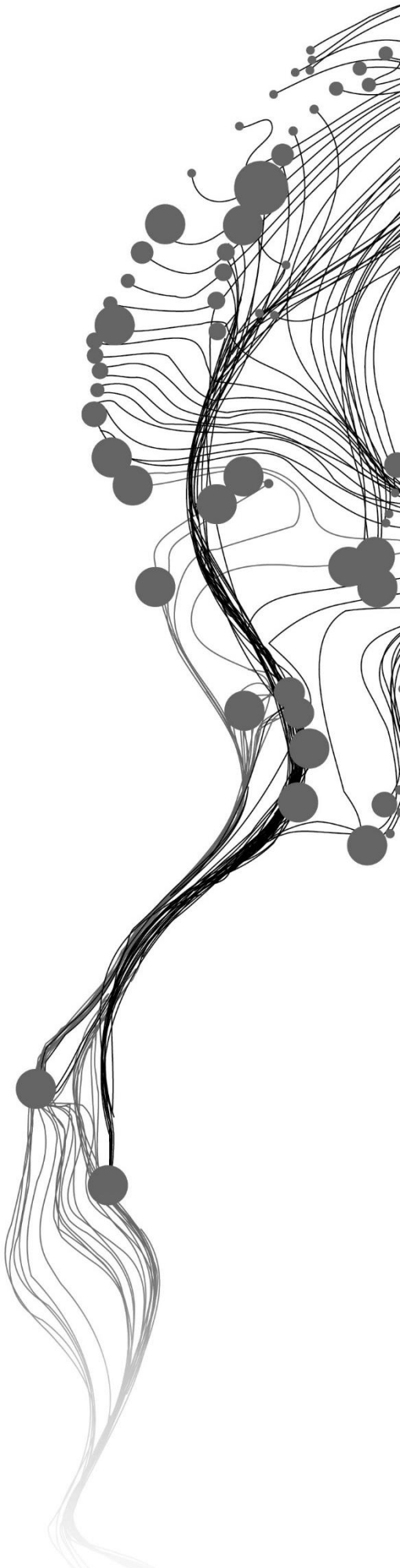
February, 2018

SUPERVISORS:

Dr. Ing. T.H.M. Rientjes

Ir. G.N. Parodi





# **SATELLITE-BASED FLOOD MAPPING FOR HYDRODYNAMIC FLOOD MODEL ASSESSMENT: ACCRA, GHANA**

REBECCA AMOAH ADDAE

Enschede, The Netherlands, February, 2018

Thesis submitted to the Faculty of Geo-Information Science and Earth Observation of the University of Twente in partial fulfilment of the requirements for the degree of Master of Science in Geo-information Science and Earth Observation.

Specialization: Water Resources and Environmental Management

**SUPERVISORS:**

Dr. Ing. T.H.M. Rientjes

Ir. G.N. Parodi

**THESIS ASSESSMENT BOARD:**

Prof. Dr. Z Su (Chair)

Prof. Dr. P. Reggiani (External Examiner, University of Siegen-Germany)

#### DISCLAIMER

This document describes work undertaken as part of a programme of study at the Faculty of Geo-Information Science and Earth Observation of the University of Twente. All views and opinions expressed therein remain the sole responsibility of the author, and do not necessarily represent those of the Faculty.

## ABSTRACT

The urban settlement, downstream of the Densu catchment experience frequent flooding that causes significant damage to people and properties. The flooding is caused by the periodic high and continuous discharge from the Weija reservoir, which is constructed at the south of the Densu catchment. With increasing expansion of settlement area along with the continuous operation of the reservoir, it is essential to understand the hydrodynamic processes of the channel and floodplains. Hydrodynamic modelling can be used to analyse flood impact for mitigation planning. However, in Ghana, data required for the setup and calibration of these models are limited. The objective of the study, therefore, is to analyse the suitability of satellite-based flood extent mapping for hydrodynamic flood model calibration of a data-limited floodplain in Accra. Two sources of satellite images were analysed used for this analysis. They were the Sentinel-1 SAR and PlanetScope optical images. The change detection method of image differencing and ratioing were used to extract inundation information from the Sentinel-1 SAR images. The residual image histograms were segmented using statistical percentile range thresholds, to extract the inundated changes in backscatter from the no change areas. The NDWI was applied to extract inundation from the PlanetScope images. The 1D2D SOBEK hydrodynamic model was set up to simulate the inundation extent of the model domain. The schematized model was tested using 1D steady flow condition to find and correct artefacts in the model setup before the real simulations. The model was run for the flood window determined from the daily discharge time series data. The satellite extracted flood extents were compared with the simulated flood extent to determine the match using the statistical measure of goodness of fit. The results from the Sentinel-1 inundation extraction showed a little advantage of the VV polarisation to detect over the VH polarisation. However, both polarisation in comparison with the simulated inundation showed a low correlation of slightly above 50%. The results revealed that backscatter changes in the densely built-up area were minimal and hardly recognisable. The inundation within the vegetated area along the river was comparatively better detected with the change detection method. The PlanetScope optical image, on the other hand, showed a better correlation between the NDWI extracted inundation and the simulated recording 72% of the goodness of fit. However, inundation, as seen in the comparison map, showed that vegetation hindered the extraction of inundated ponds covered with vegetation and vegetation near the river. A multivariate assessment was lastly performed to assess the goodness of fit between the simulated inundation and the combined satellite inundation of both the SAR and optical. The idea of the multivariate approach was to analyse how the two sources of satellite images would complement each other in inundation detection. The results after the multivariate assessment showed a higher value of goodness of fit of approximately 88%. Overall the study revealed the extent to which inundation can be extracted from satellite images. The results suggested that Sentinel-1 is suitable to effectively extract inundation extent of open water and vegetation inundation and thus could be possible for model calibration setup at such areas. Also, detected PlanetScope optical inundation could serve model calibration in floodplain areas with low vegetation cover and urban areas. The results from the multivariate assessment indicated that the combination of inundation information from different satellite data sources could be suitable for hydrodynamic flood model calibration in data-limited areas.

**Keywords:** Sentinel-1, SAR, SOBEK 1D2D, hydrodynamic modelling, NDWI, change detection, inundation extent, Accra

## ACKNOWLEDGEMENTS

My utmost thanks to Jehovah for His grace, love and protection throughout my stay in the Netherlands. I give Him all the glory.

I would like to thank the Government of the Netherlands for granting me scholarship through the Netherland Fellowship Program (NFP) to pursue my Master of science degree in the Netherlands.

I would like to thank the staff and lecturers of the Faculty of Geo-information Science and Earth Observation (ITC) of the University of Twente, especially, lecturers of WREM Department for providing a conducive environment for studies.

I would like to express my deep gratitude to my supervisor Dr Ing. Tom Rientjes for his encouragement and guidance during my fieldwork and his critical comments and support throughout my thesis work. I must say, I learnt a lot from you. Thank you very much, Tom. My sincere thanks to Ir. Gabriel Parodi for your technical support and guidance. I am indeed grateful.

Special thanks to my colleagues and friends at ITC for their great company throughout my stay in Enschede.

I would like to thank the workers of GCWL for their support during my fieldwork, particularly Mr Paul (site manager), Isaac and Williams for their assistance. I heartily thank Mr Paul Senahu for his support and assistance during my entire fieldwork. I would also like to thank Bright and Evans of SMD for their assistance.

I thank all my friends for their help during my fieldwork, especially Justin Yieri for his complete dedication and assistance

Special thanks to my boss Godwyll Quansah of HydroCivil, Ghana, for his encouragement and advice.

I am thankful to my family for their support and prayers. I love you all.

Last but not least, special thanks to my beloved husband, Eric Berefo for his love and support throughout my period of study. Thanks so much for assuming the sole responsibility for taking care of our daughter. I am very grateful.

# TABLE OF CONTENTS

---

<b>1. INTRODUCTION.....</b>	<b>7</b>
1.1. BACKGROUND.....	7
1.2. PROBLEM STATEMENT.....	8
1.3. OBJECTIVE.....	9
1.3.1. Specific Objectives.....	9
1.4. RESEARCH QUESTIONS.....	9
1.5. THESIS OUTLINE.....	9
<b>2. LITERATURE REVIEW.....</b>	<b>10</b>
2.1. OPTICAL REMOTE SENSING BASED FLOOD MAPPING.....	10
2.2. SAR INUNDATION MAPPING.....	10
2.3. HYDRODYNAMIC FLOOD MODELLING.....	12
2.3.1. Topographical Representation.....	12
2.3.2. Land cover Representation.....	13
2.3.3. Boundary Conditions.....	14
2.4. SATELLITE INUNDATED EXTENTS FOR MODEL CALIBRATION.....	14
<b>3. STUDY AREA AND DATASET.....</b>	<b>15</b>
3.1. STUDY AREA.....	15
3.1.1. The Model Domain.....	15
3.2. DATASETS.....	16
3.2.1. Remote Sensing Data.....	16
3.3. FIELDWORK AND DATA PROCESSING.....	18
3.3.1. Reservoir Water Level and Discharge Data.....	18
3.3.2. River Cross-Section.....	18
3.3.3. Mean Velocity and Discharge Calculations.....	19
3.3.4. Topographic Data.....	20
<b>4. METHODOLOGY.....</b>	<b>22</b>
4.1. SENTINEL-1 IMAGE PROCESSING.....	22
4.1.1. Sentinel-1 Image Pre-processing.....	22
4.1.2. Sentinel-1 Inundation Mapping.....	24
4.1.3. PlanetScope Flood Detection.....	26
4.2. DEM VALIDATION AND ENHANCEMENT.....	26
4.2.1. Accuracy Assessment.....	27
4.3. HYDRODYNAMIC FLOOD MODELLING.....	28
4.3.1. SOBEK Model Setup and Schematization.....	28
4.4. INUNDATION EXTENT COMPARISON AND ASSESSMENT.....	34
<b>5. RESULTS AND DISCUSSION.....</b>	<b>35</b>
5.1. SENTINEL-1 SAR FLOOD EXTRACTION.....	35
5.1.1. Verification of Backscatter Changes from Histogram Segmentations.....	37
5.1.2. Segmentation for Inundation Extent.....	38
5.1.3. Results of Sentinel-1 SAR Flood Detection.....	39
5.2. FLOOD DETECTION FROM PLANETSCOPE IMAGES.....	40
5.3. DEM ACCURACY ASSESSMENT.....	42
5.3.1. DEM Enhancement.....	44
5.4. MODEL SET-UP AND RESULTS.....	44
5.4.1. Model Testing.....	44
5.4.2. Boundary conditions.....	48

5.4.3.	Sensitivity Analysis.....	49
5.4.4.	Model Results .....	50
5.5.	COMPARISON OF MODEL RESULTS AND SATELLITE DATA.....	53
5.5.1.	Multivariate Assessment .....	57
5.5.2.	Possible causes of misfit .....	58
<b>6.</b>	<b>CONCLUSION AND RECOMMENDATION .....</b>	<b>59</b>
6.1.	CONCLUSION.....	59
6.2.	RECOMMENDATION .....	61



## LIST OF FIGURES

---

Figure 2-1: Backscattering characteristics of land cover surfaces (source: Martinis et al. (2015))	11
Figure 2-2: Building representations effect on model simulation (Manyifika 2015)	13
Figure 3-1: Map showing the Densu catchment and the selected model domain	15
Figure 3-2: The topography, slope, aerial photo and land cover of the model domain	16
Figure 3-3: Graphs of the daily reservoir water level and the Stage and Discharge curve of two gates at 1ft gate opened width	18
Figure 3-4: Fieldwork picture of the river cross-section measurement and a sketch of the cross-section	19
Figure 3-5: Guide to conduct a float method of velocity calculation (Michaud & Wierenga, 2005)	19
Figure 3-6: GPS Survey work a) Base setup b) Spot height measurement c) Reference benchmark	20
Figure 3-7: Digital contours and survey points showing the reference stations	20
Figure 4-1: Flowchart of the Sentinel-1 flood extraction	22
Figure 4-2: Visual comparison of results of speckle filtering techniques	24
Figure 4-3: Cross-sectional profiles of the river width	25
Figure 4-4: Flowchart of DEM validation and error assessment	27
Figure 4-5: Flowchart of the hydrodynamic flood modelling and inundation comparison	28
Figure 4-6: Staggered grid of SOBEK flow model (source: (Deltares, 2017))	29
Figure 4-7: 1D2D model schematization (Source: (Deltares, 2017))	29
Figure 4-8: 1D and 2D schematization of the model domain	30
Figure 4-9: Manning's roughness coefficient of land cover classes	33
Figure 5-1: RGB view of Sentinel-1 images and residual images after the application of the difference and ratio algorithms	35
Figure 5-2: Histograms of the difference and ratio residual images	36
Figure 5-3: Verification analysis of segmented results for Weija reservoir	37
Figure 5-4: Area of inundation after segmentation	38
Figure 5-5: Inundation extend generated from the percentile threshold ranges	39
Figure 5-6: Inundation extent of the VH and VV polarisations of 07/07/2017	40
Figure 5-7: NDWI map of 25/06/2017	41
Figure 5-8: Flood maps of 25/06/2017 and 14/07/2017	42
Figure 5-9: Pixel-based elevation difference maps of the of the GPS Survey locations	43
Figure 5-10: Frequency distribution and statistical summary of the elevation differences	43
Figure 5-11: Hillshade maps of the original contour DEM and the enhanced DEM	44
Figure 5-12: Netter view and longitudinal view of simulated 1D steady flow showing the uncorrected cross-section level	45
Figure 5-13: Corrected channel bed level	45
Figure 5-14: Simulated water level of 50m <sup>3</sup> /s steady flow and (left) location of nodes and segments analysed	46
Figure 5-15: Discharge graph of 1D steady flow simulation analysis	46
Figure 5-16: Graph of water level of nodes connected at the connection node	47
Figure 5-17: Graph showing the response of the model to 1D unsteady flow test	47
Figure 5-18: Cumulative curves of daily reservoir discharge and rainfall of the study area	48
Figure 5-19: Reservoir daily discharge showing the flood window	48
Figure 5-20: Graphical representation of the sensitivity analysis	50
Figure 5-21: Simulated flood extent on the 25/06/2017 (18:00:00)	51
Figure 5-22: Simulated flood extent on the 07/07/2017 (18:00:00)	52
Figure 5-23: Simulated flood extent on the 14/07/2017 (08:00:00)	52
Figure 5-24: Comparison maps of Sentinel-1 and model simulated flood extent (25/06/2017)	55
Figure 5-25: Comparison maps of Sentinel-1 and model simulated flood extent (07/07/2017)	56
Figure 5-26: Comparison maps of PlanetScope and simulated model extent (25/06/2017)	57
Figure 5-27: Comparison map of the multivariate assessment of satellite and model simulated inundation	57

## LIST OF TABLES

---

Table 3-1: The specification of the Sentinel-1 images downloaded.....	17
Table 3-2: Image description of downloaded PlanetScope images.....	17
Table 3-3: PlanetScope product description (source: (Planet Labs, 2017)).....	18
Table 3-4: Float method velocity calculation.....	19
Table 4-1: Statistical measures for DEM error assessment.....	27
Table 4-2: Model parameter and ranges for sensitivity analysis.....	32
Table 4-3: Manning's roughness coefficient adapted from Medeiros et al. (2012).....	33
Table 4-4: Statistical measure for inundation extent comparison adapted from Grimaldi et al.(2016).....	34
Table 5-1: Statistical comparison of the satellite data and simulated results.....	54

# 1. INTRODUCTION

## 1.1. Background

Over the past decades, the urban areas in the downstream part of the Densu catchment experience recurrent flooding that caused significant damage to people and properties. The causes of the frequent floods include improper settlement planning, floodplain encroachment and effects of climate change (Amoako & Boamah, 2015; Asumadu-Sarkodie et al., 2015). Moreover, the construction of the Weija reservoir has altered the direct flow of the Densu river to the sea. Instead, the discharges are controlled and periodically released into the Densu river to the sea to maintain the structural stability of the reservoir (WRC, 2007). The periodic discharges from the Weija reservoir more often than not result in a downstream urban flood. Consequently, residents evacuate from their homes while floods cause damage to their houses and properties. Frick-Trzebitzky & Bruns (2017) noted that settlements and urbanisation in the low laying, floodplain areas such as the Densu floodplains and Delta are prohibited in Ghana. However, due to the ineffective urban policy implementation, encroachment in these areas have rapidly increased over the years.

With expanding development of settlement zone alongside the continuous operation of the reservoir, it is essential to understand the hydrodynamic processes of the floodplains and water management structures to reduce flood impact. For that reason, 1D2D<sup>1</sup> hydrodynamic flood inundation models can be employed to simulate flood scenarios before reservoir discharges for flood risk monitoring and mitigation planning (Mani et al., 2014). However, in Ghana, little attention is paid to the collection of flood and hydrometric information for flood impact assessment and hydrodynamic modelling. As a consequence, most gauge stations are not well maintained or monitored, and also, destroyed gauges are hardly replaced. Other floodplain information including channel geometry, high-resolution DEM<sup>2</sup> and the extent of historical flood event are unavailable. This information is key elements to setting up and calibrating hydrodynamic models (Huang et al., 2015).

Hydrodynamic models help to understand the flow dynamics within the floodplains, as well as to simulate flood scenarios for evaluation of water management structures (Morales-Hernández et al., 2014). Inadequate representation of hydrometric data, topographic information and river flow characteristics is a significant limitation to the application of hydrodynamic models. Therefore, to improve the above limitation, many researchers have exploited the application of satellite observations to serve as observed inundation extent for model calibration (Mason et al., 2007; Grimaldi et al., 2016; Clement et al., 2017).

Satellite remote sensing observation is known to have an extensive spatial coverage and cost-effective, which is advantageous for large scale flood mapping. In the past decades, inundation extents have been mapped using either passive or active remote sensing techniques. For instance, the use of water indices such as NDWI<sup>3</sup> and MNDWI<sup>4</sup> distinguish open water surfaces from other land cover types in optical remote sensing (Xu, 2006; Craciunescu et al., 2010). However, the inability of optical sensors to penetrate clouds limits the use of optical remote sensing in areas with persistent cloud cover for flood monitoring (Manavalan, 2017).

---

<sup>1</sup> One Dimensional Two Dimensional

<sup>2</sup> Digital Elevation Model

<sup>3</sup> Normalised Difference Water Index

<sup>4</sup> Modified Normalised Difference Water Index

On the other hand, SAR<sup>5</sup> remote sensing (an example of active remote sensing) has the capability of penetrating clouds, day and night observation and operate in all-weather conditions (Malinowski et al., 2017). Recent advances in SAR remote sensing have facilitated investigation of SAR flood monitoring and risk assessment. The low backscatter intensity of calm water bodies, as compared to other non-water surfaces, offers the ability to separate flooded areas (i.e. inundated) from non-flooded areas. Although the SAR inundation mapping is a well-appraised method, the detection of vegetation and urban inundation are not straightforward. The backscatter intensities of these land cover types may differ from the above premise due to the effect of underlying water (Refice et al., 2014). This deviation complicates the separation of some flooded land cover (such as vegetation and urban areas) from SAR images.

Despite the difficulties associated with satellite flood detection, researchers continue to evaluate its usability for inundation mapping to complement hydrodynamic models in scarce data regions (Refice et al., 2014; Schumann et al., 2015). The availability of freely accessible satellite data such as Landsat and Sentinel-2 optical images and also, Sentinel-1 SAR data from ESA<sup>6</sup> have increased the application of satellite inundation mapping of passive and active remote sensing. Moreover, authors including Montanari et al. (2009) and Grimaldi et al. (2016) have shown commending results with the use of satellite-derived flood extent for the calibration and validation of hydrodynamic models in limited data basins.

The Densu catchment lacks the adequate hydrometric information necessary for effective hydrodynamic flood modelling. Hence the need to analyse the usability of satellite observations to serve as surrogate data for hydrodynamic model calibration. This approach has rarely been investigated in Accra, Ghana. Therefore, this research seeks to investigate whether satellite-based flood extent is viable for the calibration of the 1D2D SOBEK hydrodynamic model in the Densu floodplains.

## **1.2. Problem Statement**

Hydrodynamic models can be used to simulate flood scenarios and devise water management strategies to avert flood re-occurrences in the highly populated urban area of the Densu catchment. Data limitation is a major problem to the set-up and calibration of hydrodynamic models. Moreover, since little attention is given to the acquisition of flood information for hydrodynamic modelling assessment in Ghana, it is essential to explore alternative data sources which could serve as a substitute for observed flood extent.

In recent years, researchers have investigated the use of satellite inundation extent as cost-effective and a viable substitute for calibration of hydrodynamic flood modelling (Schumann et al., 2009; Stephens et al., 2012; Manavalan, 2017). Optical and SAR satellite data are the widely used remote sensing data for flood mapping. However, the spatial and temporal resolutions of satellite sensors, atmospheric effects, as well as land cover properties can hinder inundation observation for model calibration. Therefore, it is essential to investigate the appropriateness of satellite inundation to serve for hydrodynamic model calibration in the absence of observed flood extent.

---

<sup>5</sup> Synthetic Aperture Radar

<sup>6</sup> European Space Agency

### **1.3. Objective**

The main objective of this study is to analyse the suitability of satellite-based flood extent mapping for hydrodynamic flood model calibration of the data limited Densu floodplain in Accra.

#### **1.3.1. Specific Objectives**

Specific objectives of this study are to:

- Extract inundation extent from Sentinel-1 SAR (C-band) images in an urban area
- Extract inundation extent from PlanetScope optical images
- Prepare a timeline of daily reservoir discharges and determine window of inundation events
- Set-up 1D2D SOBEK hydrodynamic model for flood extent simulation in a limited data basin
- Compare the extracted satellite flood extent with the simulated inundation extent
- Assess if satellite flood extents can serve for flood model calibration purposes

### **1.4. Research Questions**

The research questions that are addressed in this study are

- To what extent can Sentinel-1 be used to observe inundation extent in a built-up area?
- What water mapping index, is appropriate to map inundation extent from Planetscope images?
- What could be the main driver of the recurrent flooding? And can the driver be quantified?
- How could the inflows and outflows be parameterised in the 1D2D flood model?
- What are the effects of the land cover surface roughness on the flood simulation?
- What measure could serve to assess the match between satellite flood extent and hydrodynamic simulated flood extent?

### **1.5. Thesis Outline**

The outline of this thesis report is made up of six chapters. The first chapter is the introduction of this study which provides the background and problem of this research. The second chapter provides a literature review which reviews methods used in previous studies to address similar research problems identified in this study. The third chapter presents a description of the study area and the available datasets. The fourth chapter presents research methodology. Chapter five provides the results and discussion of the findings of the study. The conclusions of the research and recommendations for future research of similar problems are presented in chapter six.

## 2. LITERATURE REVIEW

Flood mapping is essential for flood mitigation planning and understanding the dynamics of a floodplain. Hydrologists have identified several methods for flood mapping and analysis. Among these methods are the hydrodynamic models and remote sensing observations. Hydrodynamic modelling is suitable for flood forecasting and devising mitigation for areas of recurrent events (Fan et al., 2017). However, this method requires detailed hydrometric data and topographic information, which are hardly available especially in developing countries. Remote sensing approach is a cost-effective method perceived as a viable option for inundation mapping. Due to its consistent observation, remote sensing inundation information has been used in recent studies to complement in-situ data for hydrological and hydrodynamic modelling in scarce data basins (Malinowski & Schwanghart, 2017).

### 2.1. Optical Remote Sensing based flood mapping

Optical remote sensing images are the frequently used data for inundation mapping since optical images are easy to interpret and process for inundation retrieval (Malinowski & Schwanghart, 2017). The inundation interpretation of optical images is performed using standardised indices. In the past two decades, spectral indices have been exploited to separate water pixels from non-water pixels in optical remote sensing. The commonly used indices are the NDWI and MNDWI introduced by McFeeters (1996) and Xu (2006) respectively. The MNDWI index applies to images with the MIR<sup>7</sup> band, whereas the NDWI applies to optical images with NIR<sup>8</sup> band. Nonetheless, both indices follow the same principle, to explain, the reflectance of water in the NIR or MIR is approximately zero while other land cover types show high reflectance in NIR and MIR. For that purpose, the normalised ratio of reflectance of the green and infrared bands present water surfaces as positives (ranging from 0 to +1) and other land covers as negative values (<0 to -1).

However, Xu (2006) established that the application of the NDWI index in built-up areas does not comply with the above premise. He discussed that the reflectance of built-up areas is similar to water reflectance. That is to say; both show high reflectance in the green band than in NIR. Even though the NIR reflectance in the built-up area may not be zero like water, the lower NIR reflectance of built-up areas can as well result in positive values. Hence, the extraction of inundated areas could mix with building noise. Thus, extracting flood extent using the NDWI index in a built-up area could mean that low positive values can be classified built-up while higher positive classified as inundated or water surfaces.

### 2.2. SAR Inundation Mapping

In recent times, more attention is focussed on the use of SAR images for inundation mapping, mainly due to the cloud-penetrating advantage over optical images. Unlike optical, inundation extraction from SAR images are quite complicated. There is a need to understand the backscattering characteristics of land cover surfaces to determine the appropriate algorithm to use for inundation extraction. Martinis et al. (2015) illustrated the different scattering characteristics of land surfaces under both dry and flooded conditions as presented in *Figure 2-1*. In fact, the application of SAR inundation mapping is capitalised on these scattering characteristics to classify flooded areas from non-flooded.

---

<sup>7</sup> Middle Infrared

<sup>8</sup> Near Infrared

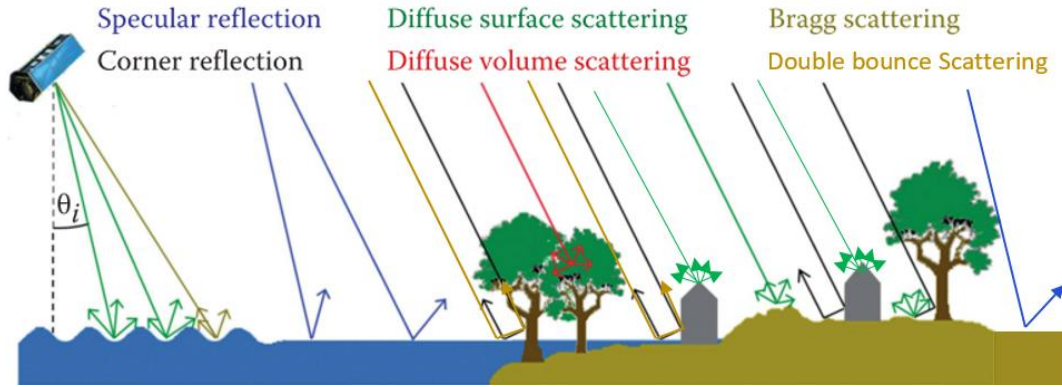


Figure 2-1: Backscattering characteristics of land cover surfaces (source: Martinis et al. (2015))

Amongst the SAR water mapping techniques, histogram thresholding method is the simplest and widely consented method to separate water surfaces from other land cover types (El-Zaart, 2015). The method involved the determination of a threshold value from a SAR image histogram to separate water pixels from non-water pixels through binarisation (Manavalan, 2017). This method often misclassified shadows and layovers caused by the sensor viewing angle and areas of lower backscatter (such as tarmac) as water. Moreover, the histogram thresholding method was unsuccessful to extract flooded vegetation and urban areas from non-flooded areas (Giacomelli et al., 2017). Basically due to the increase in backscatter intensity propelled by the underlying water triggering double bounce reflections and corner reflections as illustrated in Figure 2-1.

The change detection method was developed to overcome the limitation of the histogram thresholding method in SAR inundation detection. The method involved the application of multi-temporal images of the same area (Xiong & Chen, 2012). In essence, the difference in backscatter intensity between the pre and post-flood images were used to identify flood changes within the area of study. There are two change detection approaches for SAR inundation mapping. These are the differencing image algorithm and the image ratio algorithm. In literature, the most frequently used change detection algorithm is the image differencing (Long et al., 2014; Clement et al., 2017; Malinowski & Schwanghart, 2017). Although the ratio algorithm has not been exploited much, Xiong & Chen (2012) emphasised that it is equally simple and easy to apply like the image differencing. According to their study, the ratio algorithm, reduce significant noise in the residual image and increase the distinction between changes and no change areas.

In their study, the threshold for separating changes on the residual image obtained from the change detection (either differencing or ratio) was subjective and unsupervised. Nevertheless, the method of change extraction provided reasonably good results. In the application of inundation mapping, Long et al. (2014) and Clement et al. (2017) have achieved an increase in accuracy of the inundated area with the application of the CDAT<sup>9</sup>.

Also, Long et al. (2014), Martinis et al. (2015) and Hong et al. (2015) applied terrain filtering model (often referred to as HAND<sup>10</sup> model) to reduce the effect of external “noise” on the inundation analysis. The HAND model mask heights of high flood probability to improve the extent of the detected flood. They concluded that flood extent extracted after the application of the HAND model improved the overall accuracy of inundation extraction.

<sup>9</sup> Change Detection and Thresholding

<sup>10</sup> Height Above the Nearest Drainage

In this research, urban flooding in which the similarity of backscatter received by SAR sensors makes it somewhat complicated to distinguish the flooded built-up area from non-flooded. Therefore, based on the successes of earlier studies of a similar problem, the change detection method will be adopted for Sentinel-1 SAR inundation mapping.

### **2.3. Hydrodynamic Flood Modelling**

Previous studies have utilised hydrodynamic modelling to investigate and simulate the impact of floods (e.g. Mani et al., 2014; Patel et al., 2017). With increasing events of urban floods and the urgency to avert the situation, more hydrodynamic models have been developed to incorporate more complex hydrological systems. Over the years, models of 1D, 2D, coupled 1D-2D and 3D<sup>11</sup> have been developed to provide a good representation of channel and floodplain characteristics (Liu et al., 2015). The 1D models performed better when simulating fluvial flooding and are noted for fast computational run time. Hydraulic features like bridges, weirs and sluices are better represented in 1D models (Fan et al., 2017). They asserted that the 1D models inadequately simulated floodplain flow dynamics and characteristics. On the other hand, the 2D model better representation of the lateral flow on floodplains, however computationally intensive. Although the 1D and 2D models have successfully simulated flow characteristics in their respective domains, recent studies have shown a maximised benefits by the coupled 1D2D model, especially in urban flood simulation (Crispino et al., 2015; Fan et al., 2017).

Hydrodynamic models are subject to the 1D, 2D and 1D2D model concepts and the governing equations to simulate flow dynamics in channels and floodplains. The models are designed to implement mass and momentum conservative equations (Deltares, 2017). Moreover, Morales-Hernández et al. (2014) explained in detailed the coupling strategies of linking the 1D and 2D models. They indicated that only mass conservation or both mass and momentum conservations could be imposed between the connecting link of the 1D and 2D models. The strategies determine how water is transfer from the 1D to the 2D, hence very important to simulate the flood dynamics of a floodplain.

Typically, urban floods originate from channels flow to floodplains that makes the 1D2D model as a useful tool, for urban flood modelling. Van Dijk et al. (2014) argued that the coupled 1D2D hydrodynamic model approach give a better flood simulation than the standalone 1D and 2D models. Moreover, other researchers like (Bladé et al., 2012; Mani et al., 2014; Liu et al., 2015; Patel et al., 2017) have analysed the efficiency of the coupled approach for flood modelling. Moreover, in each of these studies, the coupled 1D2D model has shown an advantage over the 1D and 2D for urban flood simulation. Although these researchers have attested the benefits of a 1D2D model for urban inundation modelling, the efficiency of the model is characterised by the accuracy of the input parameters (Rientjes, 2015). Commonly denoted as “garbage-in-garbage-out”. The accurate representation of the input parameters such as the floodplain topography, surface roughness, boundary and initial conditions determines the closeness of the model to real-world characteristics.

#### **2.3.1. Topographical Representation**

Topographical representation in the form of DEM is an essential input in 2D hydrodynamic modelling. The method of topographical data acquisition often determines the degree of uncertainties introduced. The ground survey is perceived to be a very accurate method for topographical data acquisition. Other DEM acquisition methods include digital contours, airborne survey (e.g. LiDAR and digital aerial

---

<sup>11</sup> Three Dimensional



photogrammetry) and satellite-based elevation data (e.g. ASTER<sup>12</sup> and SRTM<sup>13</sup>). Most recently, high-resolution topographical data acquisition by UAS<sup>14</sup> has been known to have an accuracy of >10cm (Anders et al., 2013). The accuracy of the DEM generated from the above method can be evaluated by comparing to randomly collected ground survey points (Smith et al., 2006).

The vertical accuracy assessment is necessary to ensure the reliability of the flow representation of the hydrodynamic model flow simulation. In hydrodynamic modelling, the topographical heights represent the hydraulic heads which facilitate water movement across the model domain (Gichamo et al., 2011). Additionally, the flow velocity, direction and extent of inundation are significantly influenced by differences in elevation and slope (Haile & Rientjes, 2005). Besides the vertical accuracy, the DEM resolution can influence the inundation extent simulated by the model. Recent studies by Brandt (2016) and Ali (2016) have discussed the effect of topographical representation on flood model extent simulation. They illustrated that the DEM resolution had a significant effect on the inundation extent and flow dynamics.

**2.3.2. Land cover Representation**

According to Bao et al. (2009), the surface roughness is a sensitive parameter in the hydrodynamic model. The surface roughness determines the resistance to flow in the model domain. Hence, careful selection of the roughness parameters is crucial to minimise uncertainties to the flow and flood accumulation. However, Shepherd et al. (2011) emphasized that there is no definitive method for correct measurement of roughness values. Modellers have therefore estimated friction values explicitly from biophysical variables (through field experiments) and made available for different land cover types (Smith et al., 2006; Medeiros et al., 2012).

The roughness parameters result significantly in the depth and extent of inundation simulated. This assertion was affirmed by the studies of Haile & Rientjes (2005), Manyifika (2015) and Ali (2016). For instance, Manyifika (2015) conducted a test of building roughness parameter with reference to Haile & Rientjes (2005), and the results as shown in *Figure 2-2* displays high variability in inundation for three building representations. Consequently, high roughness resulted in higher flood depths and a small area of inundation, while lower friction value led to lower flood depths and larger inundated area.

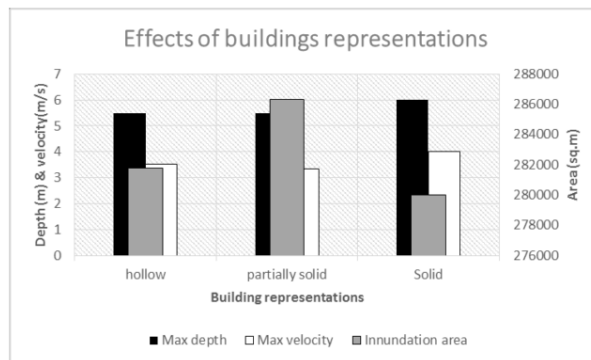


Figure 2-2: Building representations effect on model simulation (Manyifika 2015)

<sup>12</sup> Advanced Spaceborne Thermal Emission and Reflection Radiometer  
<sup>13</sup> Shuttle Radar Topography Mission  
<sup>14</sup> Unmanned Aerial Systems

### 2.3.3. Boundary Conditions

In hydrodynamic modelling, part of the real world, bounded in space and time is simulated. The hydrological influences at the inflow and outflow of the model domain are mathematically represented as the boundary conditions to the model setup (Rientjes, 2015). The boundary conditions like other modelling parameters have an effect on the model output. For example, a sensitivity analysis of boundary conditions analysed by Ali (2016), showed an increase of the downstream boundary condition propagated error to as far as 450m in the model domain. In a like manner, he investigated the effect of the upstream boundary condition and realised an exponential increase in maximum flood depth and inundation area. This study confirmed an earlier analysis made by Alemseged & Rientjes (2007).

In modelling areas where the downstream boundary condition is not available, the selection is often based on a priori knowledge of the hydrological conditions of the modelled area (Marcinkowski & Olszewski, 2014). Several methods exist in literature to impose a boundary condition to a model domain. Among these are the Dirichlet condition (specified head boundary), Neumann condition (no flow boundary), and Cauchy condition (head-dependent flow boundary) explained in the lecture notes of Rientjes (2015). In this study, the hydrodynamic model is set up in a limited data area. The outflow data of the model domain is not available. Therefore, the Dirichlet boundary condition would be adopted for the modelling setup.

## 2.4. Satellite Inundated Extents for Model Calibration

Model calibration is performed by fine-tuning the simulated model data to replicate the observed data. The model calibration can be achieved by adjusting the model parameters and modifying the concepts (Rientjes, 2015). Mostly, observed data is used in the model calibration processes. However, in remote and data limited areas, this approach is hardly possible. The urgency to model and understand the impacts of flooding in these areas has increased the optimism to using remote sensing observations as surrogate data. In reference to this notion, many authors including Di Baldassarre et al. (2011), Grimaldi et al. (2016) and Teng et al. (2017) have described the hydrological and hydrodynamic modelling as traversing from data-poor to data-rich sciences.

Nevertheless, several studies in the past years, have investigated the uncertainties associated with the application of satellite observed inundation extents for hydrodynamic model calibration. Grimaldi et al. (2016) reviewed several satellite remote sensing technologies for inundation mapping and their use for hydrodynamic model calibration and validation. They emphasised that the efficient use of the remote sensing inundation data was challenged by factors including image resolution, the frequency of acquisition and the processing algorithms used. In recent times researchers continue to evaluate the extent to which satellite-based flood (i.e. both SAR and optical) extent could serve for hydrodynamic model calibration. For example, Di Baldassarre et al. (2009) applied flood extent derived from different sets of SAR data (i.e. ENVISAT ASAR<sup>15</sup> and ERS-2<sup>16</sup> SAR) to calibrate a hydrodynamic model of River Dee inundation modelling in the United Kingdom. Likewise, Karim et al. (2011) achieved satisfactory results by using flood extents generated from a set of optical satellite images for hydrodynamic calibration. In the same fashion, Sentinel-1 SAR data and PlanetScope optical images would for analysed whether it could be used for hydrodynamic model calibration.

---

<sup>15</sup> Environmental Satellite Advanced Synthetic Aperture Radar

<sup>16</sup> European Remote Sensing Satellite 2

### 3. STUDY AREA AND DATASET

#### 3.1. Study Area

The Densu catchment is one of the coastal catchments of Ghana. The Densu River catchment covers an area of about 2,600 km<sup>2</sup> and spreads across the Greater Accra and Eastern regions as shown in *Figure 3-1*. The catchment is geographically located between latitudes 5°30'N to 6°17'N and longitudes 0°10'W to 0°37'W. The topography is characterised by highlands to the north and low and flatlands towards the south, where the study was concentrated. The catchment is bordered to the south by the Densu delta, salt lagoon and the sea (WRC, 2007). The Densu River is the main river of the catchment and has a total length of about 120 km. The outstanding feature of this catchment is characterised by the Weija reservoir, located at the south of the catchment and thus intercepting the free flow of the Densu river. The reservoir was constructed to store water for potable water supply and irrigation purposes. The GWCL<sup>17</sup> is the operator of the reservoir and primarily controls the storage and outflow of the reservoir.

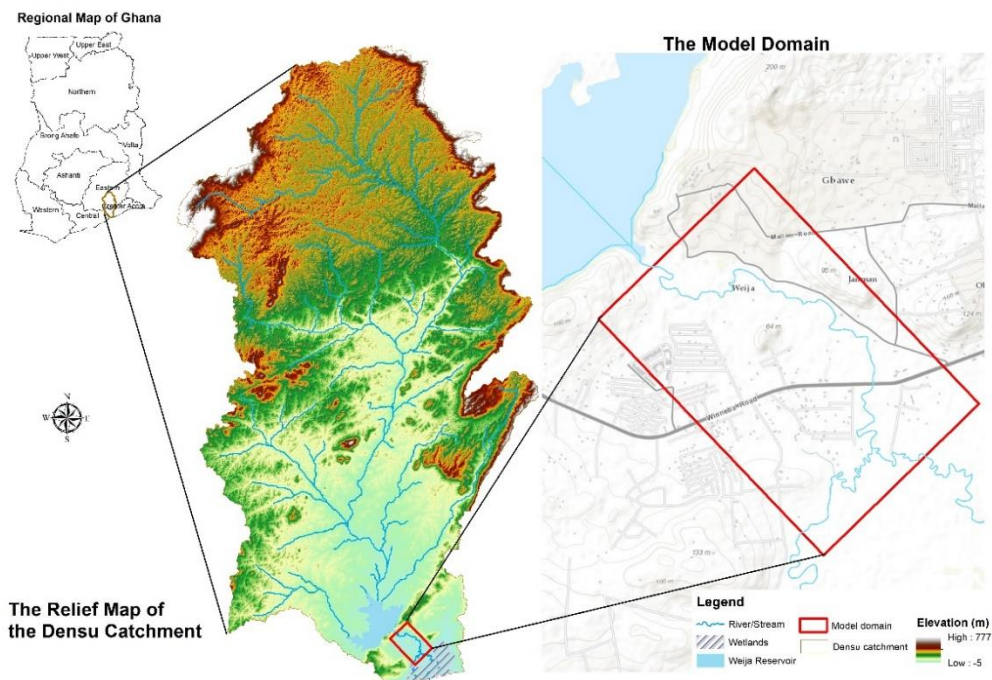


*Figure 3-1: Map showing the Densu catchment and the selected model domain*

##### 3.1.1. The Model Domain

The study was concerned with the frequent floods occurring at the low and flat land areas of the Densu catchment. Accordingly, the model domain was selected to cover a section of the flood-prone area of about 15km<sup>2</sup> as shown in *Figure 3-1*. As stated above, the topography of the selected domain is low land, and the elevation varies between less than 2m to and 130m above sea level. The slope varies from 0 to 56 degrees, with about 90% below 2.5 degrees. The land cover is predominantly a built-up with patches of open forest and shrubs along the river banks. The topographical representation, slope, aerial photograph and land cover of the model domain are shown in *Figure 3-2*.

<sup>17</sup> Ghana Water Company Limited

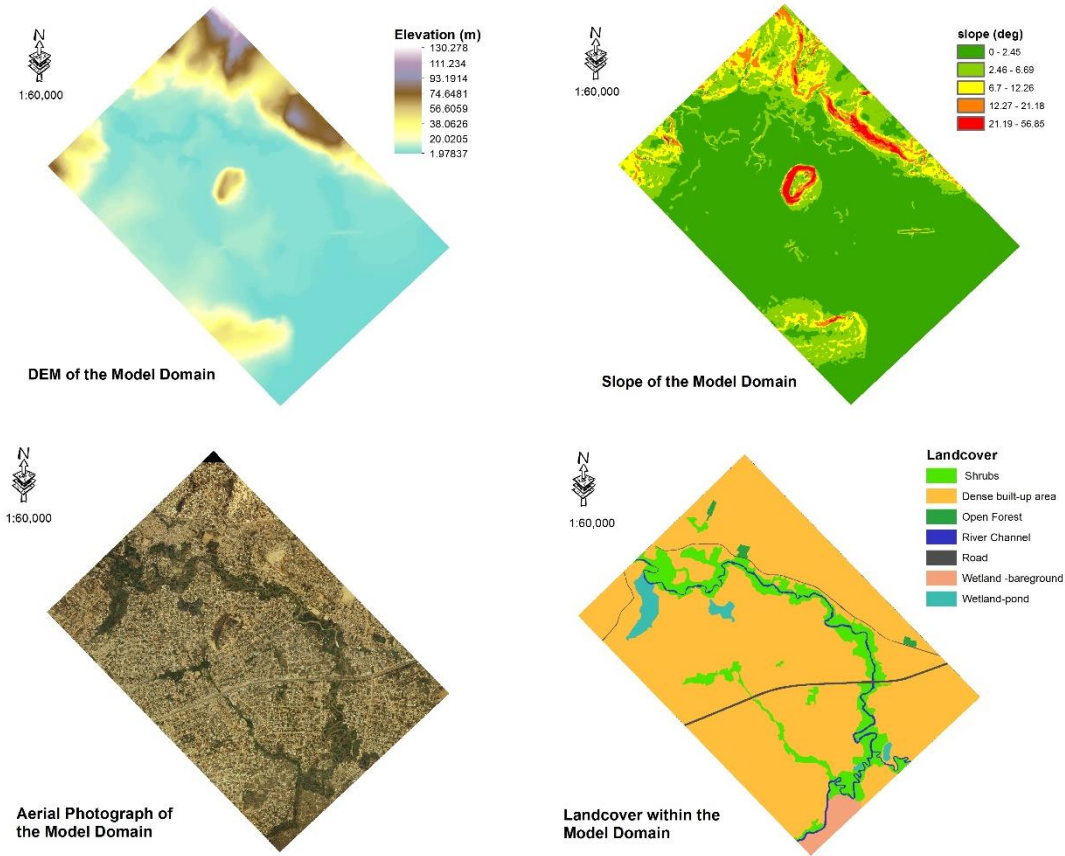


Figure 3-2: The topography, slope, aerial photo and land cover of the model domain

## 3.2. Datasets

Three types of datasets were used in the study, and these were i) the satellite remote sensing data (i.e. Sentinel-1 SAR images and PlanetScope optical images), ii) hydrometric of the reservoir water levels and discharge information and iii) the topographical data of the floodplain and river cross-sectional measurements. Details of the downloaded satellite images are provided in *sub-section 3.2.1*. The second and third datasets were attained during the fieldwork for the setup of 1D2D SOBEK hydrodynamic model.

### 3.2.1. Remote Sensing Data

#### 3.2.1.1. Sentinel-1 SAR Data

Sentinel-1 SAR C-band (5.4GHz) images were downloaded from the *Copernicus Open Access Hub* published by the European Space Agency (ESA) through the link (<https://scihub.copernicus.eu/dhus/>). The IW<sup>18</sup> Swath mode of 250 km swath, geometric resolution of 5 m x 20 m and single-look was acquired for this research. The IW is described by ESA (2017), as the primary operational mode for land applications. The specification of the Sentinel-1 downloaded images is tabulated in Table 3-1. The period determined for the downloads were centred on the high discharges window indicated in *Figure 5-19*. Sentinel-1 images available were in one pass (i.e. ascending over Ghana). As a result, the image and orbit properties were similar for all downloaded images making them appropriate for the change detection method. A dry image captured on the 26/04/2017 was downloaded as a reference image, in addition to two flooded images captured on the 25/06/2017 and

<sup>18</sup> Interferometric Wide

07/07/2017. The acquisition of the flooded images was based on the defined flood window of the discharge time series.

Table 3-1: The specification of the Sentinel-1 images downloaded

Satellite	Specifications	Year	Acquisition dates	
Sentinel-1	Instrument: <b>SAR-C</b> Mode: <b>IW</b> Acquisition Type: <b>NOMINAL</b> Cycle number: <b>123</b> Format: <b>SAFE</b> Pass direction: <b>ASCENDING</b> Polarizations: <b>VV<sup>19</sup> VH<sup>20</sup></b> Product class: <b>S</b> Product class description : <b>SAR Standard L1 Product</b> Product type: <b>GRD<sup>21</sup></b> Relative orbit(Start): <b>147</b> Relative orbit(Stop): <b>147</b> Incident angle (near): <b>30.8</b> Incident angle (far): <b>46.0</b> Status: <b>ARCHIVED</b>	2017	26/04/2017	Reference image
			25/06/2017 07/07/2017	Flooded image

### 3.2.1.2. Optical Imagery

Optical data considered for the analysis included Landsat and Sentinel-2 but cloud-free images for the period identified for the study was difficult to acquire. What is more, WorldView-2, RapidEye and DigitalGlobe sensors had no images captured within the flood window. PlanetScope images of daily revisit time were made available for free download for 14days after first registration with the site. Luckily, a couple of images (within the flood window) were found to be a suitable option for the study after an extended period of fruitless search of optical images over the study area.

- **PlanetScope images**

The PlanetScope satellite constellation made up of groups of individual satellites of multiple launches and continually improving the on-orbit capacity in the ability to obtain more data. With about 120 satellites in the constellation, PlanetScope can make daily capture of the entire earth surface (Planet Labs, 2017). The Level 3A PlanetScope images were downloaded from the link <https://www.planet.com/explorer>. The Level 3A processed image implied the images were orthorectified, radiometrically and geometrically corrected. The images were projected in UTM<sup>22</sup> map coordinate system. The PlanetScope image is a four (4) band image made up of the visual bands (i.e. Red, Green and Blue) and the Near Infrared band. Table 3-2 and

Table 3-3 show the description of the images downloaded and the PlanetScope product specification respectively.

Table 3-2: Image description of downloaded PlanetScope images

Date	Format	Cloud cover	AOI <sup>23</sup> Coverage
18-6-2017	GeoTiff	85%	Full
25-6-2017		40%	Partial
10-7-2017		75%	Partial
14-7-2017		<10%	Full

<sup>19</sup> Vertical transmitted Vertical received  
<sup>20</sup> Vertical transmitted Horizontal received  
<sup>21</sup> Ground Range Detected  
<sup>22</sup> Universal Transverse Mercator  
<sup>23</sup> Area of Interest

Table 3-3: PlanetScope product description (source: (Planet Labs, 2017))

Product Attribute	Description
<b>Information Content</b>	
Analytic Bands	4-band multispectral image (blue, green, red, near-infrared).
Ground Sample Distance	3.7 m (at reference altitude 475 km)
<b>Processing</b>	
Pixel Size (orthorectified)	3.125 m
Bit Depth	Analytic (DN): 12-bit Analytic (Radiance - W m <sup>-2</sup> sr <sup>-1</sup> μm <sup>-1</sup> ): 16-bit
Geometric Corrections	Sensor-related effects are corrected using sensor telemetry and a sensor model, bands are co-registered, and spacecraft-related effects are corrected using attitude telemetry and best available ephemeris data. Orthorectified using GCPs and fine DEMs (30 m to 90 m posting) to <10 m RMSE positional accuracy.
Positional Accuracy	Less than 10 m RMSE
Radiometric Corrections	<ul style="list-style-type: none"> <li>• Conversion to absolute radiometric values based on calibration coefficients</li> <li>• Radiometric values scaled by 100 to reduce quantization error</li> <li>• Calibration coefficients regularly monitored and updated with on-orbit calibration techniques.</li> </ul>

### 3.3. Fieldwork and Data Processing

#### 3.3.1. Reservoir Water Level and Discharge Data

The safe operating level of the reservoir is 47ft, and the minimum operating level for discharge according to GWCL is 45ft as illustrated in *Figure 3-3 (left)*. 12 years daily reservoir levels were obtained, but, only levels from June to September 2017 had accompanied information on the net gate opening widths for discharge computation. In addition, a stage and discharge curves of the number of gates opened and the net gates opened widths were provided. An example of the stage-discharge curve of two gates opened at 1ft width is shown in *Figure 3-3 (right)*. The reservoir daily discharges were estimated from the stage and discharge equations.

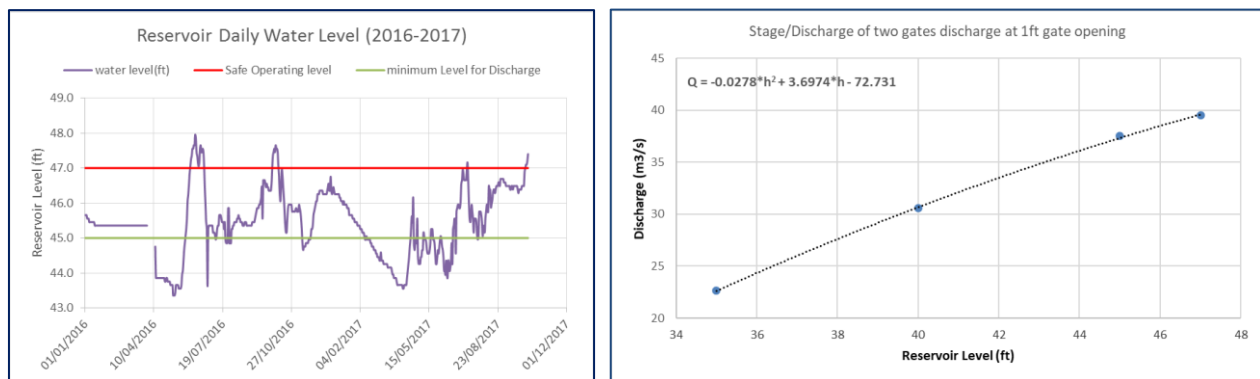


Figure 3-3: Graphs of the daily reservoir water level and the Stage and Discharge curve of two gates at 1ft gate opened width

#### 3.3.2. River Cross-Section

The cross-sectional measurements were essential to estimate discharge and velocity along the river reaches. The river cross-sections were measured during the field work. The measurements were done by gently lowering a utility cord with a metal rod attached to its end to the bottom of the river. The length below the river was marked and measured as demonstrated in *Figure 3-4(left)* and the cross-section sketched as shown in *Figure 3-4(right)*.



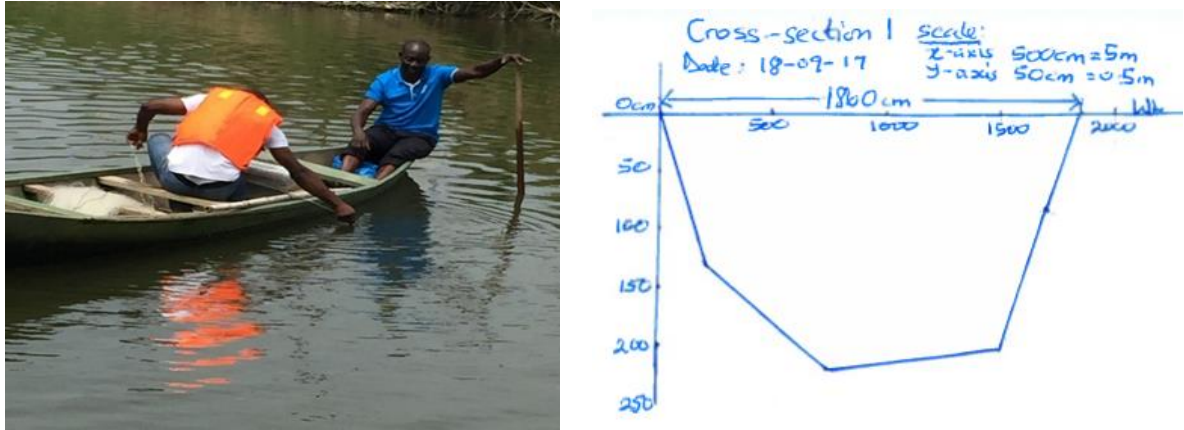


Figure 3-4: Fieldwork picture of the river cross-section measurement and a sketch of the cross-section

### 3.3.3. Mean Velocity and Discharge Calculations

The mean velocity of the river was estimated using the float method as experimented by Michaud & Wierenga (2005) and shown in Figure 3-5. A 5m distance was marked along a section of the river channel and a float thrown to the mid-section of the river. The timer was set to measure the time taken for the float to travel from the marked start point to the exit. The Table 3-4 below shows the measurement taken in the field and the velocity calculated. The discharge the cross-sections were subsequently calculated using the discharge equation (Equation 3-1).

$$Q = v * A \tag{Equation 3-1}$$

Where  $Q$  is the discharge,  $v$  is the mean velocity, and  $A$  is the cross-sectional area.

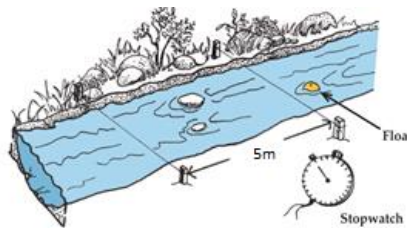


Figure 3-5: Guide to conduct a float method of velocity calculation (Michaud & Wierenga, 2005)

Table 3-4: Float method velocity calculation

Distance (m)	Time (s)	Velocity (m/s)
5	26	0.19
5	27	0.19
5	27	0.19
5	28	0.18

### 3.3.4. Topographic Data

The SMD<sup>24</sup> Ghana provided a 2m interval digital contours of the study area (see *Figure 3-7*). This method of DEM generation is proven to have the potential for high accuracies (Smith et al. 2006). In addition, an RTK<sup>25</sup> GPS<sup>26</sup> as shown in *Figure 3-6* survey was conducted during the fieldwork to i) assess the quality of the DEM and ii) to enhance the height differences at the flood-prone areas. Approximately 1000 cross-sectional points and spot heights were measured. The cross-sectional points were measured within a distance of 100m across the banks of the river at intervals ranging from 10 to 20m.



Figure 3-6: GPS Survey work a) Base setup b) Spot height measurement c) Reference benchmark

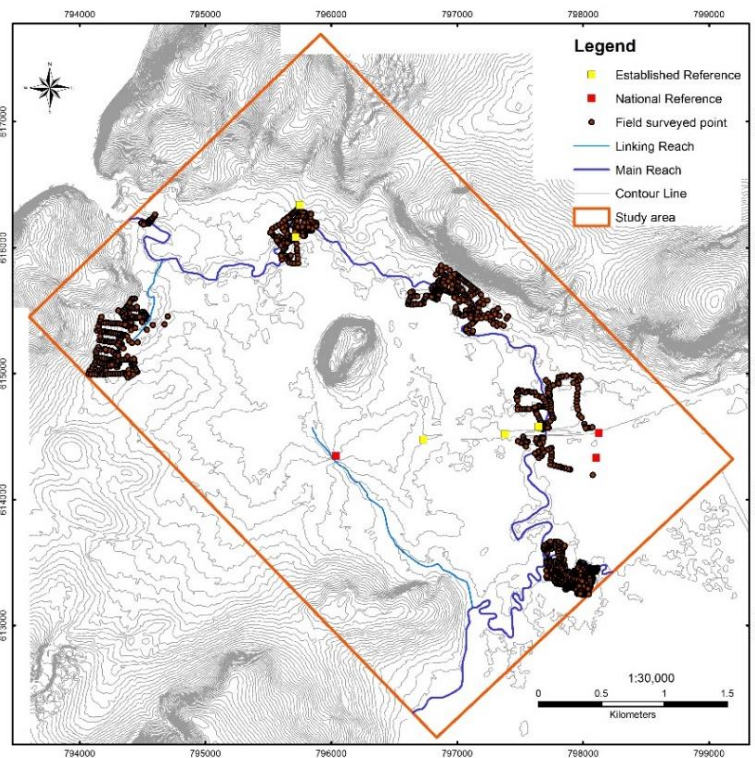


Figure 3-7: Digital contours and survey points showing the reference stations

<sup>24</sup> Survey and Mapping Department

<sup>25</sup> Real-Time Kinematic

<sup>26</sup> Global Positioning System



#### **3.3.4.1. Reference System**

The heights of the measured points were referenced to an identified national survey benchmarks located close to the study area. These benchmarks were found at distances farther away from the start of the survey work. In order to achieve consistency and correct the GPS measurements, the heights of the benchmarks were transferred to the surveyed area. *Figure 3-7* shows the location of the benchmarks and the additional references established during the height transfer. The datum of the referenced benchmarks and the overall survey was WGS84\_UTM. However, the vertical datum of the contours obtained from SMD was EGM2008<sup>27</sup>. Therefore, to maintain a common reference for the DEM validation, the surveyed points were projected from WGS84\_UTM to EGM2008 same as the contour data.

---

<sup>27</sup> Earth Gravitational Model 2008

## 4. METHODOLOGY

### 4.1. Sentinel-1 Image Processing

The Sentinel-1 image processing method was sectioned into two, namely a) the image pre-processing and b) the inundation detection. The flowchart below shows the steps of Sentinel-1 image processing.

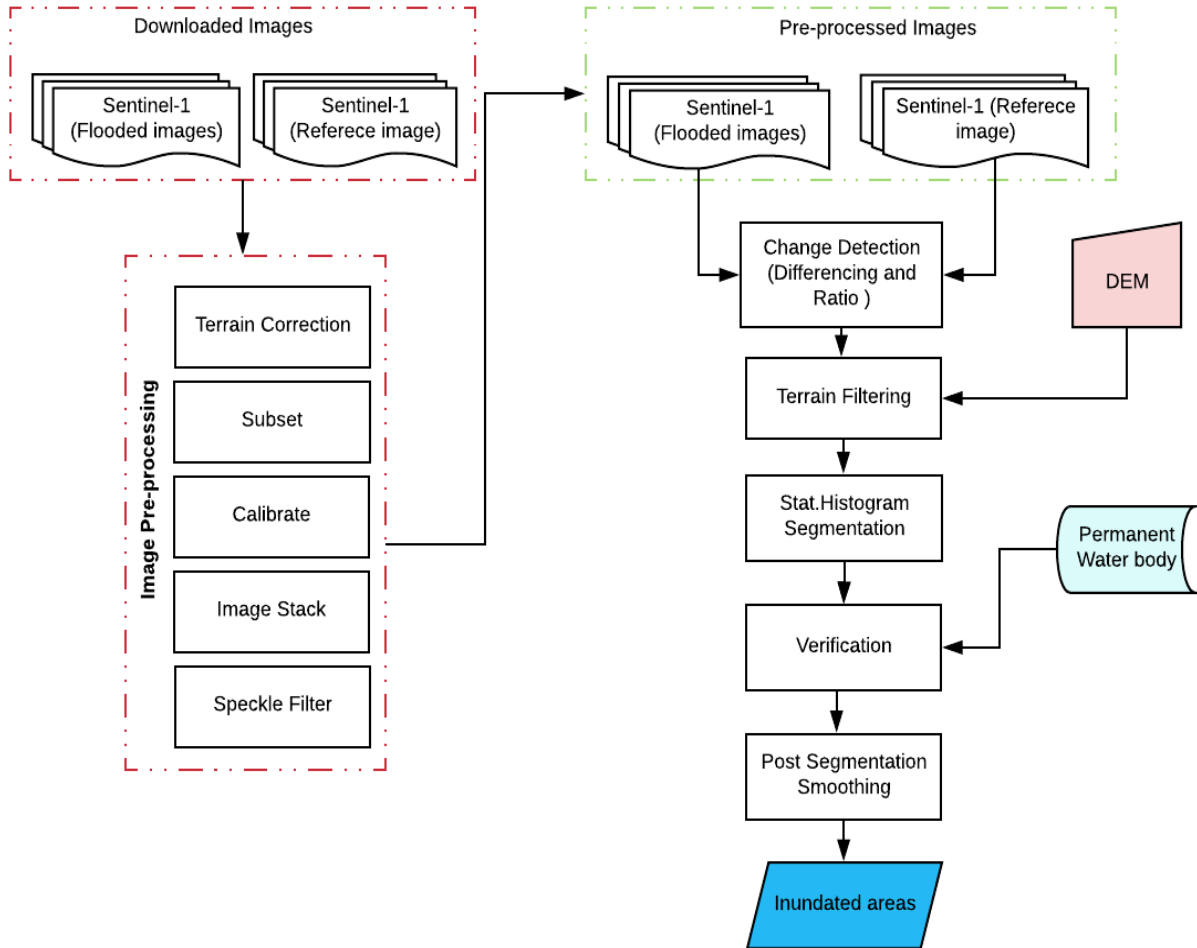


Figure 4-1: Flowchart of the Sentinel-1 flood extraction

#### 4.1.1. Sentinel-1 Image Pre-processing

The pre-processing of the Sentinel-1 images were performed using SNAP toolbox (S1TBX<sup>28</sup>). The toolbox consists of a collection of easy-to-use tools and data products for display, processing and analysis of SAR data. The pre-processing tools utilised in this study included i) Terrain correction ii) Subset iii) Calibration iv) image stacking and v) Speckle filtering.

##### 4.1.1.1. Terrain Correction

During SAR data capturing, the tilt of the sensor and the terrain variations distort the distances and object positions in the SAR images. Also, the original images were found to be inverted after download. For the above reasons, a terrain correction was performed to compensate for the distortions and improve the

<sup>28</sup> Sentinel-1 Toolbox

geometric representation of the image. The Range Doppler Terrain correction tool was applied for the terrain correction. This method used the orbit information in the metadata, the slant to ground range conversion parameters and a reference DEM (in this case SRTM DEM) to orthorectify and correct the geolocation information of the images (ESA, 2017).

#### **4.1.1.2. Image subset**

The downloaded scenes were larger than the area of interest for the study which is 15Km<sup>2</sup>. To limit the processing to the area of interest as well as reducing process time, the images were subset to preserve the area interested in the analysis. A batch processing tool in the SNAP toolbox was programmed to subset all downloaded images.

#### **4.1.1.3. Calibration**

According to ESA (2017), Level 1 SAR data processing does not include radiometric correction. Consequently, the pixel values of the Sentinel-1 images are provided in DN<sup>29</sup> values. SAR image calibration was used to convert the pixel values to the radar backscatter values of the reflecting land cover surfaces. Since the changes in backscatter were analysed for inundation extraction, it was necessary to apply image calibration to evaluate the changes in the actual backscatter of the surfaces.

#### **4.1.1.4. Image Stack**

Temporal assessment of backscatter changes was exploited to quantify the changes in backscatter coefficient for inundation detection. The image stack tool was used to collocate the images into one geographical position. The pixels of the same geographic location were coincided to enhance inter pixel analysis. In this study, the dry image captured on 26/04/2017 Sentinel-1 image (the reference image) was used as the master while flooded images (25/06/2017 and 07/07/2017) were used as slaves. The resampling type used was the nearest neighbour to preserve as much as possible the information from the original images.

#### **4.1.1.5. Speckle Filter**

Speckle is the granular noise that inherently exists in SAR images and degrades the image quality (Clement et al., 2017). The constructive and destructive interference of return waves scattered within each resolution cell cause speckles in the SAR image. This defect often makes the SAR images difficult to interpret. Speckle filtering algorithms were applied to reduce the speckle effects on the SAR images. However, application of the speckle filter may replace “true” observed information as well. The SNAP toolbox has multiple in-built speckle filtering algorithms such as the Lee, Lee Sigma, Refined Lee, Frost, Median, and Gamma Map. The purpose of this test was to select a filter which reduced the speckle noise while preserving the spatial resolution and edge information of the images.

To determine the appropriate filter for the study, the above filters were applied to the 25/06/2017 Sentinel-1 image. A 3X3 kernel was used in all filtering to preserve as much as possible the image information. After a visual comparison, the Gamma Map filter was found better preserve the edge information of the image. Moreover, Mansourpour et al. (2006) established that the Gamma Map was efficient to reduce speckle and preserved the edge information of the observed surfaces. The boundary detail of the river course at the narrow width sections as indicated by the red circle in *Figure 4-2*, appeared better in Gamma Map. In that regard and through subjective selection, the Gamma map was applied to the other images.

---

<sup>29</sup> Digital Numbers

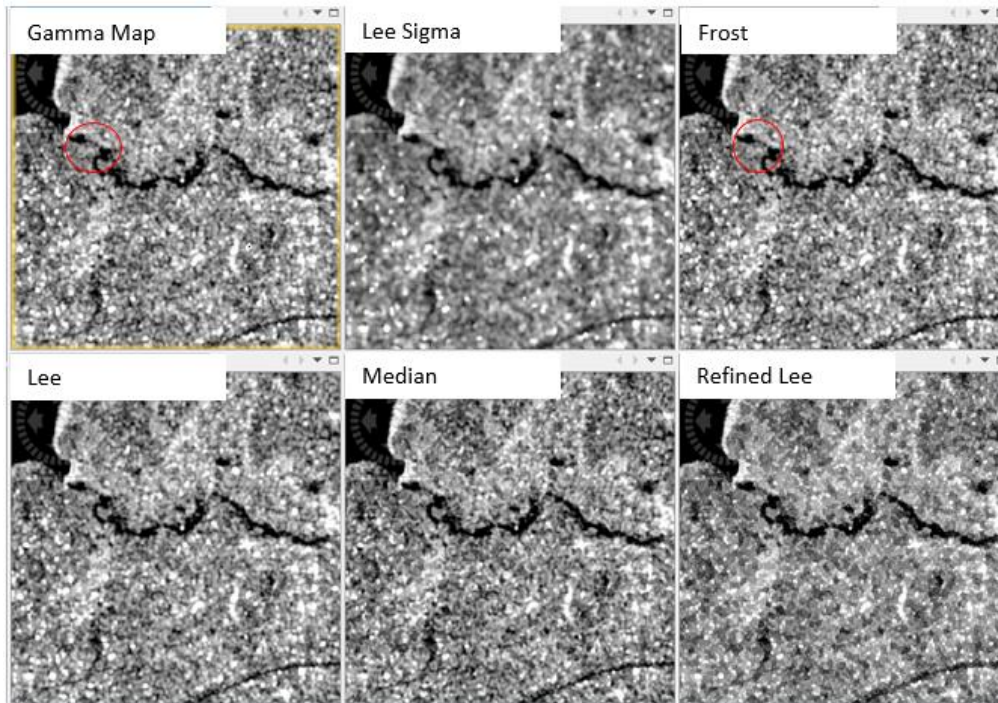


Figure 4-2: Visual comparison of results of speckle filtering techniques

#### 4.1.2. Sentinel-1 Inundation Mapping

The extent of river inundation was used as an indication to select the flooded images. This initial assumption was necessary since inundation extent in the built-up area cannot directly be observed in the SAR images. To effectively map inundation in the built-up area, the change detection method was applied to detect inundation from the Sentinel-1 SAR images. The BandMath tool in the S1TBX was utilised for this application. The two change detection methods as mentioned in the literature review were employed for the inundation extraction (i.e. the differencing method and the ratio method). These methods involved the use of two or more temporally different Sentinel-1 SAR images of the same area. The change detection method is a pixel by pixel based analysis of the reference image and flooded image. The first change detection method explored was the image differencing and subsequently the image ratio method.

##### 4.1.2.1. Change Detection Methods

The pixel-by-pixel based image differencing method was performed according to the procedure by Long et al. (2014). The absolute backscatter values of the pixels in the reference image (i.e. 26/04/2017) were subtracted from the pixels in the flooded images (i.e. 25/06/2017 and 07/07/2017). The method was performed on the VH and VV polarisations of the Sentinel-1 images. The expression below (Equation 4-1) was used to prepare the residual difference images.

$$\text{Difference Residual Image} = |\text{Pixel Flooded Image}| - |\text{Pixel Reference Image}| \quad \text{Equation 4-1}$$

The concept of this approach was that the difference residual image showed a pixel based representation of the no change and change areas. Additionally, the resultant histogram of the residual image showed no change as zero or close to zero while changed pixels resulted in negative and positive values.

In a like manner, the ratio method was applied to determine the pixel-based changes in the flooded image against the reference. The absolute pixel backscatter values of the VH and VV polarisations of the flooded image were divided by the absolute pixel backscatter values of the same polarisation of the reference image. The expression in Equation 4-2 was used in this approach.

$$\text{Ratio Residual Image} = |\text{Pixel Flooded Image}| / |\text{Pixel Reference Image}| \quad \text{Equation 4-2}$$

The no change pixels were quantified as one while the change pixels resulted in ratios lower than one or greater than one in the residual ratio image. The histograms of the residual images were later segmented to detect the backscatter changes as flooded areas.

#### 4.1.2.2. Terrain Filtering

To reduce the effect of inundation lookalike changes on the detected inundation, the DEM was used to limit the analysis to flood-prone areas. In previous studies (e.g. Martinis et al. (2015) and Twele et al. (2016)), the HAND DEM automatic technique was used, limit inundation detection to elevations highly susceptible to flood. In this study, the researcher applied a manual method with a similar concept as the HAND approach to reduce flood lookalike pixels within heights above the drainage susceptible to flood in the area for the urban flood detection. The approach was executed by drawing a cross-sectional profile from the left bank of the channel to meet the same height at the right bank as illustrated in *Figure 4-3*. Several cross-sectional profiles were drawn across the channel to establish the height for the inundation analysis. The DEM extent was modified using the contours. Once the profiles were defined, the extent was used to mask areas in the residual images highly susceptible to inundation. This approach was beneficial in previous studies of SAR inundation mapping to minimise the flood-lookalike misclassification at DEM locations that are unlikely to flood.

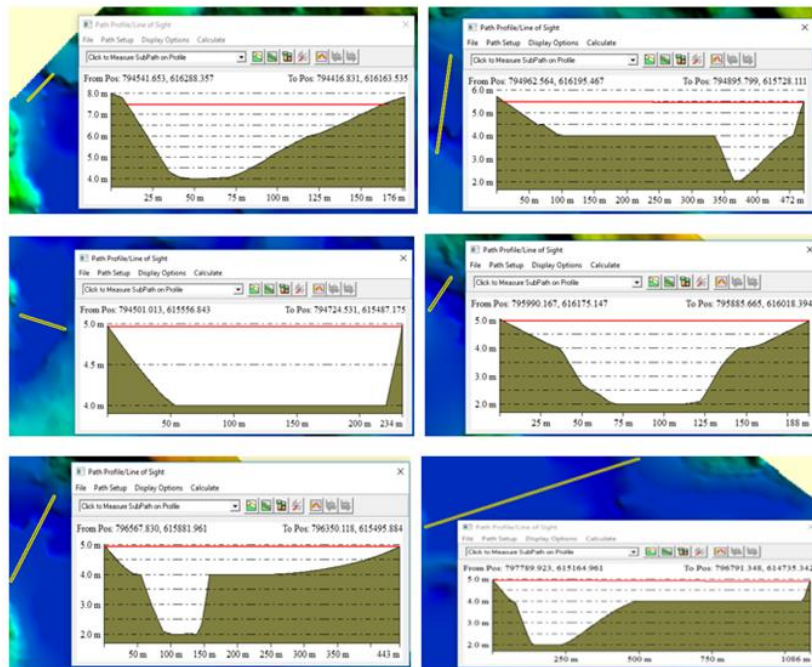


*Figure 4-3: Cross-sectional profiles of the river width*

#### 4.1.2.3. Residual Image Histogram Segmentation

Following the terrain filtering, the histograms of the residual images were segmented for the flood detection. The procedure involved masking out areas of no change or minimal changes of the residual difference and ratio images. The percentile threshold values were extracted from the histograms of the residual images and used to segment the backscatter changes through binarization. The percentile threshold values between the lower and upper threshold values were segmented as no change pixels. The segmented image showed pixels of no change as 0 and changed pixels as 1. The thresholds of the following percentile ranges were used for the residual image segmentation i) 25<sup>th</sup>-75<sup>th</sup>, ii) 20<sup>th</sup> -80<sup>th</sup>, iii) 15<sup>th</sup> -85<sup>th</sup>, iv) 10<sup>th</sup> -90<sup>th</sup> and v) 5<sup>th</sup> -95<sup>th</sup>.

#### 4.1.2.4. Verification

Due to the specular reflection of calm and open water surfaces, the backscatter intensity hardly changes over time (White et al., 2015). Therefore, to ensure that misclassification did not influence the segmented changes, a simple verification test was conducted. The segmented results were verified with the permanent water body (in this case the Weija reservoir) to the misclassification of the percentile range thresholds. Based on the verification results and area of inundation detected in each range, the optimum percentile range was selected for the inundation detection of the other images.

#### 4.1.2.5. Post segmentation smoothing

After the segmentation, there was no continuity of the detected changes. For this reason, a post segmentation filtering was performed to remove the isolated pixels and improve the representation of the image. A majority filter tool in ArcGIS was utilised for this purpose. A 3x3 kernel filter was defined, for every eight neighbouring pixels that determined contiguity based on an edge connection.

#### 4.1.3. PlanetScope Flood Detection

PlanetScope was the second source satellite image analysed in this study. As indicated earlier, the PlanetScope image is comprised of four (4) bands (i.e. Red, Green, Blue and NIR). Two images (25/06/2017 and 14/07/2017) out of the four downloaded were selected to be viable for the inundation detection, due to cloud cover limitations. However, the selected images were not entirely cloud free. Hence the effects of the cloud shadow were inevitable even though the clouds were masked out before the application of the NDWI. The NDWI is expressed in Equation 4-3 as

$$NDWI = \frac{\text{Green}-\text{NIR}}{\text{Green}+\text{NIR}} \quad \text{Equation 4-3}$$

The NDWI image was analysed and inundation extent extracted. The detected inundated pixels were resampled from 3m resolution to 10m, to match the pixel resolution of the Sentinel-1 and the grid size of the flood model to enable subsequent pixel based comparison. A similar terrain filtering as applied in the Sentinel-1 flood detection was used to limit inundation detection to the high flood-susceptible area. Also, a post-processing smoothing as explained in *sub-section 4.1.2.5* was performed to enhance pixel continuity of the detected inundation extent.

## 4.2. DEM Validation and Enhancement

DEM is an essential model input in flood modelling. Therefore, inaccurate representation of real-world elevation by a DEM can lead to inaccurate simulation of flood extent. Moreover, the elevation model largely affects the flood depth whereas elevation gradients affect velocity as well as the direction of flow on the floodplain (Deltares, 2017). A 2m interval digital contour acquired from the SMD was utilised in the creation of the DEM of the study area. In order to ensure all heights were included in the elevation model formation, the TIN<sup>30</sup> model of the surface was prepared in ArcGIS. Rennó De Azeredo Freitas et al. (2016) argued that TIN is an efficient method of terrain surface representation as the density of the height points or lines included in the DEM preparation affects the accuracy of the land surface elevation created.

The created TIN was then rasterised into 5m, 10m and 20m grid DEM raster which were ideal for the numerical computation of SOBEK model. Similarly, a DEM was prepared using GPS points of the surveyed areas. The contour DEM was compared with the GPS DEM, and the difference evaluated through visual

<sup>30</sup> Triangular Irregular Network

inspection. The areas with high relative disparities were improved using the GPS points measured in the field. According to Smith et al. (2006), GPS survey measurement is perceived to be more accurate. The heights of the rasterised contour DEM were extracted with the GPS points for all the grid sizes and the differences statistically analysed. The overall procedure for the DEM assessment is shown in *Figure 4-4*.

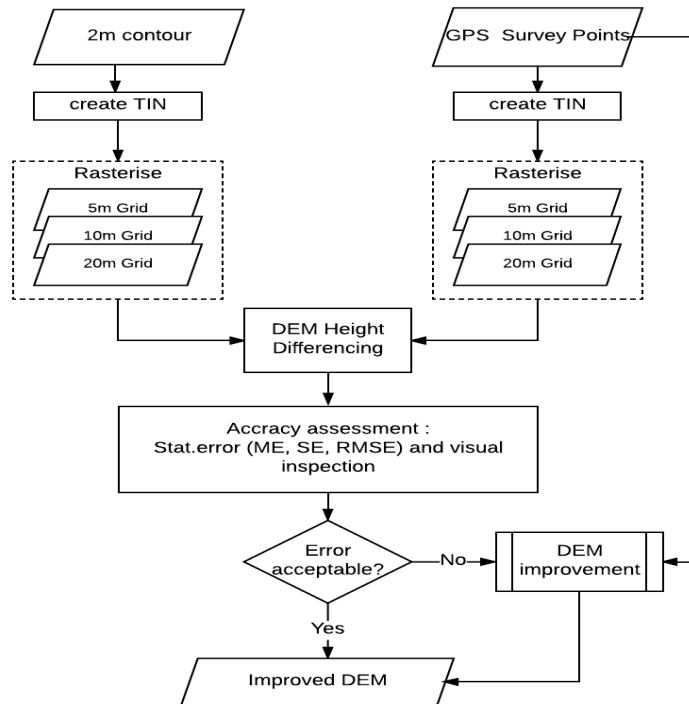


Figure 4-4: Flowchart of DEM validation and error assessment

#### 4.2.1. Accuracy Assessment

The accuracy of the contour DEM was assessed through statistical error evaluation and visual inspection of the difference map. Satge et al. (2016) and Elkhrachy (2017) are among many authors who have proven that statistical error measures such as Mean Error (ME), Standard Deviation (SD) and Root Mean Square Error (RMSE) are appropriate methods to determine the accuracy of a DEM. These measures were also employed in this study to estimate the error of the contour DEM from the GPS points DEM (reference data). The difference analysis was limited to the extent of the GPS points to minimise uncertainty in the error assessment. The DEM interpolation areas outside the survey boundaries were ignored. Table 4-1 presents the mathematical expression of the statistical measures used for the DEM error assessment.

Table 4-1: Statistical measures for DEM error assessment

Statistical Error Measure	Equations
<b>Mean Error (ME)</b> This error is estimated calculating the mean of the individual pixel bias. The method determines the extent of systematic error in the DEM creation.	$ME = \frac{1}{n} \sum_{i=1}^n (H_G - H_C)$
<b>Standard Deviation (SD)</b> This estimates the variation of the elevation differences in the mean elevation. This measure helps to identify pixels of more significant elevation differences.	$SD = \sqrt{\frac{\sum((H_G - H_C) - ME)^2}{n - 1}}$
<b>Root Mean Square Error (RMSE)</b> In this measure, the error is exaggerated by squaring differences in elevation between the contour DEM and GPS DEM.	$RMSE = \sqrt{\frac{\sum(H_G - H_C)^2}{n}}$

Where  $H_G$  is the GPS pixel height (reference),  $H_C$  is contour pixel height, and  $n$  is the total number of pixels evaluated

### 4.3. Hydrodynamic Flood Modelling

As part of the objectives of this research, a hydrodynamic model was set up to simulate the flood extent of the study area using 1D2D SOBEK hydrodynamic model. The major input parameters of the model included the DEM, River geometry, boundary conditions and surface roughness. The flowchart in *Figure 4-5* presents the stepwise procedures performed to achieve the set objective.

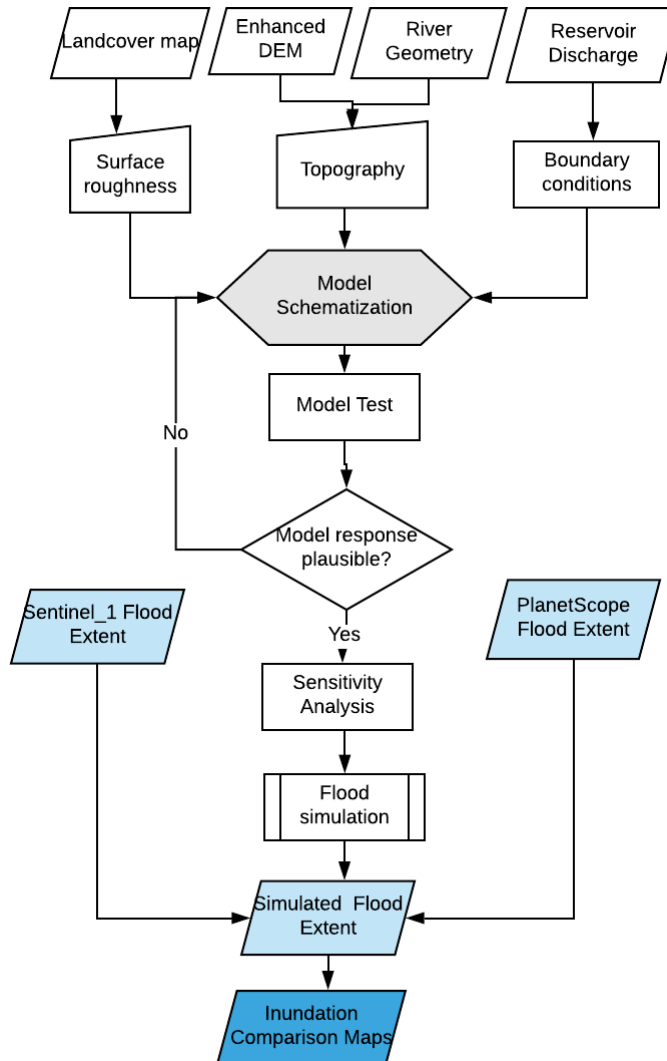


Figure 4-5: Flowchart of the hydrodynamic flood modelling and inundation comparison

#### 4.3.1. SOBEK Model Setup and Schematization

The 1D2D SOBEK model was set-up for the flood simulation of the study area. The SOBEK 1D2D hydrodynamic suite is a powerful modelling tool designed to simulate and analyse both simple and complex flow systems. The program is user-friendly and easy to set-up. The model input data structure are designed to schematically check for data input errors (Deltares, 2017). The model is set-up using the case manager, which is made up of a schematic flow of task blocks. Each block represents a task to be performed in order to successfully set-up and run the model. The NETTER is the GIS interface of the SOBEK model. The NETTER provided data input, editing and results viewing and analysis tools that were used to check for schematization errors and also analyse input and simulated data. Since the 1D2D model was used to simulate the flood extent, both the 1D and 2D were schematized.

The 1D flow model is comprised of a network of reaches connected to each other and represented as a staggered grid as illustrated in *Figure 4-6*. The water levels are calculated at the calculation points, boundary



and connection nodes. The velocity is estimated halfway between the calculation points and discharges are calculated at the reach segments.

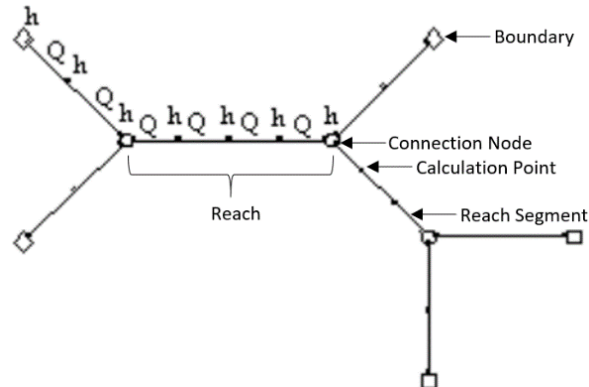


Figure 4-6: Staggered grid of SOBEK flow model (source: (Deltares, 2017))

The calculation points were assigned at each coordinate vertex of the channel. Due to the meandering nature of the Densu river, the distance between two neighbouring calculation points was not large for accuracy and proper representation of the physical processes within the channel. The main reach was diverted at a connection node while the linking reaches were connected to the main reach by linkage nodes. The flow boundary nodes defined the inflows and outflows of the model domain. Subsequently, the geometry of the channel was defined by cross-section and bridge nodes with information obtained from field measurements.

The 2D grid data of the floodplain topography was later imported into the NETTER as an ASCII file format. It was coupled with the already schematized 1D flow model of the channel by using flow-connection nodes. As a result, each calculation point or connection node was connected to the underlying grid cell as illustrated in Figure 4-7. The exchange between the 1D and 2D models was implemented by determining the connection points between 1D and 2D based on the map coordinates for the center of the 2D grid cell and the 1D connection node or calculation point node. The center of the 1D node is internally moved to match with the center of the 2D grid cell. The underlying 2D grid cell is counted as part of 1D Node such that, when the 1D flow level is the same or above the underlying 2D grid elevation the 1D flow is omitted in the flow computation. On the other hand, the model assumes a full 1D model computation when the 1D flow level is below the 2D grid level. The 1D and 2D schematization of the model domain is shown in Figure 4-8.

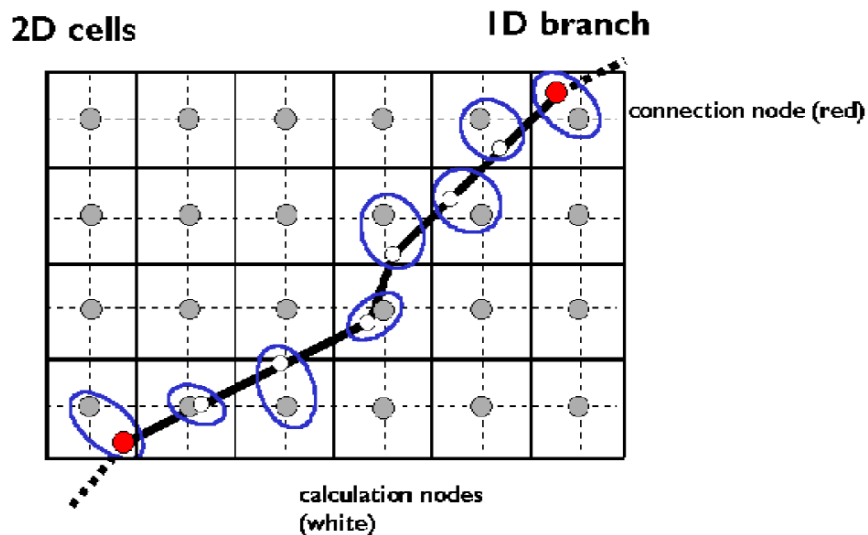


Figure 4-7: 1D2D model schematization (Source: (Deltares, 2017))

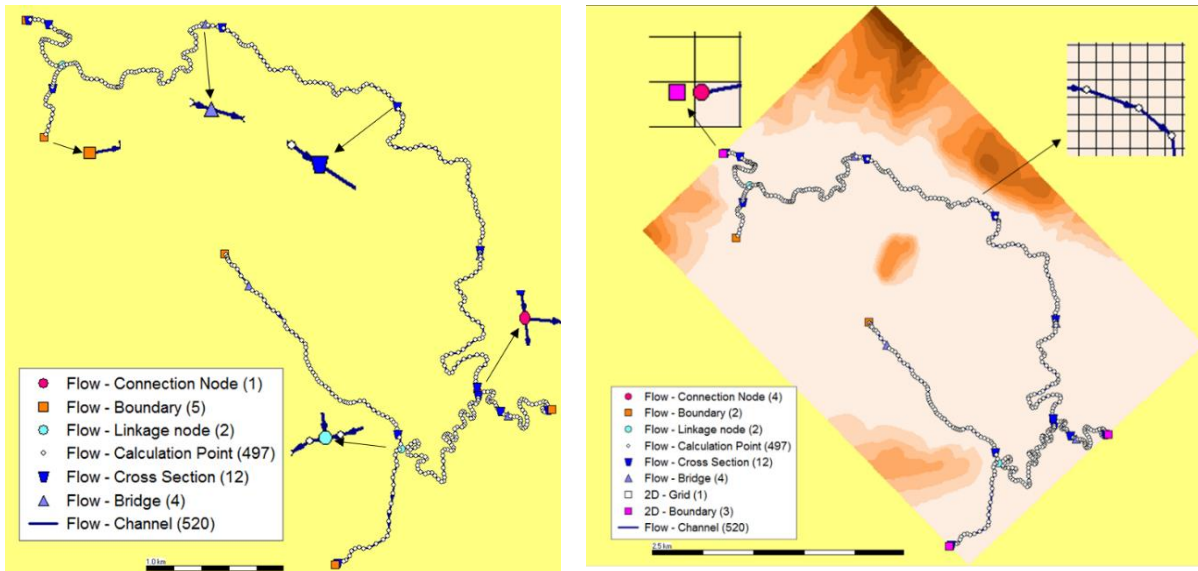


Figure 4-8: 1D and 2D schematization of the model domain

#### 4.3.1.1. Governing Equations

The water flow is computed by solving the complete De Saint Venant equations. The numerical computations of the SOBEK model are extremely robust and implement both mass and momentum conservations (Deltares, 2017). The 1D and 2D flow of mass and momentum conservations are calculated for each time step using the continuity and momentum equations expressed in Equations 4-4 to 4-7.

##### Continuity equation 1D

$$\frac{\partial A_f}{\partial t} + \frac{\partial Q}{\partial x} = q_{int} \quad \text{Equation 4-4}$$

##### Momentum equation 1D flow

$$\frac{\partial Q}{\partial t} + \frac{\partial}{\partial x} \left( \frac{Q^2}{A_f} \right) + g \cdot A_f \cdot \frac{\partial h}{\partial x} + \frac{gQ|Q|}{C^2 R A_f} - W_f \frac{\tau_{wi}}{\rho_w} = 0 \quad \text{Equation 4-5}$$

Where  $Q$  is the Discharge [ $m^3/s$ ],  $t$  is the Time [ $s$ ],  $x$  is the Distance [ $m$ ],  $A_f$  -Wetted area [ $m^2$ ],  $g$  is the Gravity acceleration [ $m/s^2$ ] ( $=9.81$ ),  $h$  is the Water level [ $m$ ] (with respect to the reference level),  $C$  is the Chézy coefficient [ $m^{1/2}/s$ ],  $R$  is the Hydraulic radius [ $m$ ],  $W_f$  is the Flow width [ $m$ ],  $\tau_{wi}$  is the Wind shear stress [ $N/m^2$ ],  $\rho_w$  is the Water density [ $kg/m^3$ ]

The terms in the equation describe in chronological order i) the inertia ii) the convection iii) the water level gradient iv) the bed friction v) the influence of the wind force and vi) the influence of extra resistance. The full description of these terms can be found in (Deltares, 2017)

### Continuity equation 2D

$$\frac{\partial \zeta}{\partial t} + \frac{\partial(uh)}{\partial x} + \frac{\partial(vh)}{\partial y} = 0$$

Equation 4-6

### Momentum equation 2D flow

$$\begin{aligned} \frac{\partial u}{\partial t} + u \frac{\partial u}{\partial x} + v \frac{\partial u}{\partial y} + g \frac{\partial \zeta}{\partial x} + g \frac{u|V|}{C^2 h} + au|u| &= 0 \\ \frac{\partial v}{\partial t} + u \frac{\partial v}{\partial x} + v \frac{\partial v}{\partial y} + g \frac{\partial \zeta}{\partial y} + g \frac{v|V|}{C^2 h} + av|v| &= 0 \end{aligned}$$

Equation 4-7

Where  $u$  is the velocity in x-direction [m/s],  $v$  is the velocity in y-direction [m/s],  $V$  is the velocity ( $\sqrt{u^2 + v^2}$ ),  $\zeta$  is the water level above plane of reference [m],  $C$  - Chézy coefficient [ $m^{1/2}/s$ ],  $d$  is the depth below the plane [m],  $h$  is the total water depth [m],  $a$  is the wall friction coefficient [ $1/m$ ]

The terms in the above equations are made up of acceleration, the horizontal pressure gradient, convective terms, bottom friction and last, the wall friction.

#### 4.3.1.2. Model Testing

A 1D steady state flow represents a simplification of flow mechanisms in open channels since the flow at each discrete location of a 1D model and does not change over time. Therefore, any possible error in the model set up can relatively be easy identified by erratic behaviour in the simulated flow patterns. The 1D steady state condition was run with a constant inflow discharge of  $5m^3/s$ ,  $50m^3/s$  and  $160m^3/s$  at the upstream boundary condition of a completely dry system for 715 simulation steps (30 days). Overall, the 1D steady flow was used to check the various aspect of the model such as how the cross-section geometry, the manning coefficient, the channel slope and other model features affected the model simulation results. Several runs were performed before achieving a plausible model response of mass and momentum balance. Each simulated results were analysed through visual interpretation and graphical analysis of the model results.

After the ID steady test, 1D unsteady state and 2D steady and unsteady state model tests were subsequently performed. The 1D model was tested using an artificial triangular wave flow prepared by the researcher starting from  $5m^3/s$  and rising to  $60m^3/s$  discharge. The 1D unsteady test was to evaluate the model response to dynamic flow.

The 2D tests were done to analyse the model response to real-world flow dynamics on the floodplain. The 2D topographical representation of the model domain was incorporated into the 1D model. The 2D model was run to test the response of the flow dynamics across the floodplain. The model was run for eight simulation time steps (i.e. from 01:00:00 to 05:00:00 at 30mins time step).

It must be noted that a very low flow of  $0.01m^3/s$  was imposed at the boundaries of the linking reaches, consequently ignoring its effect on the model simulation.

#### 4.3.1.3. Sensitivity analysis

Setting-up a flood model to simulate part of the real world is prone to many uncertainties arising from the generalisation of catchment characteristics to the governing equations used. Understanding the influence of

the model inputs is important to reduce uncertainties in model setup. The parameters analysed were the surface roughness and boundary conditions (i.e. inflow and outflow).

A theoretically acceptable range of roughness coefficient between 0.03 and 0.1 of manning’s values were used to represent the resistance to flow in the model domain. The minimum and maximum discharges within the flood window were used as the lower and upper limits of the upstream discharge. Since the downstream water levels were not available, the researcher based the downstream on the bottom level of the channel. Table 4-2 presents information on the parameters and parameter ranges analysed in the sensitivity test.

The variations of the model parameters were considered one parameter at a time while maintaining constant values of the other parameters. An invariant manning’s roughness coefficient was used to represent the entire model friction to flow. Each simulation was run for ten simulation steps (from 01:00:00 to 10:00:00).

Table 4-2: Model parameter and ranges for sensitivity analysis

Parameter	Range	Comments
Surface roughness (Manning’s coefficient, n)	0.03 - 0.1	The range reflected the major land cover of the model domain. The range encompassed the theoretically accepted range of Manning's roughness values for rivers, vegetation and developed areas (settlement)
Upstream boundary condition (m <sup>3</sup> /s)	27 - 168	The range was selected with reference to the flood window identified in the study. The minimum and maximum values of the window were used as the range
Downstream boundary condition (mAD <sup>31</sup> )	0.2 - 1.5	The bottom level of the outlets of the model was 0.3. The 1.5m water level at the down was selected to represent a likely water level rise at the outlet. Whereas the 0.2m represent low water level, thus more storage capacity at the outlet.

#### 4.3.1.4. Surface Manning's Roughness

The land cover of the model domain varied in space. In order to parameterise the surface roughness, the land cover map was prepared using the aerial photo of the domain and subsequently rasterised into 10m same as the grid size of the elevation raster. Moreover, the elevation grid was clipped with the roughness raster to maintain the same number of rows and columns in ArcGIS. It was then imported into the SOBEK model as an ASCII file format. The land cover classes mapped in the domain and the Manning's roughness assigned are tabulated in *Table 4-3* and spatially presented in *Figure 4-9*. The Manning’s roughness values were adapted from literature-based the land cover characteristics of the model domain. The main land cover class of the domain was the urban settlement and followed by vegetation (mostly shrubs) along the river channel.

<sup>31</sup> Above Datum

Table 4-3: Manning's roughness coefficient adapted from Medeiros et al. (2012)

<i>Land cover classes</i>	<b>Manning's roughness coefficient (n)</b>
<i>Settlement</i>	0.052
<i>Shrubs</i>	0.045
<i>River</i>	0.03
<i>Road</i>	0.01
<i>Bare land</i>	0.018
<i>Open forest</i>	0.022
<i>Wetland</i>	0.045

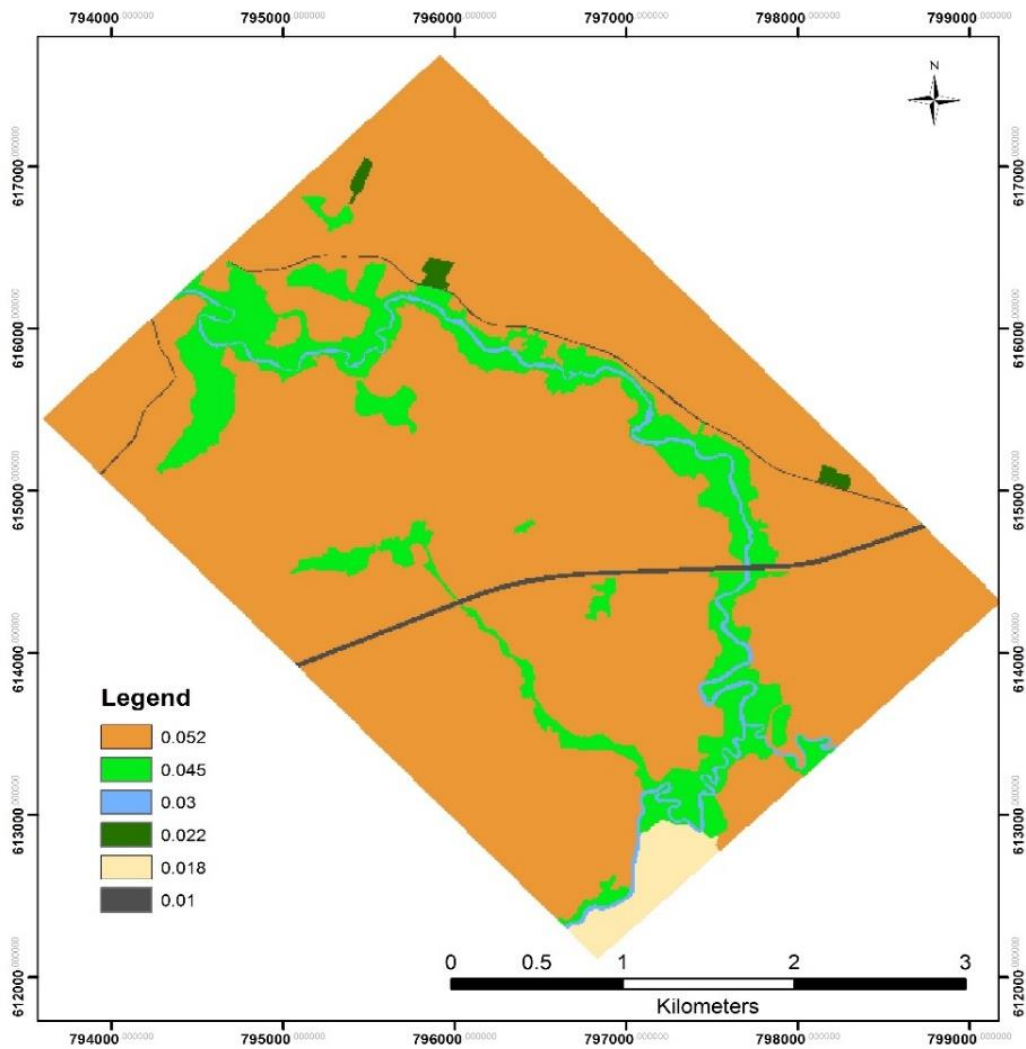


Figure 4-9: Manning's roughness coefficient of land cover classes

#### 4.4. Inundation Extent Comparison and Assessment

The extent of inundation detected from the two sources of satellite data (Sentinel-1 SAR and PlanetScope optical images) used in the study were compared with the model simulated flood extent. The Goodness of fit measure, was appropriate to analyse the match between the satellite detected inundation and the flood simulated inundation. The closeness of the simulated and the satellite flood extents would determine the appropriateness of satellite inundation extent for model calibration. The statistical measure presented in Table 4-4 was used to analyse the suitability of the Sentinel-1 SAR and PlanetScope optical flood extent to serve as a surrogate data for model calibration.

Table 4-4: Statistical measure for inundation extent comparison adapted from Grimaldi et al.(2016)

Measure	Equation	Description	Range
Goodness of fit	$\frac{F(MS)}{F(MS) + F(S) + F(M)} \times 100$	F(MS) are pixels shown as the flood in both model simulation and satellite. F (M) and F(S) are pixels shown as flood by the model simulation and the Sentinel-1 image respectively. The goodness of fit ranges between 0 for poor fit and 100 is for best fit.	0 - 100

## 5. RESULTS AND DISCUSSION

### 5.1. Sentinel-1 SAR Flood Extraction

The research aimed to analyse the suitability of satellite flood extent for hydrodynamic flood model calibration. Sentinel-1 SAR image was one source of satellite data used in this study. Inundation detection from SAR images (for that matter Sentinel-1) can be complicated especially in urban areas. However, the change detection methods (i.e. differencing and ratio) were explored to detect inundation extent of an urban setting in Accra. Two temporally different images (i.e. referenced – 26/04/2017 and flooded images – 25/06/2017 and 07/07/2017) were used for the analysis. *Figure 5-1* displays the RGB images of the reference and flooded image as well as the residual images of the differencing and ratio algorithms.

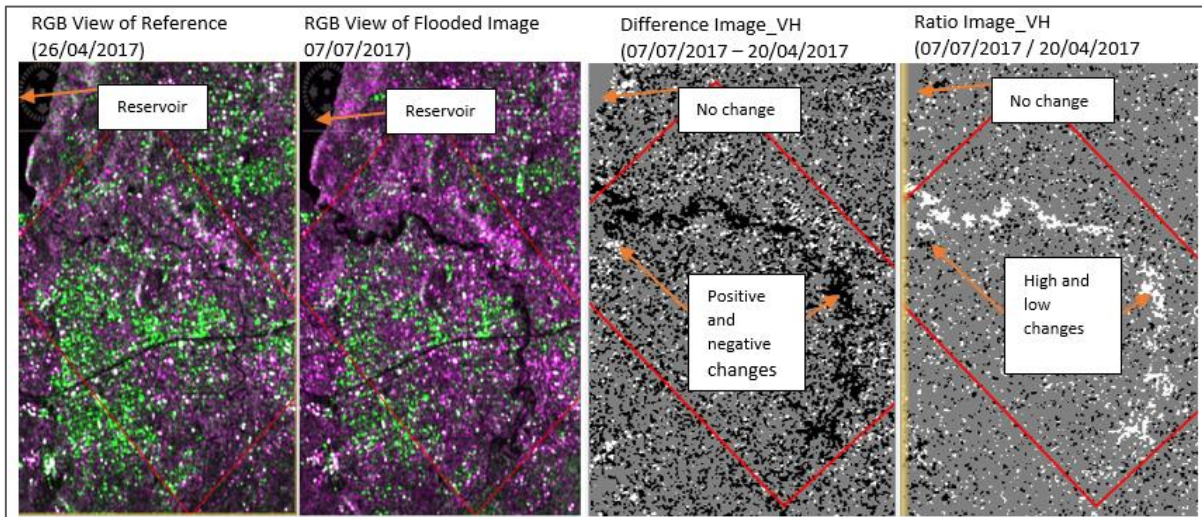


*Figure 5-1: RGB view of Sentinel-1 images and residual images after the application of the difference and ratio algorithms*

The concept of the differencing approach is that no change pixels result in zero value, while changed pixels characterised by relatively high positive and negative values in the residual image. As indicated in *Figure 5-1*, pixels of no change pixels appeared grey in the difference map while positive and negative changes appeared white and black respectively. In other words, surfaces of relatively high backscatter in the reference image (e.g. rough land) and would display a relative low backscatter in the flooded image when completely covered with water. Such pixels appeared white in the residual difference image. Also, flooded vegetation exhibited an increase in backscatter in the flooded image and hence presented as black in the residual image.

The ratio approach was applied to determine the changes in the flooded images as against the reference image. Like the residual difference image, the grey areas presented the no change while the changed pixels are depicted as white and black in the residual ratio image (*Figure 5-1*). The white pixels illustrated relative high ratio changes estimated from increased backscatter intensity of inundated pixels in the flooded image such as flooded vegetation. The black pixels also illustrated ratio values below one as a result of relatively low backscatter pixels in the flooded image such as flooded land surfaces.

Furthermore, the resultant histogram of the residual images was statistically segmented to detect the urban and vegetation inundation. The histogram of the residual images of the VH and VV (i.e. 07/07/2017 - 26/07/2017) are presented in *Figure 5-2*. From the histograms; it was apparent that majority of the pixels were unchanged as is peaked at the zero in the difference histograms and also the ratio histograms. The variation



of the resultant values from the ratio algorithm were small and difficult to interpret. Therefore, the logarithm scale was applied to enhance the changes in the residual ratio image. This output was similar to the result obtained by Xiong & Chen (2012), who also applied the logarithm scale to enhance the residual image and histogram interpretation.

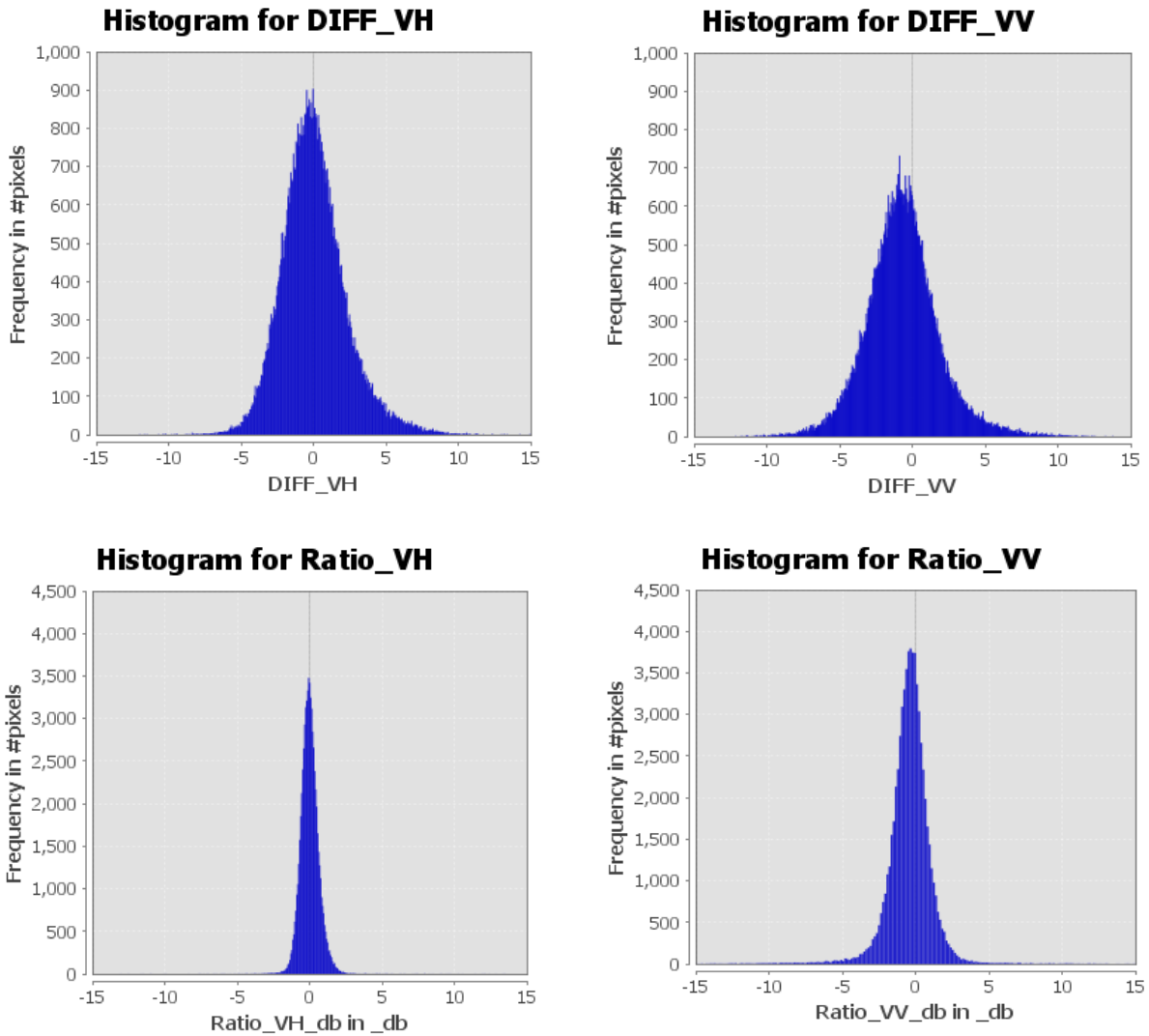


Figure 5-2: Histograms of the difference and ratio residual images

From Figure 5-2, the majority of the changes are distributed between -10 and 10 of the difference histogram, and between -5 and 5 of the ratio histograms. Additionally, the peak of no change pixels in the ratio histograms is greater than in the difference histogram. These results could suggest that the changes observed in the residual ratio images can distinctively be separated from the no-change pixels. The distribution of the histograms above could, therefore, clarify the dispersion of change pixels in the difference and ratio images in Figure 5-1 above, where there are more change pixels in the residual difference image than the residual ratio image.

The observed frequency of change detected pixels below -5 and above 5 is relatively greater in the VV polarisation than the VH polarisation in both the difference and ratio residual histograms. This indicated that the VV polarisation detected more changes than the VH polarisation. Moreover, the peak of no change pixels in both the VH and VV histograms above confirmed that the VV detected more changes than the VH as the number of pixels observed as no change is greater than the VV. Contrary to the difference histograms, the ratio histogram of the VV displayed a greater number of pixels with no change than the VH.



This could suggest that the relatively high detection of no change pixels in the residual images could help separate the inundated pixels distinctively from the non-inundated pixels. The peak characteristics of the residual ratio histograms could be an indication of the advantage of the VV polarisation to detect backscatter changes in the Sentinel-1 images. Moreover, the results confirmed earlier findings of Twele et al. (2016), who proved that the VV polarisation had a little advantage in inundation detection over the VH polarisation.

### 5.1.1. Verification of Backscatter Changes from Histogram Segmentations

Although previous studies have described the backscattering characteristics of water bodies, none have used it to verify the change detection method of inundated areas. The verification analysis was performed to demonstrate that the detected changes were not influenced by misclassification. *Figure 5-3* presents the graph and spatial representation of the verification analysis performed using the permanent water body (i.e. part of Weija reservoir). The percentile range threshold segmentation between 25th and 75th gave the highest rate of misclassification in each image. Moreover, the increase of change pixels in the water body indicated that the segmentation using the 25<sup>th</sup>-75<sup>th</sup> percentile range depicted relatively higher misclassification error than the other segmentation thresholds. It is possible, therefore, that the 25<sup>th</sup>-75<sup>th</sup> segmentation range could subsequently impose a relative high misclassification error in the inundation detection. Based on the observed misclassification error, this range was omitted from the further analysis.

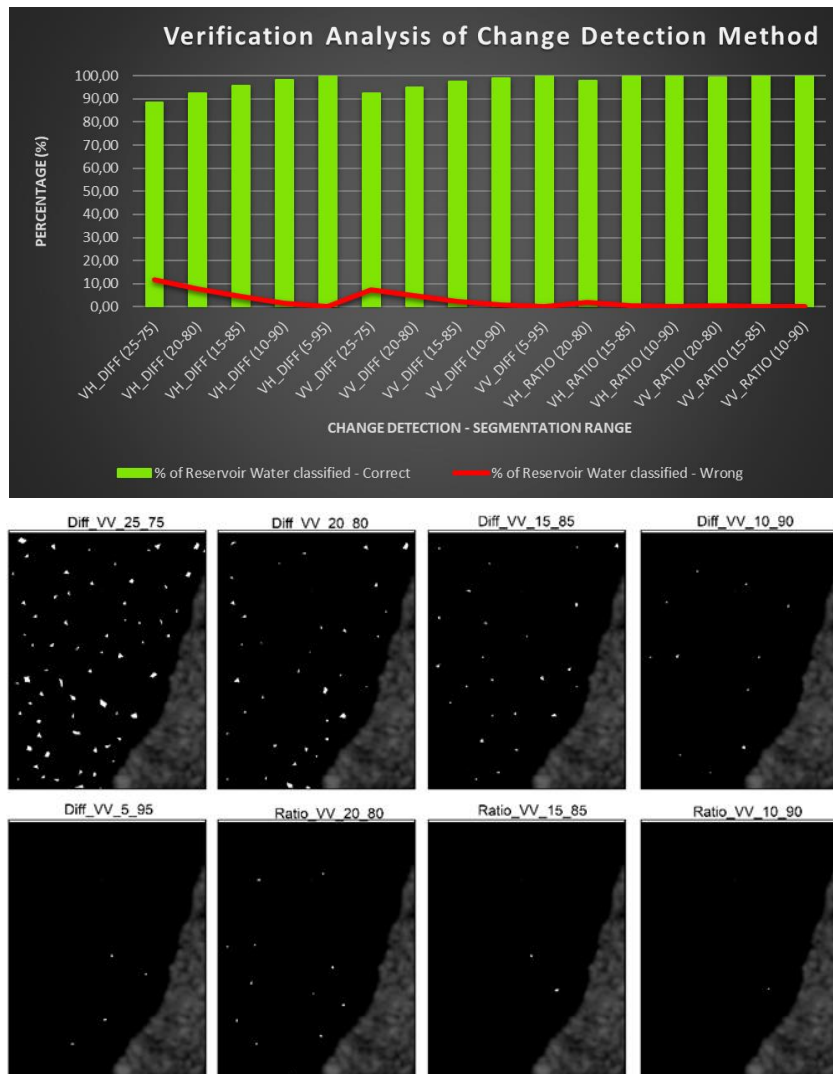
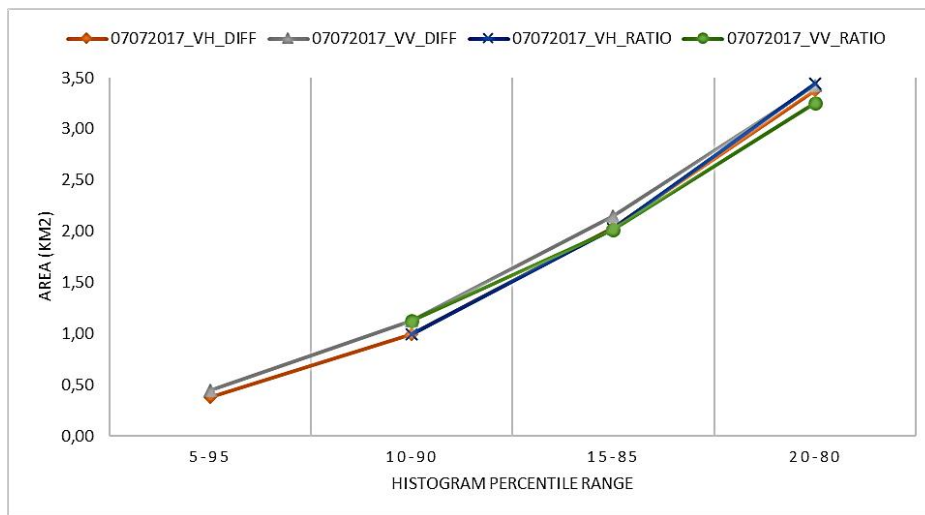


Figure 5-3: Verification analysis of segmented results for Weija reservoir

### 5.1.2. Segmentation for Inundation Extent

The second question in this research sought to analyse the extent to which Sentinel-1 SAR images can be used to observe inundation in an urban area. The thresholds of (20<sup>th</sup>-80<sup>th</sup>, 15<sup>th</sup>-85<sup>th</sup>, 10<sup>th</sup>-90<sup>th</sup>, and 5<sup>th</sup>-95<sup>th</sup>) percentile ranges were used to segment pixel changes as inundated from non-flooded areas. *Figure 5-4* shows a graphical overview of the segmented inundation area resulted from each percentile range thresholds. These results in *Figure 5-4* and *Figure 5-5* illustrated that more changes were detected with the 20<sup>th</sup>-80<sup>th</sup> percentile range segmentation. The results were in agreement with the findings of Mason et al., (2014), who established that the backscatter changes observe in urban areas were relatively lower than in rural areas. Consequently, the 20<sup>th</sup> -80<sup>th</sup> percentile range detected a larger area of inundation than the other percentile range thresholds. The results further suggested that changes in backscatter intensity caused by the flood in urban areas are minimal.

Moreover, the results further revealed that the other segmented ranges could not detect as many changes as the 20<sup>th</sup>-80<sup>th</sup> percentile thresholds (*Figure 5-5*). Consequently, more inundated pixels could not be detected. It is apparent that relative high changes as observed in the inundated vegetation could be segmented. These other percentile range thresholds could have used if the analysis was performed in a vegetated area. Therefore, to ensure that the minimal changes detected were extracted as inundation in the urban area, the 20<sup>th</sup>-80<sup>th</sup> percentile range thresholds were considered as the optimum range to detect inundation of Sentinel-1 SAR images for this study.



*Figure 5-4: Area of inundation after segmentation*

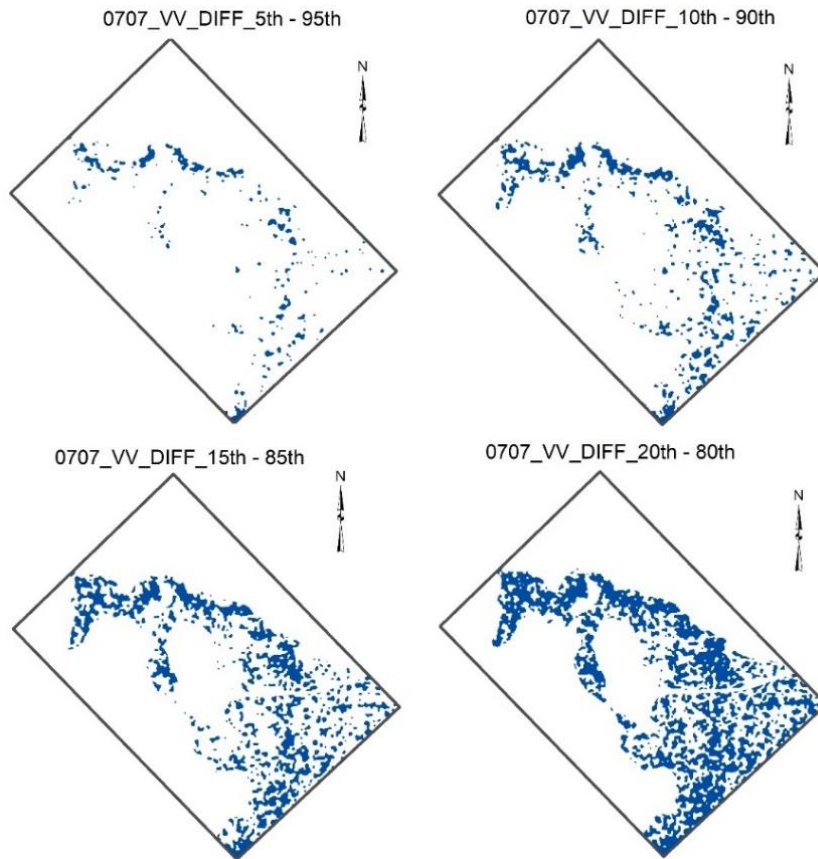


Figure 5-5: Inundation extent generated from the percentile threshold ranges

### 5.1.3. Results of Sentinel-1 SAR Flood Detection

The 20<sup>th</sup> -80<sup>th</sup> percentile range thresholds were used to detect inundation of the Sentinel-1 images of the study area for both the VH and VV polarisations. The maps of the detected inundation of the 07/07/2017 flooded image are presented in *Figure 5-6*. From the results, the VV polarisation displayed a relatively larger inundation extent than the VH polarisation, especially along the river course. These results agreed with the findings of Clement et al. (2017), who compared flood detected by the VH and VV polarisations and found out the VV detect water surfaces better than VH polarisation.

Furthermore, the pixels of the inundated areas were not continuous. It is possible that the structural arrangements of buildings and other vertical structures in the urban area obstructed the detection of flood water observed by SAR sensors. According to Mason et al. (2010), shadows and layover effects caused by these vertical structures reduce flood detection by about 20%. Moreover, the high backscatter intensity from the metallic roofing and other structures in the study area may impede the detection of the minor increase in backscatter intensities caused by the underlying flood water.

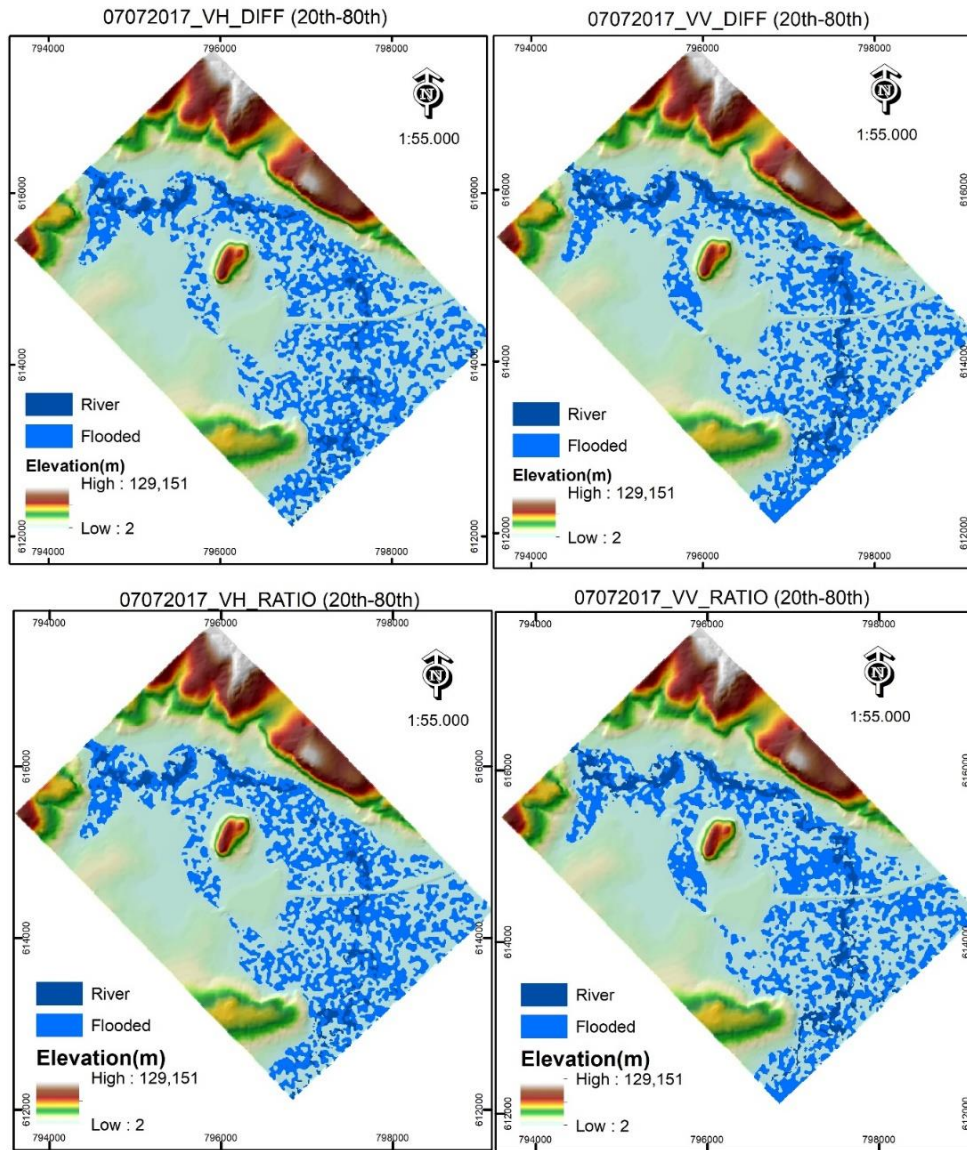


Figure 5-6: Inundation extent of the VH and VV polarisations of 07/07/2017

## 5.2. Flood Detection From PlanetScope Images

The NDWI map of PlanetScope image captured on the 25/06/2017 is presented in *Figure 5-7*. The result from the NDWI shows that cloud shadows and thin clouds which could not be masked (because its values were below the cloud mask threshold), resulted in positive NDWI values. Also, the ponds and wetlands covered with vegetation could not be detected since optical sensors cannot penetrate vegetation. Therefore the NDWI values of the vegetated covered ponds and wetland were negative and subsequently, influence the overall estimate of the observed inundation.



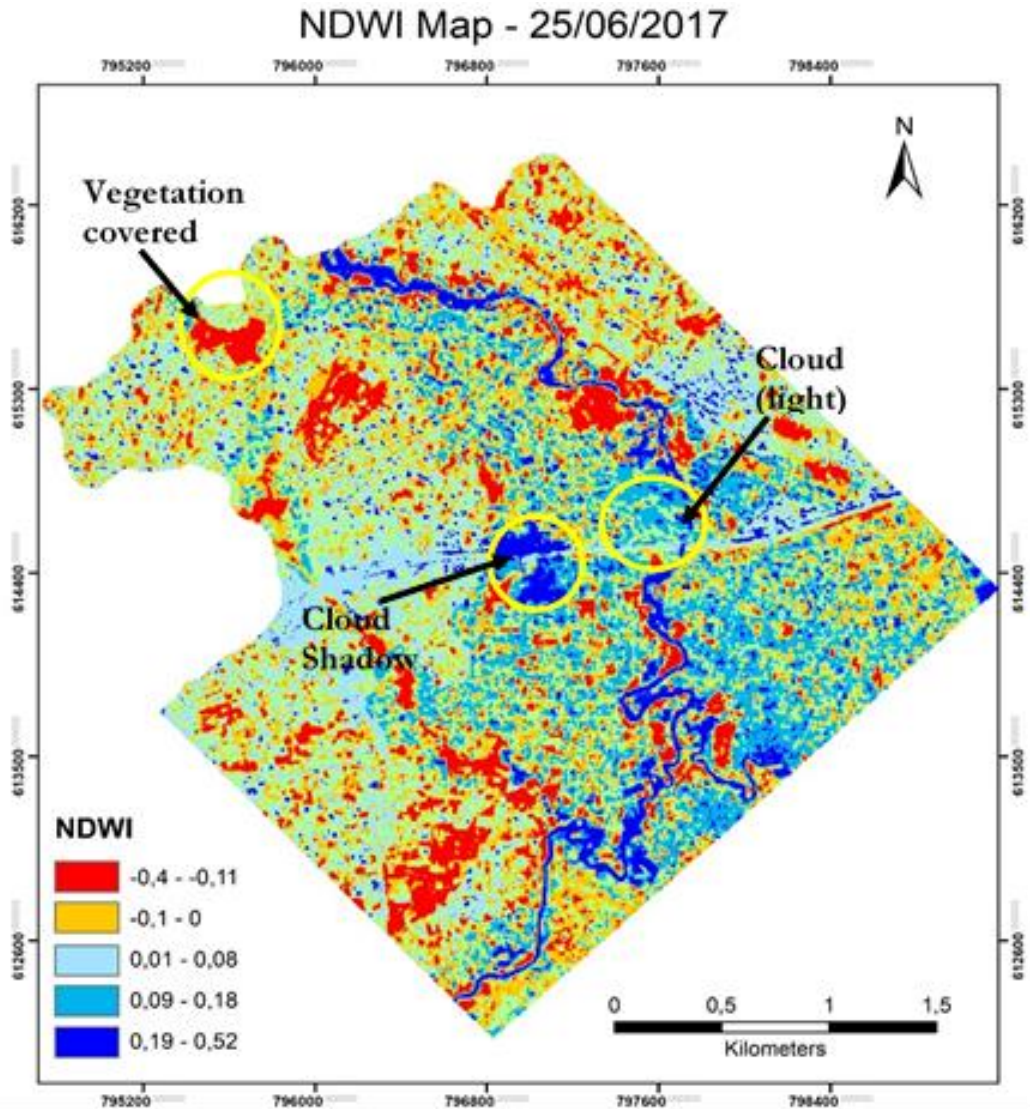


Figure 5-7: NDWI map of 25/06/2017

As indicated in the methodology, the normalisation of the green and NIR reflectance show water surfaces as positive and other land covers as negatives. However, the investigation conducted by Xu (2006), revealed that the application of the NDWI index in built-up areas does not comply with the above premise. Similar to the findings of Xu (2006), the results of the NDWI in this study depicted positive values in the urban area (see Figure 5-7). Thus, the extraction of inundated pixels in urban areas could be mixed with buildings. Nevertheless, the study by McFeeters (2013) established that NDWI values  $>0.1$  detected water bodies within an urban area. He proved that the NDWI values of buildings were between 0 and 0.1. Based on these findings, the inundated pixels of the PlanetScope images of the 25/06/2017 and 14/07/2017 were extracted as shown in Figure 5-8. Majority filter as explained in subsection 4.1.2.5 was applied to improve continuity of the detected pixels. Lastly, the terrain filtering was applied to filter out inundation-lookalike pixels at DEM locations of little likelihood to flood.

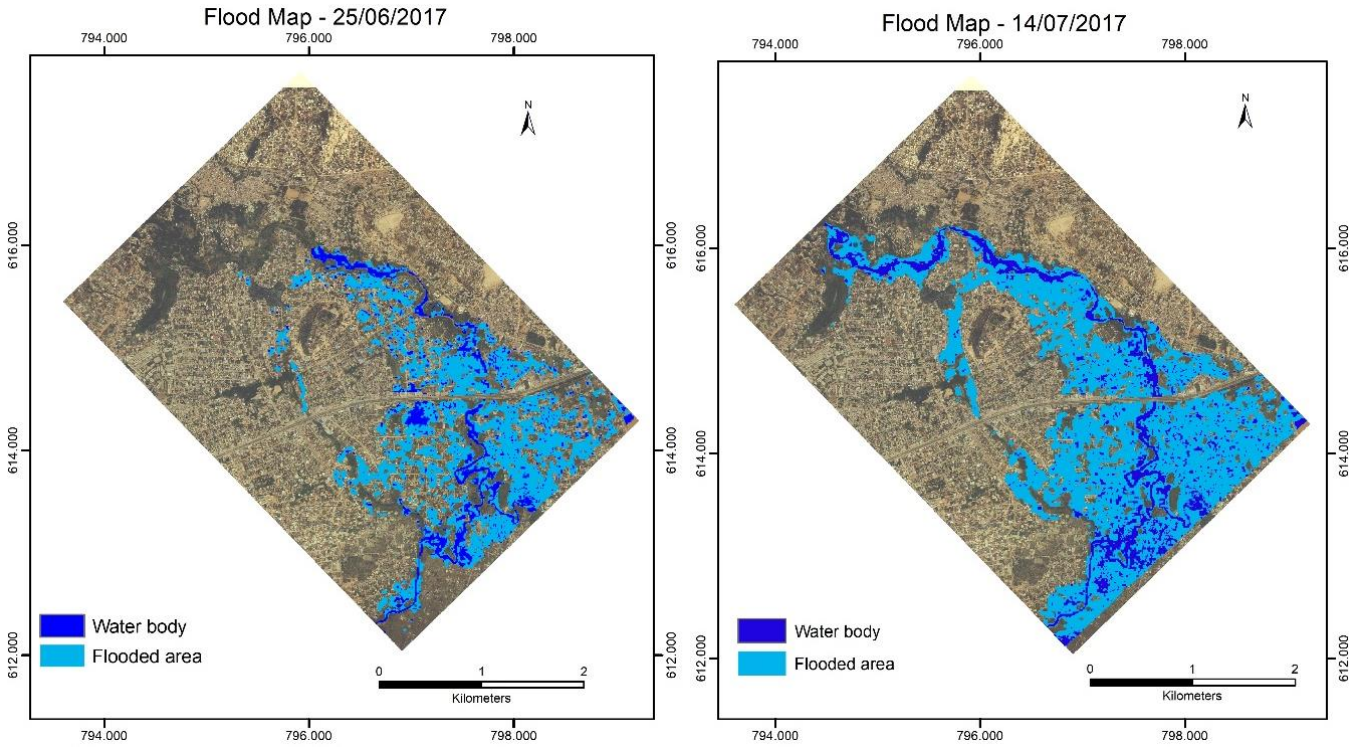


Figure 5-8: Flood maps of 25/06/2017 and 14/07/2017

### 5.3. DEM Accuracy Assessment

Topographical data in the form of elevation model is one of the major input of flood modelling. Hence, the correctness of the DEM as mentioned earlier, effect the flood model outputs (i.e. the extent and depth of inundation). To ascertain the accuracy of the contour, DEM was prepared for this study and evaluated against the GPS DEM also prepared using the GPS field measurement. A pixel-by-pixel based elevation difference map was created using the 5m resolution raster of the overlap areas of both DEMs (i.e. the contour DEM and the GPS DEM). *Figure 5-9* shows the spatial representation of the elevation differences at all surveyed areas.

The elevation difference analysis was limited to the survey extents of the GPS points, to minimise the effect of incorrect interpolation of no points areas in the GPS DEM creation. From the map, “Area 4” showed significant elevation differences. The contour elevation of 2m above datum was interpolated at the outlets. As a result, elevation of features like the roads and bridges were poorly represented in the contour DEM. These disparities were later corrected with the GPS measured points.

All the same, the overall accuracy of the contour prepared DEM for 5m, 10m and 20m resolution raster were statistically analysed. The GPS points were used to extract the elevation of the overlapped elevation pixels for the statistical assessment of the contour DEM. *Figure 5-10* provides the summary statistics and histogram distribution frequency of the elevation differences at 5m, 10m and 20m resolution. The results illustrate that the error increased as the cell sizes increase. That is to say, the resampling of the DEM raster caused changes to the original elevation values in the new raster. The summary statistics depicted no significant deviation from the GPS points. For instance, the RMSE values of all the DEM resolutions were about 20cm and according to Smith et al. (2006), is an allowable error for flood modelling.

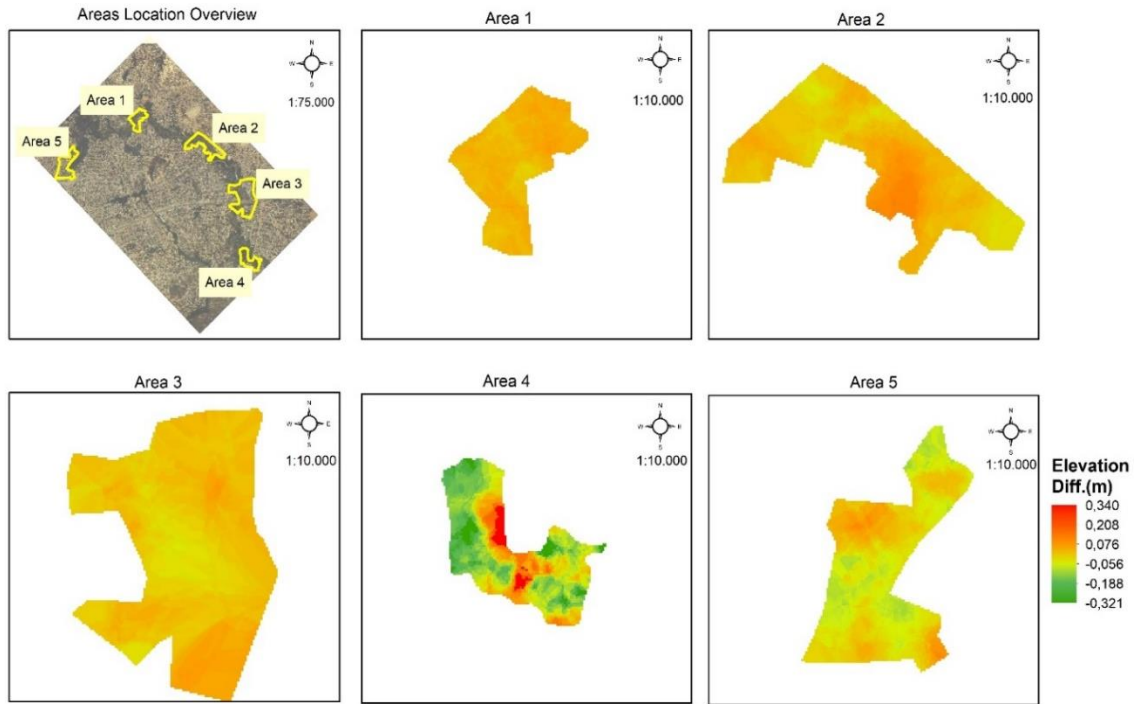


Figure 5-9: Pixel-based elevation difference maps of the of the GPS Survey locations

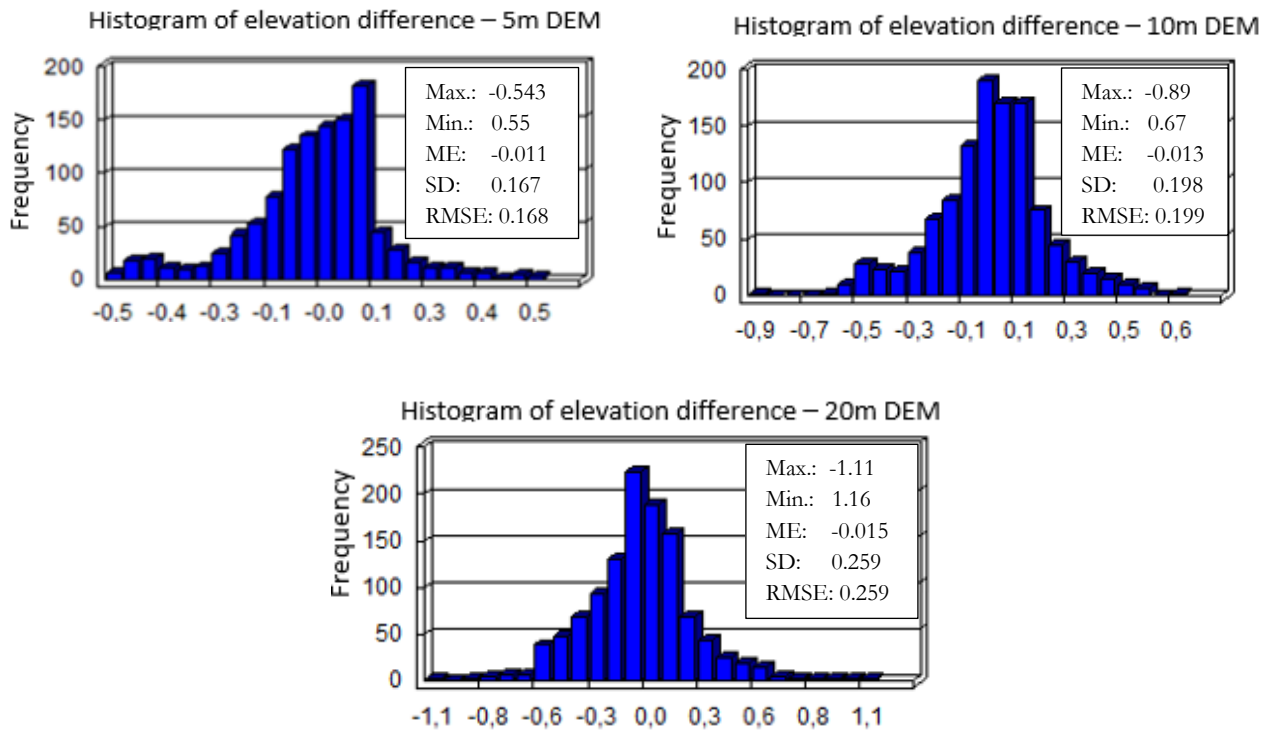
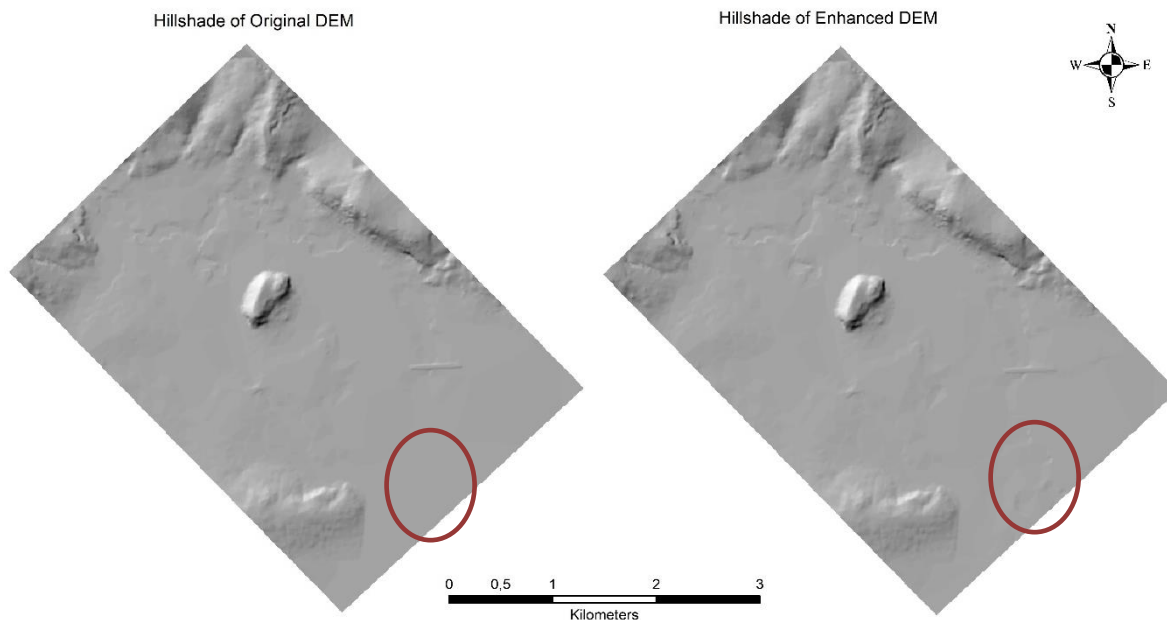


Figure 5-10: Frequency distribution and statistical summary of the elevation differences

### 5.3.1. DEM Enhancement

Despite the statistically accepted error quantified, the significant differences observed between the contour DEM and GPS DEM at area 4 could not be ignored. The observed deviation could effect the simulated flood extent of the area. For this reason, the GPS points were combined with the contour data to prepare an improved DEM. The enhanced DEM was rasterised to a 10m resolution to represent the topography of the model domain for the flood model. The hillshades maps of the original contour DEM and the enhanced DEM are shown in *Figure 5-11*. The brown circles mark the change in elevation, observed at “Area 4”. The elevations at the outlets are relatively low with respect to the datum. Hence the enhanced elevation at area 4 is hardly visible at this location.



*Figure 5-11: Hillshade maps of the original contour DEM and the enhanced DEM*

## 5.4. Model Set-up and Results

### 5.4.1. Model Testing

Testing the model was performed to identify erratic behaviour by errors in the model setup and to ensure that the mass and momentum balance of the schematized model is conserved. Moreover, a successfully tested model establish credibility in the real world model simulation. Several tests were run, including the 1D steady state and unsteady state and 2D unsteady flow tests. In each test, a couple of scenarios were tested, and model response analysed graphically and through visual inspection to assess if the model output was plausible.

For a channel to attain a steady state, for a time series covering multiple days, the model output discharge must be the same as the model input. The results of the 50m<sup>3</sup>/s constant flow were analysed below. The results of the 1D steady state test depicted an accumulation of water depth at the central section of the main reach as shown in *Figure 5-12*. This irregularity in flow occurred due to the sudden change in the channel bottom slope measured at cross-section 4. Since SOBEK linearly interpolate between the nearest cross-sections to obtain the channel bed slope, the raised level affected the slope of between the preceding and succeeding cross-sections as observed in *Figure 5-12*. This error could subsequently lead to artificial flooding in the 1D2D simulation. For that purpose, the channel bottom slope was manually corrected by averaging



the levels of the preceding and succeeding cross-sections of cross-section 4 as illustrated in *Figure 5-13*. The rectified level was accordingly corrected in the 1D schematization and the 1D steady flow test re-run. It must be noted that, due to the few number of cross-sections measured, the linear interpolation of the channel bed resulted in a smooth slope which may not be naturally the case.

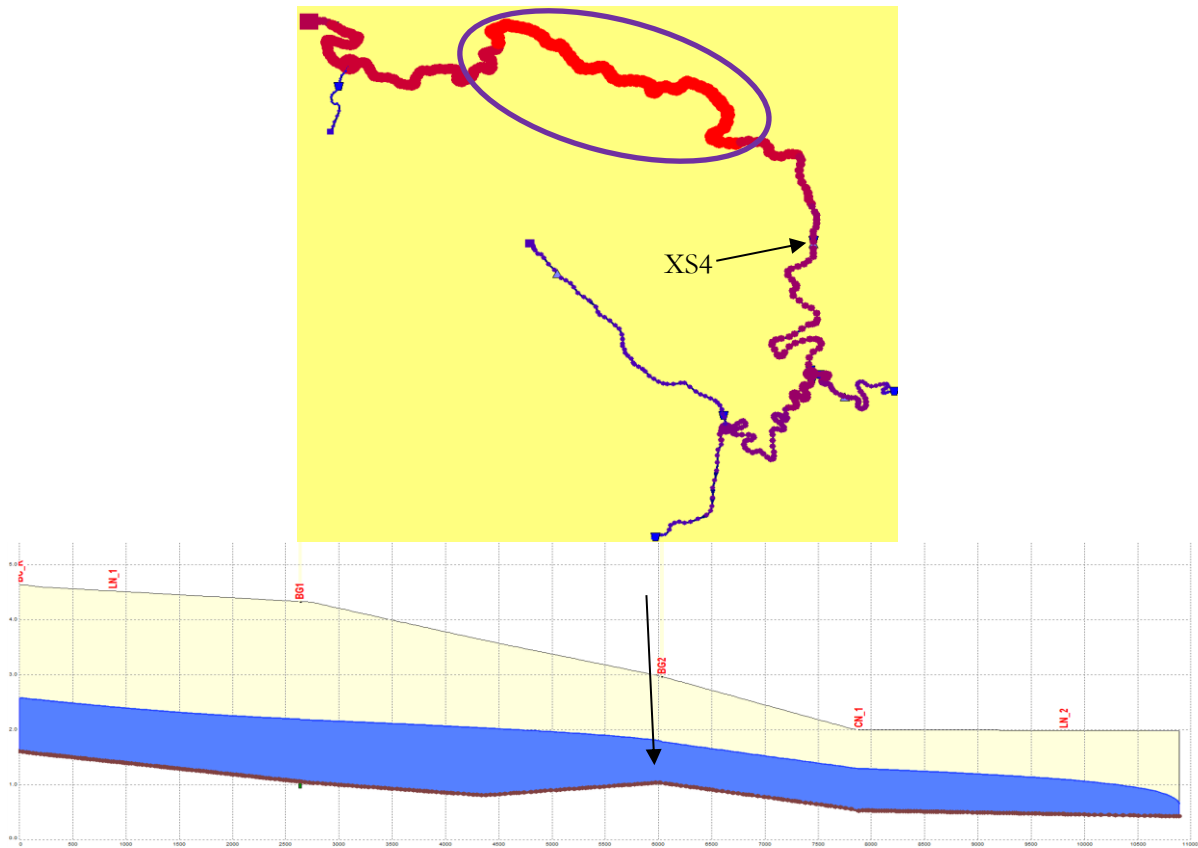


Figure 5-12: Netter view and longitudinal view of simulated 1D steady flow showing the uncorrected cross-section level

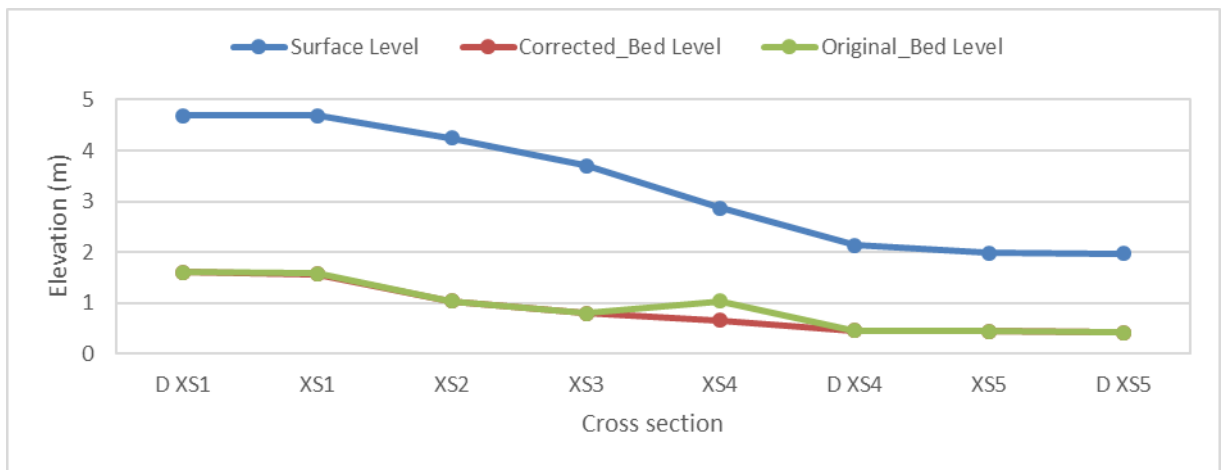


Figure 5-13: Corrected channel bed level

The simulated results after the channel bed slope correction illustrated a reasonable result of water depth transferred along the reach (*Figure 5-14*). The result was graphically analysed from the discharge graph illustrated in *Figure 5-15* that the sum of the outflow discharge from the diverting reach segments to Node 2\_3 and Node 3\_3 equal to the inflow discharge.

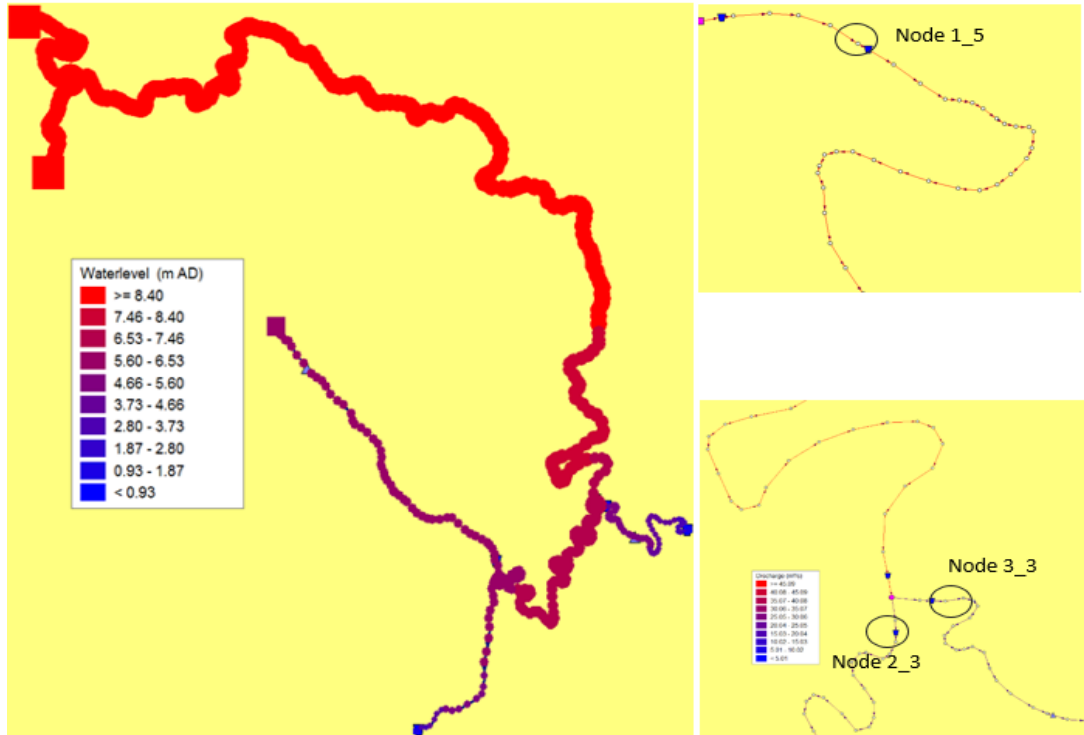


Figure 5-14: Simulated water level of 50m<sup>3</sup>/s steady flow and (left) location of nodes and segments analysed

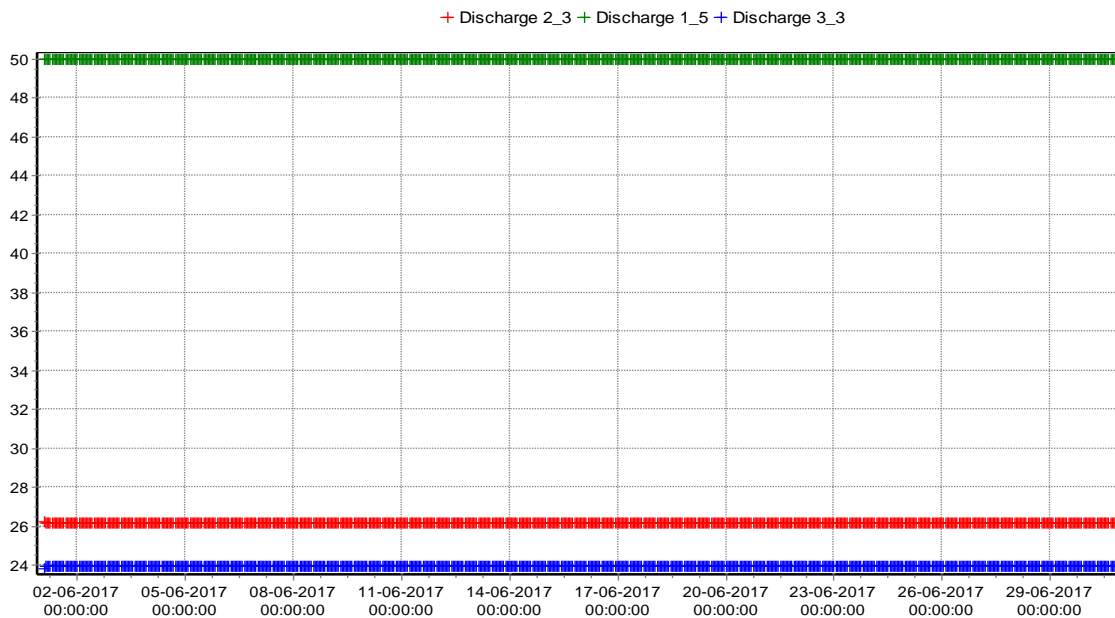


Figure 5-15: Discharge graph of 1D steady flow simulation analysis

The water level and the discharge result in the 1D flow computation in SOBEK. Hence, the water levels at the calculation nodes preceding and succeeding the connection node at the diverting junction were analysed. This analysis was essential to ensure that there were no backwater effects at the connection node which could propagate into an artificial flood in the real simulation. The water level of the preceding node to the connection node and the succeeding nodes of the diverting reaches were assessed. The differences in water level are presented in Figure 5-16. The water level difference of about 30mm was observed between the preceding calculation node and the connection node. Also, the water level difference between the succeeding

calculation nodes of the diverting channels was 10mm on the left branch and 20mm on the right branch. Consequently, the relatively low discharge in the right branch resulted in the relative lower water level from the connection node. These water level differences proved that there was a free flow of water at the connection node. It was interesting to note that, the water level in the main channel was distributed over the diverting channels which demonstrate mass and momentum conservation at the junction.

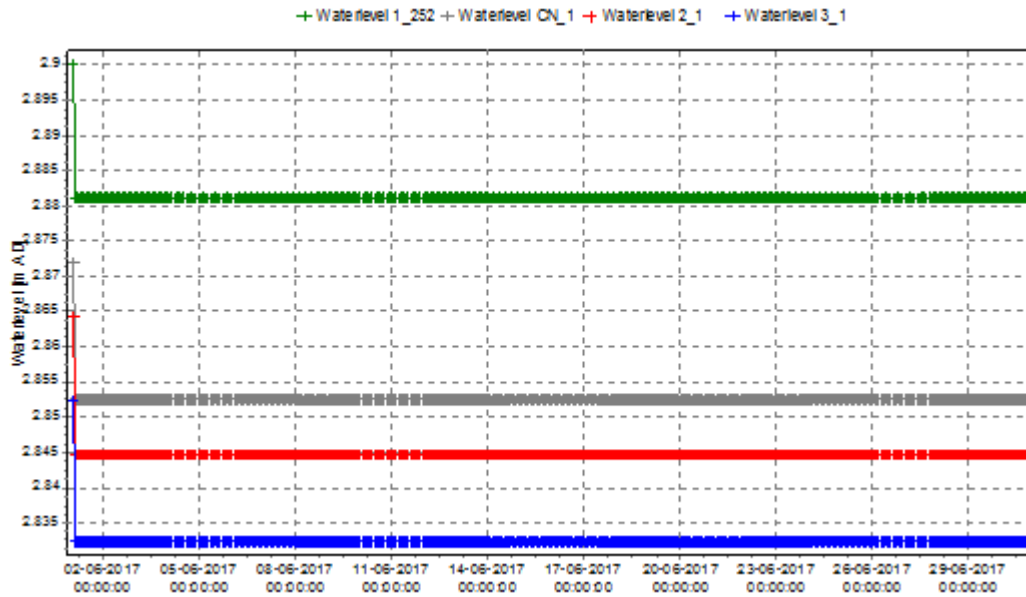


Figure 5-16: Graph of water level of nodes connected to the connection node

The 1D model was later tested for unsteady flow condition, and the response of the model to the inflow discharge is illustrated in Figure 5-17. The model responded well to the dynamic wave inflow provided to the model. Several scenarios of the 1D unsteady flow were tested with the model, and in all cases, the model showed a good response. Similar to the 1D steady flow the unsteady flow showed adherence of the model to mass and momentum conservation. The final test in the model set-up was the 2D steady and unsteady test, which responded well to the dynamic flow on the input discharge.

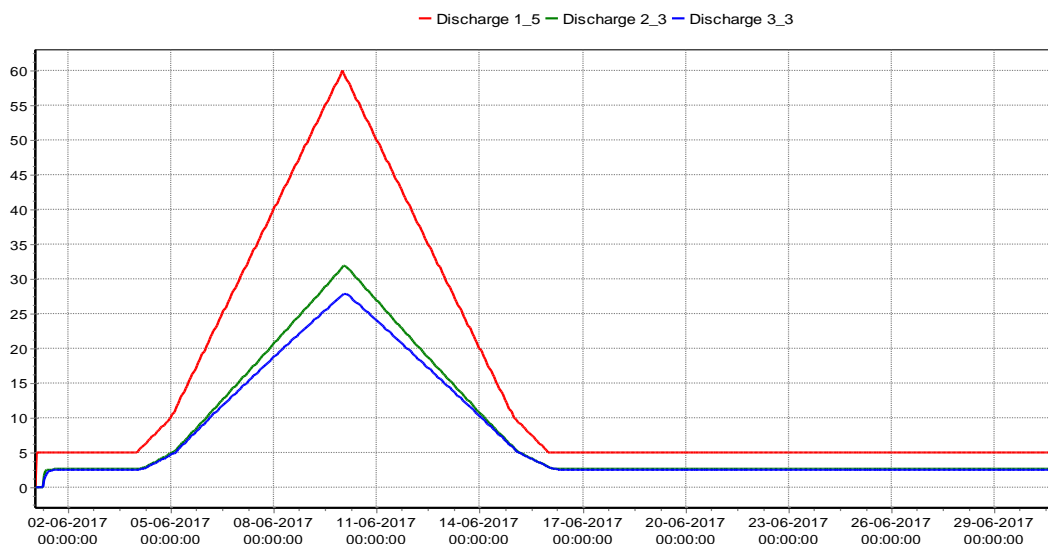
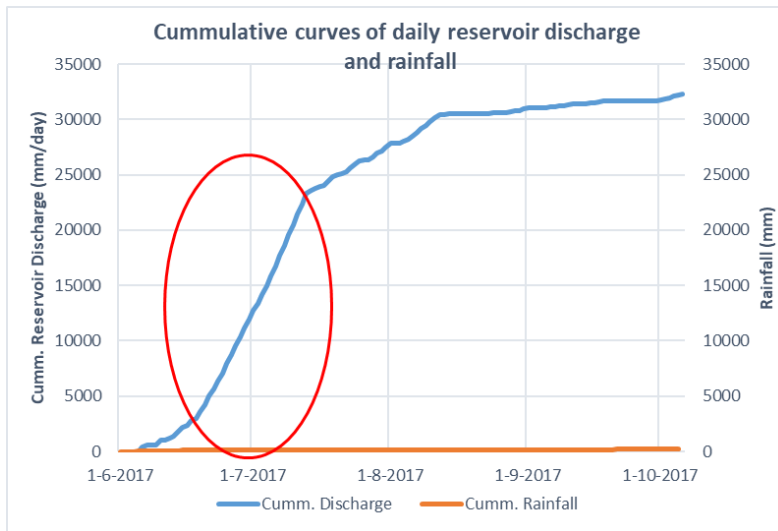


Figure 5-17: Graph showing the response of the model to 1D unsteady flow test

**5.4.2. Boundary conditions**

The first question of the study sought to find out the driver to the flooding in the area. For this purpose, cumulative curves of the daily reservoir discharge and rainfall were examined as illustrated in *Figure 5-18*. The results showed that the reservoir discharges could be incessant for several weeks. The cumulative reservoir discharges increased steadily over a period of three and half weeks as indicated by the red ellipse. Meanwhile, the observed response in the cumulative rainfall curve for the same period was insignificant. The section of the graph marked with the red ellipse was the identified flood window as shown in *Figure 5-19* of the time series of the daily reservoir discharges. The amount of rainfall recorded during the period of high continuous reservoir discharge was insignificant. Therefore, rainfall effect was assumed negligible in this case, hence ignored in the inflow estimation. In that regard, the reservoir discharge was solely considered inflow boundary condition to the model domain.



*Figure 5-18: Cumulative curves of daily reservoir discharge and rainfall of the study area*

As stated earlier in the data processing, the reservoir discharges were estimated by using the reservoir level data and discharge curves. *Figure 5-19* shows the daily estimated discharges from the reservoir. The red vertical lines were used to represent the high discharge window that was defined for the flood model simulation. Over this period, an average discharge of 120m<sup>3</sup>/s was continuously discharged from the reservoir for several weeks could lead to extensive flooding of the model domain.

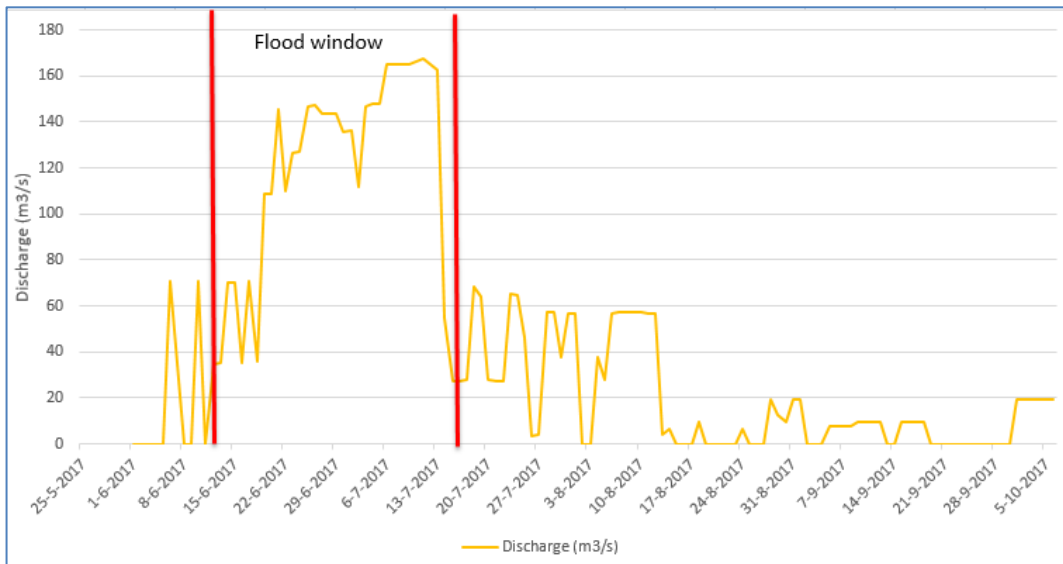


*Figure 5-19: Reservoir daily discharge showing the flood window*

Furthermore, the water levels to define the downstream boundary condition of the model domain was not available. Hence a specified head condition was defined for the model at the outflow to allow a free flow of water from the outlet. The downstream boundary condition was established after the sensitivity analysis and the researcher's knowledge of the area acquired during the fieldwork.

### 5.4.3. Sensitivity Analysis

The results obtained from the sensitivity analyses of the parameters listed in Table 4-2 are presented in *Figure 5-20*. Both the Manning's coefficient and the upstream boundary condition indicated high sensitivity to model. The outer limits of the parameters as indicated in Table 4-2 were analysed, and an increase of inundation extent was observed in each case. In order to establish detailed effects of the parameter variations on the model out, two roughness values within the predefined range and one of the inflow discharge were additionally simulated. The results of the additional analyses were found to follow a similar trend as the outer limits which affirmed the high sensitivity of these parameters to the model output.

The low limit of the manning's range (0.03) showed little resistance to flow as compared to the high limit (0.1) resulting in less accumulation of water in the model. It can be deduced from *Figure 5-20a* that the roughness is proportional to the area of inundation. That implies that land cover properties such as built-up areas with relatively high roughness retain a high volume of water which consequently influence the depth of inundation. Moreover, *Figure 5-20b* indicated that the model is highly sensitive to the upstream boundary condition. The sensitivity of the inflow is instigated by how much water is taken out of the model from the downstream boundary condition. The hydraulic gradient of the downstream discharge effected the propagation of inundation extent caused by the inflow. Consequently, the upstream flow showed high sensitivity to the model.

However, in the case of this model, the downstream boundary condition was found to be insensitive. No change in inundation extent was observed after running the model for the outer range limits. However, an additional internal value (0.8m AD) was simulated to find out if the model would respond differently from the model response of the outer limits. Likewise, the model showed no response to the internal value. The inundation extent remained the same to the extent obtained from the outer limits as illustrated in *Figure 5-20c*. A second sensitivity test was analysed for the downstream boundary condition using a relatively low inflow. In this case, the average discharge value (50m<sup>3</sup>/s) of the discharge time series data was used for the analysis. The downstream boundary showed an identical response as the first downstream boundary condition test. The orange line illustrates the response of the second sensitivity test of the downstream boundary condition in *Figure 5-20c*. The observe insensitivity of the downstream boundary condition can be explained by referring to the St Venant equations of hydrodynamics of the model domain in *subsection 4.3.1.1*. The hydraulic gradient at the downstream was found to be relatively low, which caused a back water flow at the outlet.

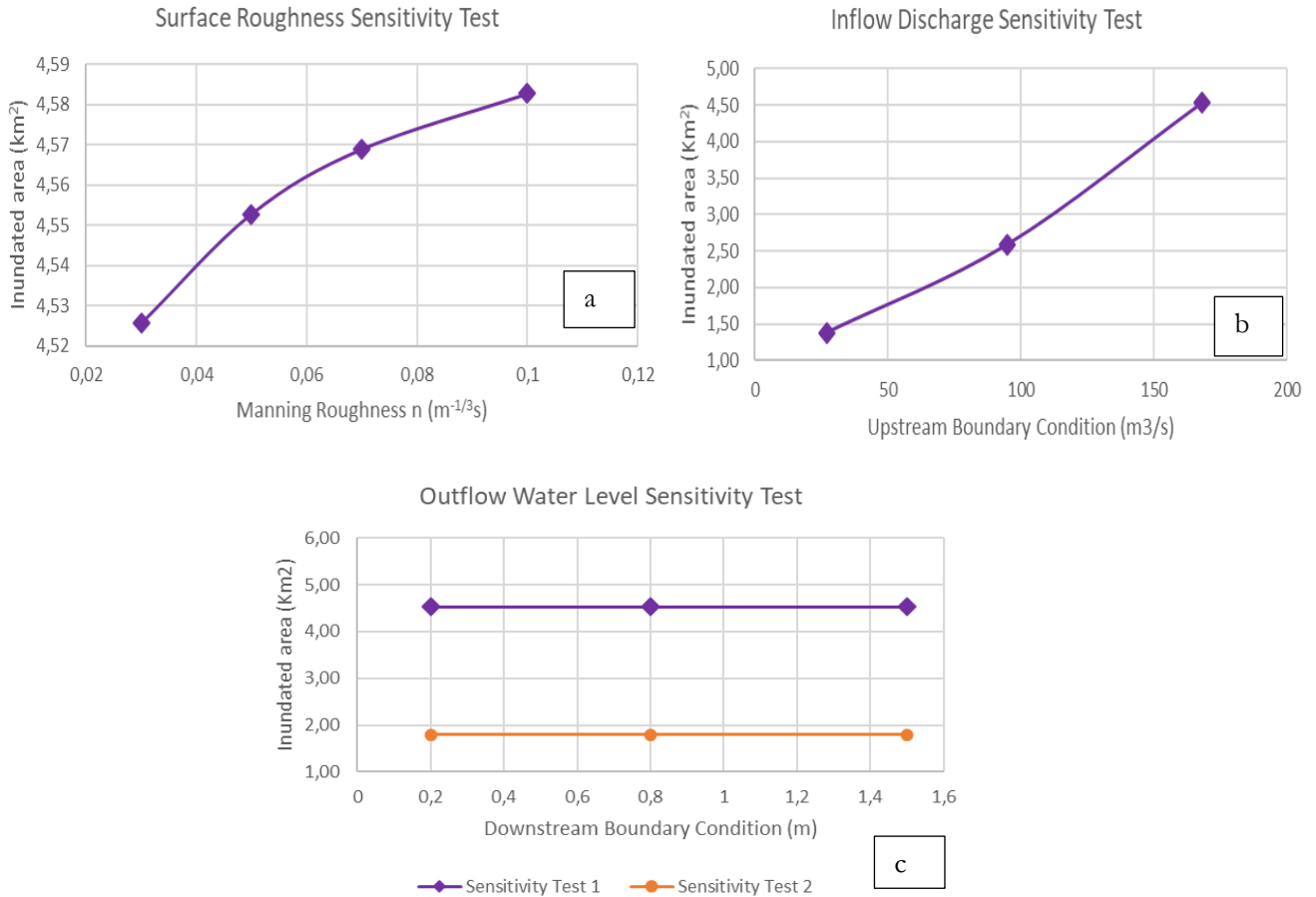


Figure 5-20: Graphical representation of the sensitivity analysis

#### 5.4.4. Model Results

The results of the flood simulation of 25/06/2017, 07/07/2017 and 14/07/2017 are shown in *Figure 5-21*, *Figure 5-22* and *Figure 5-23* respectively. These results show that main part of the model downstream become inundated. These results suggest that there could be backwater effect at the outlets, due to the low water level gradient observed at the downstream. However, the model results were analysed spatially to determine the plausibility of the results. The simulated flood extent seemed plausible by observing flood extent with reference to land properties such as roads. Most often, roads are constructed at relatively high elevations above drainage elevations. Therefore roads could serve as barriers to the flood dispersion as indicated with arrows in *Figure 5-21*. Hence the flood spread to the left of the river channel with relative low elevation. Moreover, the water depths on flooded roads and areas near the roads were observed to be shallow, that is observed to be less than 0.5m above the domain level.

Although the inundation extents seemed plausible, the simulated flood depths at the outlet of the left reach (as indicated by the red circles) in all the simulated results seemed excessive with flood depths  $>1.5m$  above model domain level. Then again, the inundation depths observed in the simulated results presented below could have been instigated the relatively low elevation representation at the outlet. Unfortunately, no GPS measurement was taken in this area to enhance the elevation differences. It is possible, therefore, that the DEM elevation in this area may not have accurately represented the elevations of this area. Moreover, the model domain is bounded to the south by the Densu delta, which could suggest a possible increase in water level at the downstream, thus contributing to a high flood depth at this location.

Interestingly, high water depth of  $>2\text{m}$  above domain level was observed along the river course. It is possible that the friction resistance of the shrub vegetation along the river course restricted the flow, thus accumulating higher depths. Furthermore, the simulated results showed contiguity in the inundated cells. That was because the vertical structures such as buildings were not incorporated into the topographical representation of the model domain. Therefore, no vertical structures obstructed the flow computation from one cell to the other. Hence the continuous simulation extents observed in the simulated results.

The major challenge encountered in the model simulation was the long computation time which lasted several days. Due to this, the simulation of the discharge (i.e. three and half weeks) as determined in flood window could not be simulated within the time span of this research. Instead, simulations were sectioned into three day simulation periods for the flood simulation period. The SOBEK software stored a restart file for each simulated period that served to initialise the model for the follow-up simulations. The restart file stored the model simulation results of the last simulation.

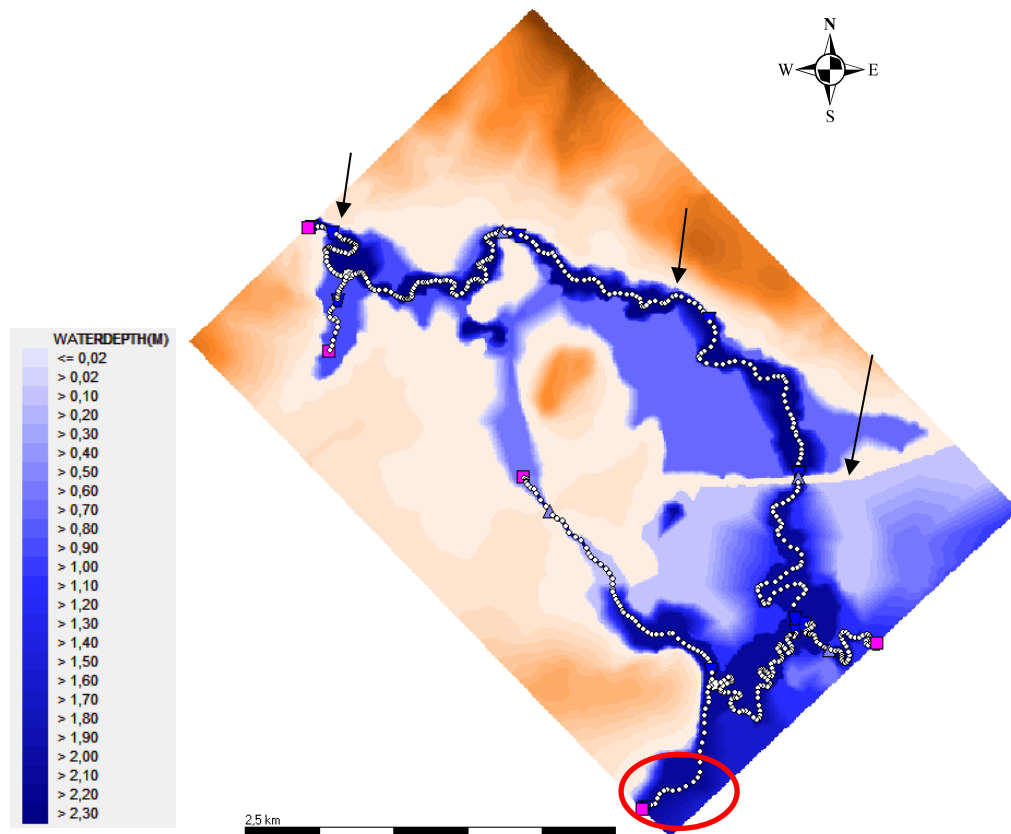


Figure 5-21: Simulated flood extent on the 25/06/2017 (18:00:00)



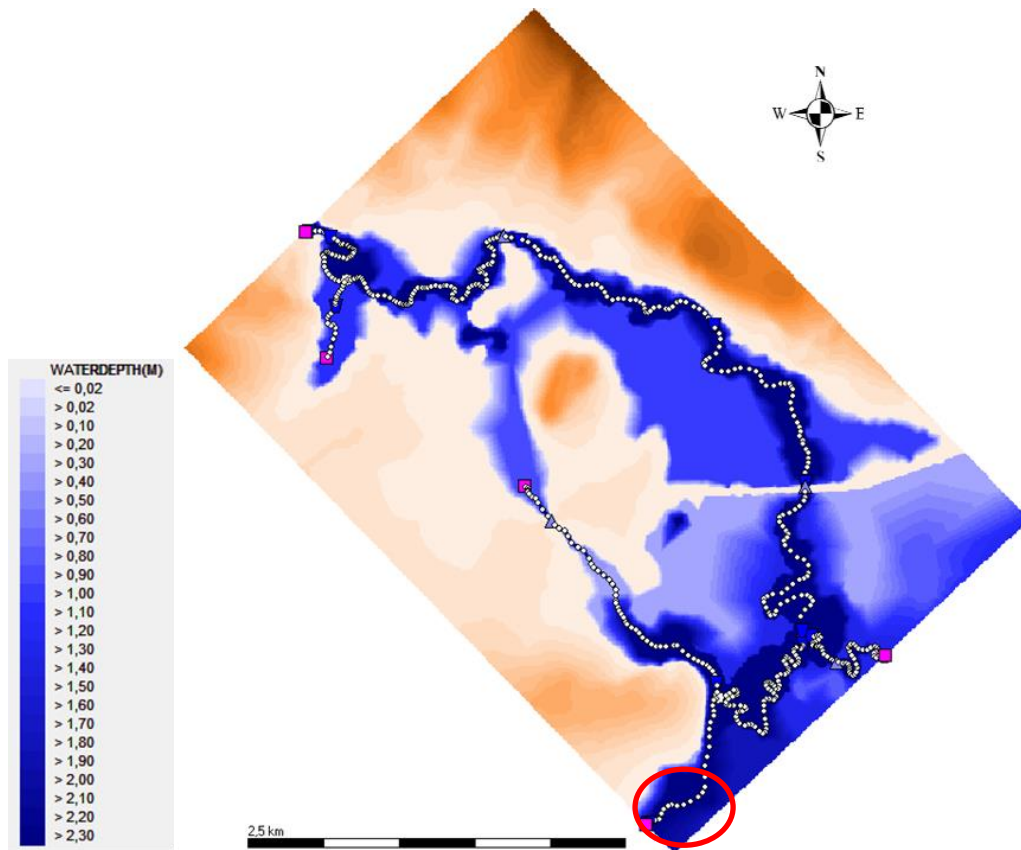


Figure 5-22: Simulated flood extent on the 07/07/2017 (18:00:00)

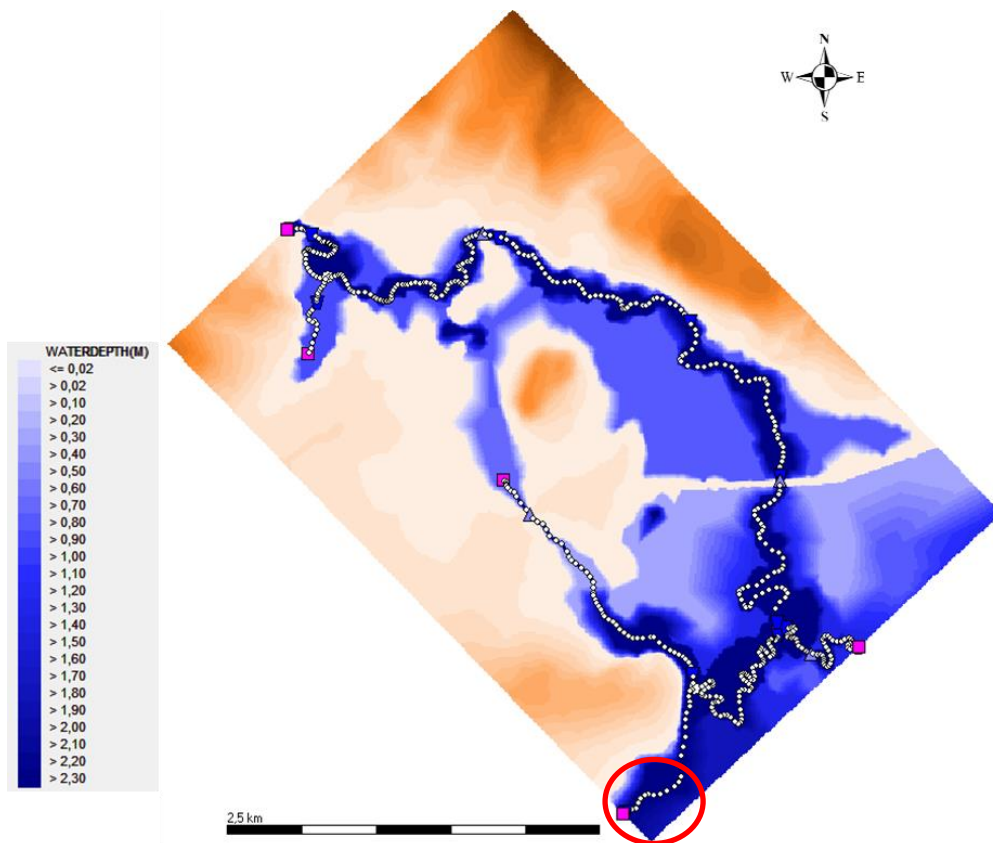


Figure 5-23: Simulated flood extent on the 14/07/2017 (08:00:00)



## 5.5. Comparison of Model Results and Satellite Data

The study aimed to analyse if satellite flood extent could serve for hydrodynamic model calibration in an urban area. In fact, it is undeniable that the simulated output of the hydrodynamic model in a limited data area may be uncertain. However, the systematic approach of the model setup and testing, as well as evaluation of the available data provided some level of credibility of the model output. Obviously, satellite data observation and abstraction were equally associated with some degree of uncertainties. Nevertheless, analysing the suitability of the satellite inundation extent could serve for model calibration purposes would be determined by a close match of the simulated flood extent and the satellite inundation extent. Essentially, the high match between the simulated and satellite flood areas would imply a good possibility for the satellite data to serve for calibration purposes.

Inundation detected from both Sentinel-1 and PlanetScope images were compared with the simulated results of the SOBEK hydrodynamic model. The satellite data used were the Sentinel-1 SAR images captured on the 25/05/2017 and 07/07/2017 at 18:17:47 and PlanetScope optical images captured on 25/06/2017 and 14/07/2017 at 07:57:12. So then the simulated extent of the image dates and the simulated time of 18:00:00 and 08:00:00 were extracted for comparison of the Sentinel-1 and the PlanetScope respectively.

A pixel by pixel based comparison was performed in ArcGIS, and the results including the goodness of fit are presented **Table 5-1**. From the table, the overall match between the simulated and the Sentinel-1 inundation is extents of both VH and VV polarisation was found to be a little above 50%. The VV polarisation had a relatively higher match to the simulated inundation than the VH polarisation. In addition, the maps in *Figure 5-24* and *Figure 5-25*, exhibited relative high match of inundation in the vegetation along the river than the urban area. The overall match of the Sentinel-1 detected inundation extents were contrary to results of Twele et al. (2016), who obtained about 90% accuracy in their analysis. Then again, the study of Twele et al. (2016) was conducted in a vegetated area, different to this study which was situated in an urban area. That notwithstanding, these results in this study yielded similar (initial) results obtained by Mason et al. (2014) in an urban flood detection with SAR before they improved the detected inundation with a developed geometrical optics model.

Table 5-1: Statistical comparison of the satellite data and simulated results

	#Pixels			Area (Km <sup>2</sup> )			Goodness of fit (%)
<b>Sentinel-1 SAR Images</b>							
Images	Model and Satellite	Model only	Satellite only	Model and Satellite	Model only	Satellite only	
25062017_VH_DIFF	34368	28567	1700	3.44	2.86	0.17	53
25062017_VV_DIFF	35578	27357	1827	3.56	2.74	0.18	55
25062017_RATIO_VH	33223	29712	1598	3.32	2.97	0.16	51
25062017_RATIO_VV	37711	25224	1970	3.77	2.52	0.20	58
07072017_VH_DIFF	33727	31615	834	3.37	3.16	0.08	51
07072017_VV_DIFF	35112	30230	964	3.51	3.02	0.10	53
07072017_RATIO_VH	34541	30801	858	3.45	3.08	0.09	52
07072017_RATIO_VV	34774	30568	890	3.48	3.06	0.09	53
<b>PlanetScope Optical Images</b>							
14072017_planetscope	45837	17984	148	4.58	1.80	0.01	72
25062017_planetscope	25129	26871	145	2.51	2.69	0.01	48
<b>Multivariate assessment of both satellite images</b>							
25062017 Ratio VV and 14072017 PlanetScope	58383	5438	2205	5.84	0.54	0.22	88

In a like manner, the PlanetScope optical detected inundation was compared to the simulated model extent. The results obtained from the optical images and model comparison are displayed in **Table 5-1**. The PlanetScope result showed a 72% match with inundation observed on the 14/07/2017 and a 48% match with the inundation observed on the 25/06/2017. The mismatch pixels were found to be the vegetated areas. As can be observed in *Figure 5-26*, the hydrodynamic model simulated the inundation at the vegetated areas where the optical missed as illustrated by the yellow circles. Besides, the continuity of the inundated pixels was effected by other land cover properties such as buildings.

The results also suggested that during the extreme flood, short vegetation such as shrubs and grassland could be completely submerged by water. The submerged vegetation could rather lead to high absorption of the NIR band. In that case, flooded vegetation could be detected with the application of the NDWI. These results help to understand the extent to which the optical data could efficiently be used to extract flood in urban and vegetated areas.

The results of the optical image of 25/06/2017 recorded the lowest match of 48% compared to the simulated model results inundation extent. The portion of the image which overlapped with the simulated extent was analysed. The visual comparison of the optical and simulated extent showed a rather surprising output at the lower left of the model domain. As demonstrated the brown ellipse in *Figure 5-26*, the simulated results showed inundation at this section while the optical completely missed it. Now, turning back to the Sentinel-1 detected inundation of the same day, it was seen that Sentinel-1 detected flood at this location. However, it could be possible that the water depth at the time of the image capture (i.e. 08:00:00) was very shallow contrary to the simulated flood depth. Conversely, since both the SAR and the hydrodynamic model depicted inundation at this area could suggest an artefact in the PlanetScope optical image observation of 25/06/2017.

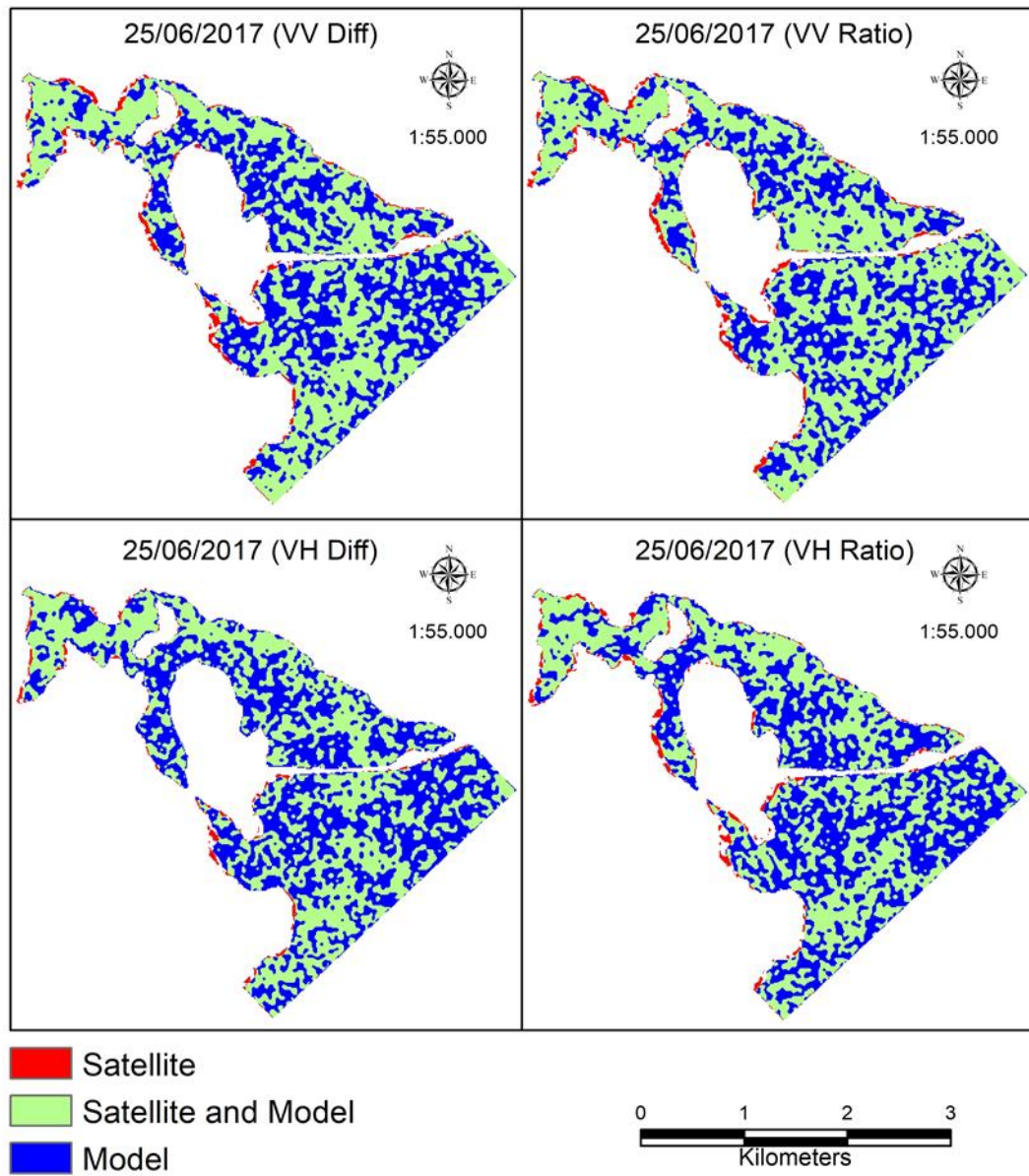


Figure 5-24: Comparison maps of Sentinel-1 and model simulated flood extent (25/06/2017)

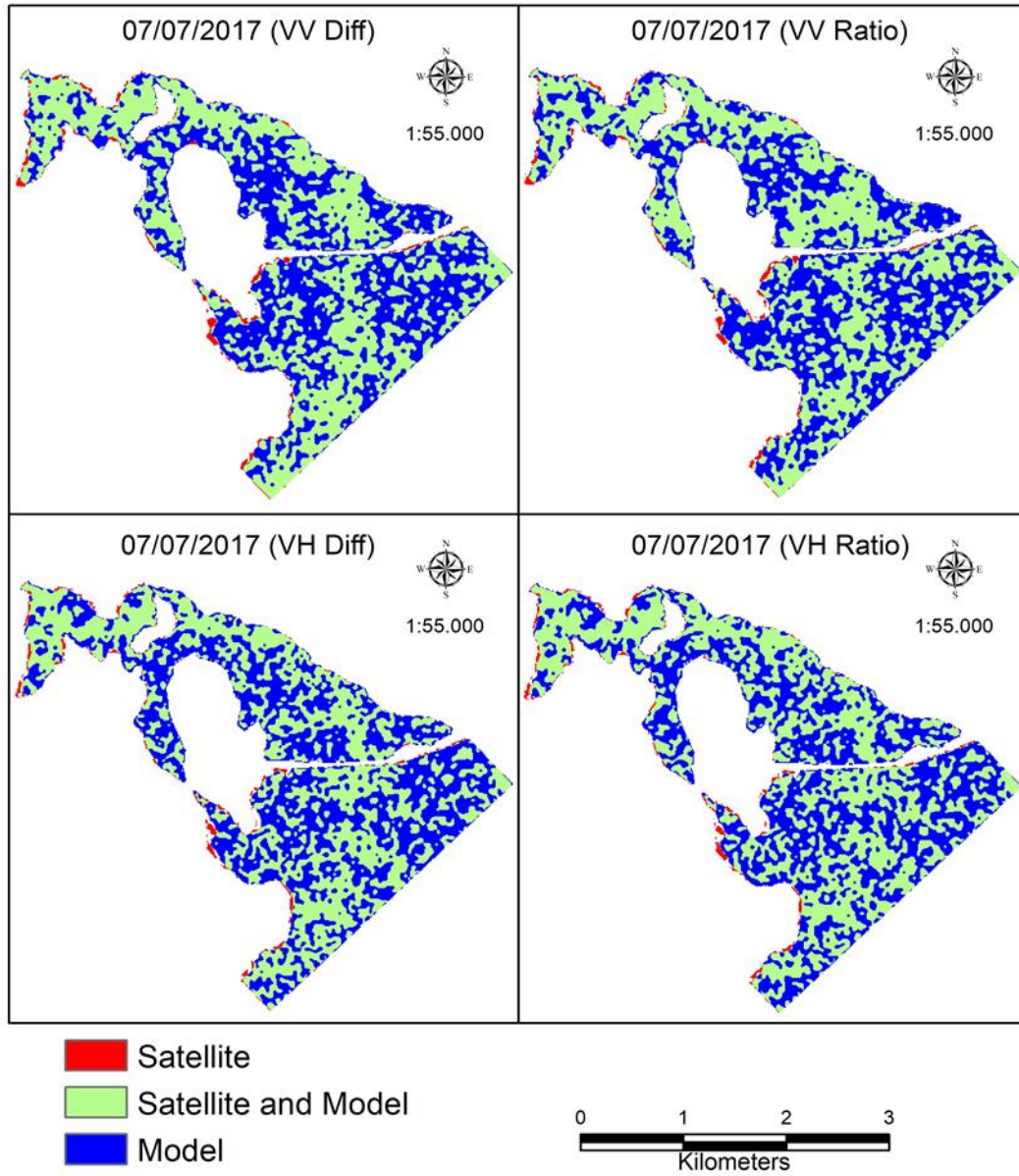


Figure 5-25: Comparison maps of Sentinel-1 and model simulated flood extent (07/07/2017)

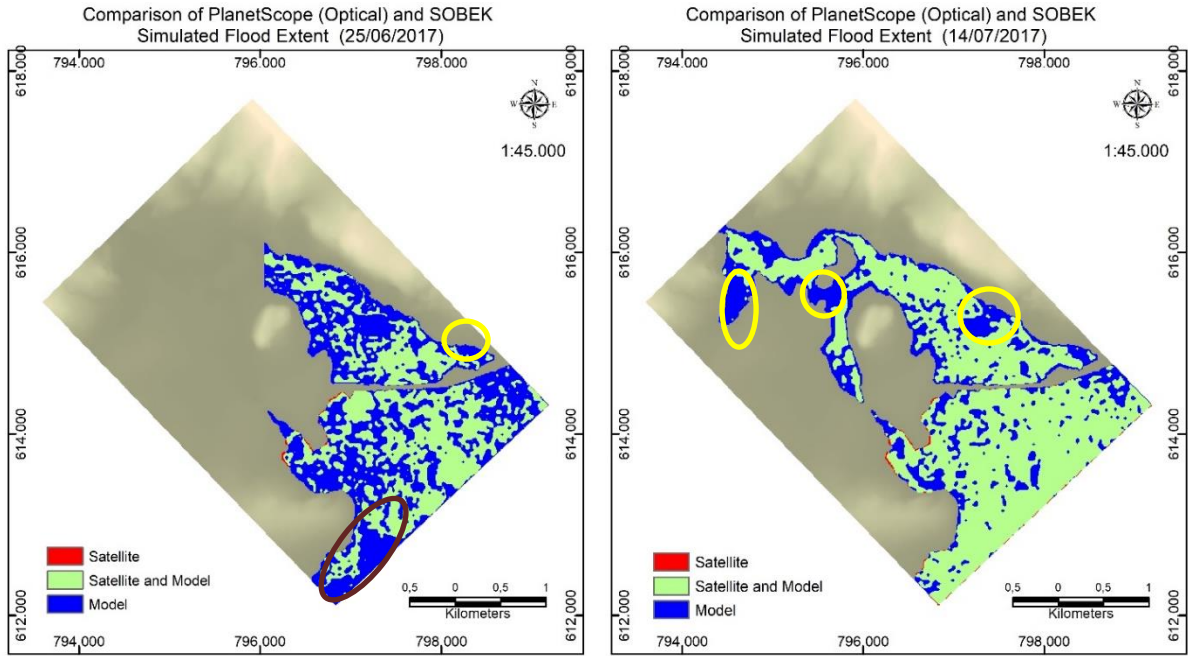


Figure 5-26: Comparison maps of PlanetScope and simulated model extent (25/06/2017)

### 5.5.1. Multivariate Assessment

The best fit from both the Sentinel-1 and the PlanetScope optical images were combined to analyse if both optical and SAR can be integrated to serve for model calibration. The goodness of fit obtained from the multivariate analysis showed improved results from what has been obtained the individual satellite image sources. The result of the combined satellite inundation goodness of fit is presented in **Table 5-1**. And the pixel based comparison is shown in *Figure 5-27*. A relative high match of 88% was achieved with the data integration. The result suggests that combination of both SAR and optical inundation information could be suitable for hydrodynamic model calibration in the limited data area.

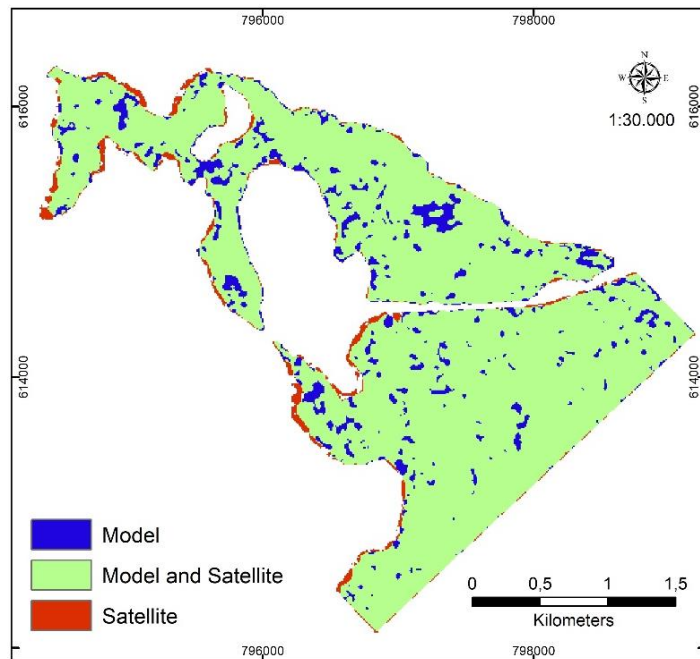


Figure 5-27: Comparison map of the multivariate assessment of satellite and model simulated inundation

### 5.5.2. Possible causes of misfit

The structural arrangement of the buildings and other land cover properties could have influenced detection of flooded pixels by the satellite data. Therefore, the detected inundation extent was observed to be discontinuous pixels. On the contrary, the vertical effect of buildings and other land cover properties were not incorporated into the DEM. For that reason, the simulated inundation extent was observed to be continuous. Hence, the omitted effect of the vertical structures in the topographical data could have increased the area of simulated flood extent. Although the satellite detected inundation was smoothed to improve the inundation continuity across pixels, they were not able to match counterparts by model simulated flood extent.

Besides, vegetation obstructed detection of the inundation using the NDWI of the PlanetScope optical images. Also, the relative high diffuse backscatter intensity of the building roof impeded the minimal changes of backscatter caused by the underlying water in the urban area, making it difficult to detect. These effects limited the inundation extent detected by the satellite images.

It is interesting to note that the HAND adapted approach used for the determine the extent of image analysis did not deviate from the model extent. However, the definition of the height above nearest drainage may have slightly enlarged the extent of analysis of the satellite images, thus the mismatch along the edges. The result of the application of the HAND adapted model as used by Twele et al. (2016), yielded good results for inundation extent as was seen in this study.



## 6. CONCLUSION AND RECOMMENDATION

### 6.1. Conclusion

The main objective of this study was to analyse the suitability of satellite-based flood extent for hydrodynamic model calibration of a limited data area of the Densu floodplain in Accra. Hydrodynamic modelling can be used to understand the hydrodynamic processes of a floodplain and devise water management measures to avert frequent flooding in the urban settlement of the Densu floodplain. Data limitation is main challenge to setting up and calibrating of a hydrodynamic model in this area. For instance, observed flood information required for the calibration of a hydrodynamic flood model is hardly available. This problem motivated the above objective of the study. The two sources of satellite data namely Sentinel-1 SAR and PlanetScope optical images were analysed in this study.

The change detection method of image differencing and image ratio was exploited to detect inundation from the Sentinel-1 SAR images. The inundated areas were segmented by using statistical percentile range threshold of the histograms of the residual difference and ratio images. The results suggested that the changes in backscatter intensity were minimal in the urban area. Due to the minimal changes in backscatter intensity, the percentile range threshold limits of 20-80 was used to detect the inundation from the flooded images. The changes in backscatter observed between the flooded and dry vegetation were relatively higher than in the built-up area. Hence, the detection of flooded vegetation by the change detection method proved to be efficient. Furthermore, it was observed that the VV polarisation detected more inundation extent than the VH polarisation.

The NDWI was used to detect inundation from the PlanetScope images. The findings revealed that cloud cover and vegetation cover obscured the detection of inundation with the application of the NDWI. For instance, inundated wetland and ponds relatively close to the drainage were not detected due to the influence of vegetation. As a result, the area of inundation detected from the application of the NDWI seemed to have underestimated the inundation extent. Cloud shadows and light clouds which could not be masked out of the image were seen to have had high NDWI values signifying water. These areas could have overestimated the extent of inundation. However, in this case, these areas were found within the inundated area. As a result, its effect did not greatly affect the detected inundation. The results also revealed that the NDWI of buildings could be positive (i.e. 0 to 0.1) and therefore, inundation mapping in urban areas was retrieved with NDWI values greater than 0.1.

The 1D2D SOBEK hydrodynamic model was set up in a limited data domain of the densely built-up settlement area in Accra. The model was schematized and well tested to provide some level of credibility to the simulated output. The tests (specifically the 1D steady flow) were used to find, and correct artefacts in the model set up. Thus, the erratic behaviour in the channel flow and the error in the channel slope were identified and corrected.

The upstream boundary condition was estimated from the reservoir daily discharges. It was established that the reservoir discharges more often than not resulted in the flood of the domain. From the cumulative graphs of rainfall and reservoir discharge, it illustrated that the continuous discharge of the reservoir showed by the linear increase in the discharges resulted in the downstream flood. The Dirichlet boundary condition was used to parameterize a free flow condition at the outflow boundary condition in the model. However, the low water level gradient at the downstream caused backwater effect in the model instigating flooding in the model domain. Nevertheless, the downstream boundary condition proved to be fairly insensitive to the model as established by sensitivity analysis. In consequence, the high reservoir discharges coupled with the backwater effect at the outlet was found to be the driver of the flood in the domain.

The effect of the land cover changes to the model was assessed through the sensitivity analysis. The sensitivity analysis revealed further that changes in land cover roughness had a significant effect on the simulated inundation extent. That is to say; low roughness values (e.g. 0.03) exerted less resistance to flow which resulted in a smaller area of inundation than for high roughness values (e.g. 0.1). Furthermore, the resistance of the vegetation along the river contributed to the relatively high water depths observed along the river channel.

The simulated flood extent of the model seemed plausible. This assumption was made based on the information observed in the field. It was observed that roads constructed on relatively high elevation from the drainage heights served as barriers to flood dispersion in the domain. Also, simulated flood depths on inundated roads were found to be shallow. However, the flood depth at the left outlet of the domain seemed excessive (i.e. >1.5m above domain level). The following factors were mentioned as the possible causes of the high flood depth at the left outlet of the model domain. First, the generalisation of elevation at this location, especially since no GPS point was collected at this location for elevation enhancement due to practical reasons. Also, backwater effect at the outlet could result in the high flood depth. However, since the inundation extent and not water depth of the model was not the main element of assessment, it was ignored.

The goodness of fit was the statistical measure employed to assess the suitability of the satellite images for model calibration. Subsequently, the match between the satellite inundation extent and the simulated flood extent was assessed. The results exhibited a poor match between Sentinel-1 inundation extent and the simulated extent. The PlanetScope optical images, on the other hand, show a higher match against the hydrodynamic simulated flood extent. The results from both satellite image sources showed different detection advantages and disadvantages. A multivariate assessment was additionally analysed to evaluate the integration of the two satellite image sources against the simulated extent. The result from this analysis indicated an improved match of 88% goodness of fit between the combined satellite inundation and the simulated extent. That is to say, the integration of different satellite data sources complemented each other to enhance inundation detection in the urban area.

Overall, the findings of the study showed that urban inundation detected from Sentinel-1 SAR images were not very successful. However, based on the clear detection of flooded vegetation, it can be suggested that Sentinel-1 SAR inundation mapping in vegetated areas could be used for the calibration of hydrodynamic models of vegetated and open water inundation. The results from the optical image, however, portrayed greater advantage of the urban inundation detection for model calibration than SAR. Nevertheless, the optical inundation information detected was affected by vegetation and cloud cover. The combination of the SAR and optical images showed satisfactory results of the goodness of fit to the simulated extent. It suggested therefore that both SAR and optical inundation information can be integrated for hydrodynamic model calibration in the limited data areas.

This study and the methods used is the first of its kind in Ghana, to ascertain how satellite data can be used to support hydrodynamic model calibration in data-scarce areas. This study contributes to the existing knowledge on the extent to which satellite data can be used to support hydrodynamic modelling. Moreover, it provides a comprehensive assessment of Sentinel-1 SAR inundation detection in urban areas and contributes to the understanding of change detection method applied for SAR inundation mapping. The study provides insight into the limitations of both optical and SAR images for urban flood monitoring and adds to the growing investigation of research that attempts to integrate satellite data to support hydrodynamic modelling.



## 6.2. Recommendation

The major problem of this study was limited availability of observed data for the model setup and calibration. For that reason, the model could not be calibrated and validated for the satellite evaluation. The researcher acknowledged the uncertainty associated with the model output. Additionally, the channel bottom profile could not be represented in detail due to constraints beyond the capability of the researcher for a regular interval measurement of the cross-section geometry.

The topography of the model domain was flat, and the digital contour could not represent small variations in elevation, which could have influenced the flood water depth simulated by the model.

In addition, the satellite images acquired for the study were limited due to the longer revisit time, and atmospheric effects (cloud cover limitation) in the case of optical satellite images. Because of these limitations, only two satellite image sources were analysed in the study. The PlanetScope optical images obtained for the analysis had only four bands, as such, not much water extraction indices could be exploited. The following recommendations were made for future studies:

- A full river profile measurements should be measured to obtain the real channel bottom profile of the river channel and its effect on the flow dynamics.
- Different topographic data sources such as high-resolution DTM from drones or detailed GPS survey points measurement over the entire domain to determine the detail flow dynamics of the floodplain. Also, the detailed representation of buildings and roads should be incorporated to prepare DTM over the area.
- Other satellite data sources such as TerraSAR, COSMO-SkyMed, WorldView3, Landsat, Sentinel-2 etc. can be explored to broaden the scope of the satellite inundation analysis for hydrodynamic model calibration.



## LIST OF REFERENCES

---

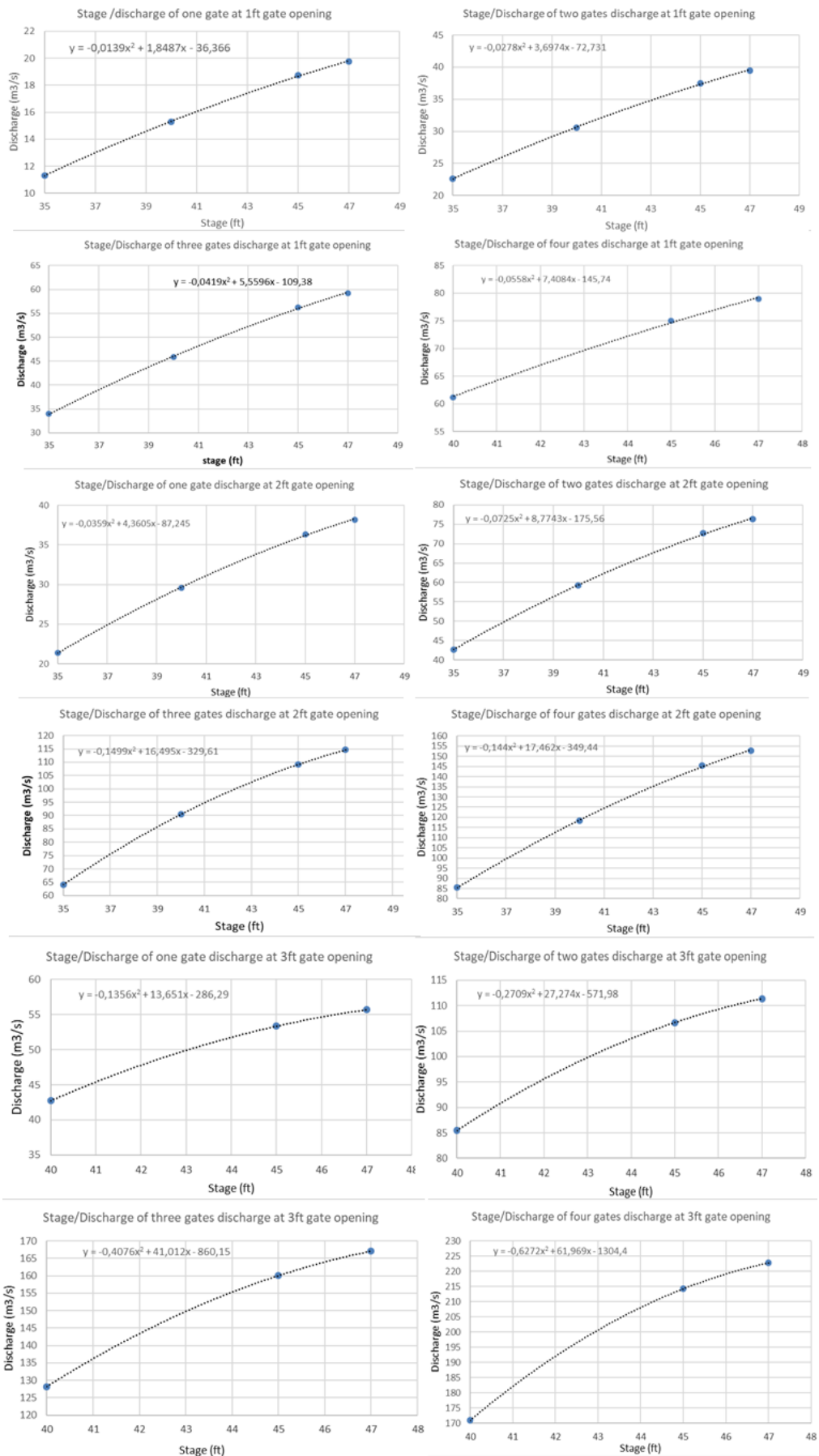
- Alemseged, T. H., & Rientjes, T. H. M. (2007). Uncertainty Issues in Hydrodynamic Flood Modelling. In *Paper presented at the Proceedings of the 5th international symposium on spatial data quality SDQ*. Retrieved from <http://citeseerx.ist.psu.edu/viewdoc/download?doi=10.1.1.221.9252&rep=rep1&type=pdf>
- Ali, H. T. (2016). *Digital Urban Terrain Characterization for 1D2D Hydrodynamic Flood Modelling in Kigali, Rwanda*. Thesis. University of Twente -ITC. Retrieved from [http://www.itc.nl/library/papers\\_2016/msc/wrem/ali.pdf](http://www.itc.nl/library/papers_2016/msc/wrem/ali.pdf)
- Amoako, C., & Frimpong Boamah, E. (2015). The three-dimensional causes of flooding in Accra, Ghana. *International Journal of Urban Sustainable Development*, 7(1), 109–129. <https://doi.org/10.1080/19463138.2014.984720>
- Anders, N., Masselink, R., Keesstra, S., & Suomalainen, J. (2013). High-Res Digital Surface Modeling using Fixed-Wing UAV-based Photogrammetry. Retrieved from <http://geomorphometry.org/system/files/Anders2013geomorphometry.pdf>
- Asumadu-Sarkodie, S., Owusu, P. A., & Rufangura, P. (2015). Impact analysis of flood in Accra, Ghana. *Advances in Applied Science Research*, 53–78. <https://doi.org/10.6084/M9.FIGSHARE.3381460>
- Bao, W.-M., Zhang, X.-Q., & Qu, S.-M. (2009). Dynamic Correction of Roughness in the Hydrodynamic Model. *Journal of Hydrodynamics*, 21(2), 255–263. [https://doi.org/10.1016/S1001-6058\(08\)60143-2](https://doi.org/10.1016/S1001-6058(08)60143-2)
- Bladé, E., Gómez-Valentín, M., Dolz, J., Aragón-Hernández, J. L., Corestein, G., & Sánchez-Juny, M. (2012). Integration of 1D and 2D finite volume schemes for computations of water flow in natural channels. *Advances in Water Resources*, 42, 17–29. <https://doi.org/10.1016/j.advwatres.2012.03.021>
- Brandt, S. A. (2016). Modeling and visualizing uncertainties of flood boundary delineation: algorithm for slope and DEM resolution dependencies of 1D hydraulic models. *Stochastic Environmental Research and Risk Assessment*, 30(6), 1677–1690. <https://doi.org/10.1007/s00477-016-1212-z>
- Clement, M. A., Kilsby, C. G., & Moore, P. (2017). Multi-temporal synthetic aperture radar flood mapping using change detection. *Journal of Flood Risk Management*, 1–17. <https://doi.org/10.1111/jfr3.12303>
- Craciunescu, V., Flueraru, C., & Stancalie, G. (2010). The Usage Of The Historical Cartographic Datasets And The Remote Sensing Data For The Better Understanding And Mapping Of The 2006 Danube Floods In Romania. *Acta Geod. Geoph. Hung*, 45(1), 112–119. <https://doi.org/10.1556/AGeod.45.2010.1.16>
- Crispino, G., Gisonni, C., & Iervolino, M. (2015). Flood hazard assessment: comparison of 1D and 2D hydraulic models. *International Journal of River Basin Management*, (153–166). <https://doi.org/10.1080/15715124.2014.928304>
- Deltares. (2017). *SOBEK user manual, 1D/2D modelling suite for integral water solutions*. Deltares. Delft: Deltares. Retrieved from [https://content.oss.deltares.nl/delft3d/manuals/SOBEK\\_User\\_Manual.pdf](https://content.oss.deltares.nl/delft3d/manuals/SOBEK_User_Manual.pdf)
- Di Baldassarre, G., Schumann, G., & Bates, P. D. (2009). A technique for the calibration of hydraulic models using uncertain satellite observations of flood extent. *Journal of Hydrology*, 367, 276–282. <https://doi.org/10.1016/j.jhydrol.2009.01.020>
- Di Baldassarre, G., Schumann, G., Brandimarte, L., & Bates, P. (2011). Timely Low Resolution SAR Imagery To Support Floodplain Modelling: a Case Study Review. *Surv Geophys*, 32(3), 255–269. <https://doi.org/10.1007/s10712-011-9111-9>
- El-Zaart, A. (2015). Synthetic Aperture Radar Images Segmentation Using Minimum Cross- Entropy with Gamma Distribution. *An International Journal (SIPIJ)*, 6(4). <https://doi.org/10.5121/sipij.2015.6402>
- Elkhrachy, I. (2017). Vertical accuracy assessment for SRTM and ASTER Digital Elevation Models: A case study of Najran city, Saudi Arabia. *Ain Shams Engineering Journal*. <https://doi.org/10.1016/j.asej.2017.01.007>
- ESA. (2017). User Guides - Sentinel-1 SAR - Sentinel Online. Retrieved August 9, 2017, from <https://sentinel.esa.int/web/sentinel/user-guides/sentinel-1-sar>
- Fan, Y., Ao, T., Yu, H., Huang, G., & Li, X. (2017). A Coupled 1D-2D Hydrodynamic Model for Urban Flood Inundation. *Advances in Meteorology*, 2017, 1–12. <https://doi.org/10.1155/2017/2819308>
- Frick-Trzebitzky, F., & Bruns, A. (2017). Disparities in the implementation gap: adaptation to flood risk in the Densu Delta, Accra, Ghana. *Journal of Environmental Policy & Planning*, 1–16. <https://doi.org/10.1080/1523908X.2017.1343136>
- Giacomelli, A., Mancini, M., & Rosso, R. (2017). Integration of ERS-1 PRI Imagery and Digital Terrain Models for the Assessment of Flooded Areas. Retrieved August 7, 2017, from <https://earth.esa.int/workshops/ers97/papers/mancini/index-2.html>
- Gichamo, T. Z., Popescu, I., Jonoski, A., & Solomatine, D. (2011). River cross-section extraction from the ASTER global DEM for flood modeling. *Environmental Modelling & Software*, Elsevier. <https://doi.org/10.1016/j.envsoft.2011.12.003>

- Grimaldi, S., Li, Y., Pauwels, V. R. N., & Walker, J. P. (2016). Remote Sensing-Derived Water Extent and Level to Constrain Hydraulic Flood Forecasting Models: Opportunities and Challenges. *Surveys in Geophysics*, 37(5), 977–1034. <https://doi.org/10.1007/s10712-016-9378-y>
- Grimaldi, S., Li, Y., Pauwels, V. R. N., Walker, J. P., Yuan Li, B., Valentijn N Pauwels, B. R., ... Walker, J. P. (2016). Remote Sensing-Derived Water Extent and Level to Constrain Hydraulic Flood Forecasting Models: Opportunities and Challenges. *Surveys in Geophysics*, 37(5), 977–1034. <https://doi.org/10.1007/s10712-016-9378-y>
- Haile, A. T., & Rientjes, T. H. M. (2005). Effects of Lidar Dem Resolution in Flood Modelling: A Model Sensitivity Study for the City of Tegucigalpa, Honduras. In *Laser scanning 2005*. Retrieved from <http://www.isprs.org/proceedings/XXXVI/3-W19/papers/168.pdf>
- Hong, S., Jang, H., Kim, N., & Sohn, H.-G. (2015). Water area extraction using RADARSAT SAR imagery combined with Landsat imagery and terrain information. *Sensors (Basel, Switzerland)*, 15(3), 6652–67. <https://doi.org/10.3390/s150306652>
- Huang, W., Cao, Z., Qi, W., Pender, G., & Zhao, K. (2015). Full 2D hydrodynamic modelling of rainfall-induced flash floods. *Journal of Mountain Science*, 12(5), 1203–1218. <https://doi.org/10.1007/s11629-015-3466-1>
- Karim, F., Petheram, C., Marvanek, S., Ticehurst, C., Wallace, J., & Gouweleeuw, B. (2011). The use of hydrodynamic modelling and remote sensing to estimate floodplain inundation and flood discharge in a large tropical catchment. In *19th International Congress on Modelling and Simulation, Perth, Australia, 12–16 December 2011*. Perth. Retrieved from <http://mssanz.org.au/modsim2011>
- Liu, Q., Qin, Y., Zhang, Y., & Li, Z. (2015). A coupled 1D–2D hydrodynamic model for flood simulation in flood detention basin. *Natural Hazards*, 75(2), 1303–1325. <https://doi.org/10.1007/s11069-014-1373-3>
- Long, S., Fatoyinbo, T. E., & Policelli, F. (2014). Flood extent mapping for Namibia using change detection and thresholding with SAR. *Environmental Research Letters Environ. Res. Lett*, 9(3), 35002–9. <https://doi.org/10.1088/1748-9326/9/3/035002>
- Malinowski, R., Groom, G. B., Heckrath, G., & Schwanghart, W. (2017). Do Remote Sensing Mapping Practices Adequately Address Localized Flooding? A Critical Overview. *Springer Science Reviews*. <https://doi.org/DOI 10.1007/s40362-017-0043-8>
- Malinowski, R., & Schwanghart, W. (2017). Do Remote Sensing Mapping Practices Adequately Address Localized Flooding? A Critical Overview. *Springer Science Reviews*. <https://doi.org/10.1007/s40362-017-0043-8>
- Manavalan, R. (2017). SAR image analysis techniques for flood area mapping - literature survey. *Earth Science Informatics*, 10(1), 1–14. <https://doi.org/10.1007/s12145-016-0274-2>
- Mani, P., Chatterjee, C., & Kumar, R. (2014). Flood hazard assessment with multiparameter approach derived from coupled 1D and 2D hydrodynamic flow model. *Natural Hazards*, 70(2), 1553–1574. <https://doi.org/10.1007/s11069-013-0891-8>
- Mansourpour, M., Rajabi, M. A., & Blais, J. A. R. (2006). EFFECTS AND PERFORMANCE OF SPECKLE NOISE REDUCTION FILTERS ON ACTIVE RADAR AND SAR IMAGES, 6. Retrieved from <http://citeseerx.ist.psu.edu/viewdoc/download?doi=10.1.1.97.1354&rep=rep1&type=pdf>
- Manyifika, M. (2015). *Diagnostic assessment on urban floods using satellite data and hydrologic models in Kigali, Rwanda*. Thesis. University of Twente Faculty of Geo-Information and Earth Observation (ITC). Retrieved from [http://www.itc.nl/library/papers\\_2015/msc/wrem/manyifika.pdf](http://www.itc.nl/library/papers_2015/msc/wrem/manyifika.pdf)
- Marcinkowski, T., & Olszewski, T. (2014). *METHODOLOGICAL TOOL: Usefulness of numerical modelling to assess new offshore disposal sites*. Gdańsk. Retrieved from [http://corpi.ku.lt/ecodump/uploads/files/CP4\\_Methodological Tool Report\\_Final.pdf](http://corpi.ku.lt/ecodump/uploads/files/CP4_Methodological Tool Report_Final.pdf)
- Martinis, S., Kuenzer, C., & Twele, A. (2015). Flood Studies Using Synthetic Aperture Radar Data. *Remote Sensing of Water Resources, Disasters, and Urban Studies*, 145–173. <https://doi.org/doi:10.1201/b19321-10>
- Martinis, S., Kuenzer, C., Wendleder, A., Huth, J., Twele, A., Roth, A., & Dech, S. (2015). Comparing four operational SAR-based water and flood detection approaches. *International Journal of Remote Sensing*, 36, 3519–3543. <https://doi.org/10.1080/01431161.2015.1060647>
- Mason, D. C., Bates, P. D., & Dall'amico, J. T. (2007). Calibration of uncertain flood inundation models using remotely sensed water levels. *Journal of Hydrology*, 368, 224–236. <https://doi.org/10.1016/j.jhydrol.2009.02.034>
- Mason, D. C. C., Giustarini, L., Garcia-Pintado, J., & Cloke, H. L. (2014). Detection of flooded urban areas in high resolution Synthetic Aperture Radar images using double scattering. *International Journal of Applied Earth Observations and Geoinformation*, 28, 150–159. <https://doi.org/10.1016/j.jag.2013.12.002>

- Mason, D. C., Speck, R., Devereux, B., Schumann, G. J.-P., Neal, J. C., & Bates, P. D. (2010). Flood Detection in Urban Areas Using TerraSAR-X. *IEEE Transactions on Geoscience and Remote Sensing*, 48(2), 882–894. <https://doi.org/10.1109/TGRS.2009.2029236>
- McFeeters, S. k. (2013). Using the Normalized Difference Water Index (NDWI) within a Geographic Information System to Detect Swimming Pools for Mosquito Abatement: A Practical Approach. *Remote Sensing*, 5(7), 3544–3561. <https://doi.org/10.3390/rs5073544>
- McFEETERS, S. K. (1996). The use of the Normalized Difference Water Index (NDWI) in the delineation of open water features. *International Journal of Remote Sensing*, 17(7), 1425–1432. <https://doi.org/10.1080/01431169608948714>
- Medeiros, S. C., Hagen, S. C., & Weishampel, J. F. (2012). Comparison of floodplain surface roughness parameters derived from land cover data and field measurements. *Journal of Hydrology*, 452–453, 139–149. <https://doi.org/10.1016/j.jhydrol.2012.05.043>
- Michaud, J. P., & Wierenga, M. (2005). *Estimating Discharge and Stream Flows: A Guide for Sand and Gravel Operators*. Washington: Washington State Department of Ecology. Retrieved from <https://fortress.wa.gov/ecy/publications/documents/0510070.pdf>
- Montanari, M., Hostache, R., Matgen, P., Schumann, G., Pfister, L., & Hoffmann, L. (2009). Calibration and sequential updating of a coupled hydrologic-hydraulic model using remote sensing-derived water stages. *Hydrol. Earth Syst. Sci*, 13, 367–380. Retrieved from [www.hydrol-earth-syst-sci.net/13/367/2009/](http://www.hydrol-earth-syst-sci.net/13/367/2009/)
- Morales-Hernández, M., Murillo, J., Lacasta, A., Brufau, P., & García-Navarro, P. (2014). A conservative strategy to couple 1D and 2D numerical models : application to flooding simulations. In *Proceedings of the International Conference on Fluvial Hydraulics, RIVER FLOW 2014* (pp. 605–613). CRC Press. <https://doi.org/10.1201/b17133-84>
- Patel, D. P., Ramirez, J. A., Srivastava, P. K., Bray, M., & Han, D. (2017). Assessment of flood inundation mapping of Surat city by coupled 1D/2D hydrodynamic modeling: a case application of the new HEC-RAS 5. *Natural Hazards*, 1–38. <https://doi.org/10.1007/s11069-017-2956-6>
- Planet Labs. (2017). PLANET IMAGERY PRODUCT SPECIFICATION. Planet Labs Inc. Retrieved from [https://www.planet.com/products/satellite-imagery/files/Planet\\_Imagery\\_Product\\_Specs.pdf](https://www.planet.com/products/satellite-imagery/files/Planet_Imagery_Product_Specs.pdf)
- Refice, A., Capolongo, D., Pasquariello, G., D’Addabbo, A., Bovenga, F., Nutricato, R., ... Pietranera, L. (2014). SAR and InSAR for flood monitoring: Examples with COSMO-SkyMed data. *IEEE Journal of Selected Topics in Applied Earth Observations and Remote Sensing*, 7(7), 2711–2722. <https://doi.org/10.1109/JSTARS.2014.2305165>
- Rennó De Azeredo Freitas, H., Da, C., Freitas, C., Rosim, S., De, J. R., & Oliveira, F. (2016). Drainage networks and watersheds delineation derived from TIN-based digital elevation models. *Computers and Geosciences*, 92, 21–37. <https://doi.org/10.1016/j.cageo.2016.04.003>
- Rientjes, T. (2015). *Hydrologic modelling for Intergated Water Resource. Lecture notes for surface water stream.*
- Satge, F., Denezine, M., Pillco, R., Timouk, F., Pinel, S., Molina, J., ... Bonnet, M.-P. (2016). Absolute and relative height-pixel accuracy of SRTM-GL1 over the South American Andean Plateau. *ISPRS Journal of Photogrammetry and Remote Sensing*, 121, 157–166. <https://doi.org/10.1016/j.isprsjprs.2016.09.003>
- Schumann, G., Bates, P. D., Horritt, M. S., Matgen, P., & Pappenberger, F. (2009). Progress in integration of remote sensing–derived flood extent and stage data and hydraulic models. *Reviews of Geophysics*. <https://doi.org/10.1029/2008RG000274>
- Schumann, G. J.-P., Bates, P. D., Neal, J. C., & Andreadis, K. M. (2015). Measuring and Mapping Flood Processes. In *Hydro-Meteorological Hazards, Risks and Disasters* (pp. 35–64). Elsevier. <https://doi.org/10.1016/B978-0-12-394846-5.00002-3>
- Shepherd, W., Blanksby, J., Doncaster, S., & Poole, T. (2011). Quantifying the effect of buildings and surface roughness on 2D flood modelling. In *12th International Conference on Urban Drainage, Porto Alegre/Brazil, 11-16 September 2011* (pp. 11–16). Porto Alegre. Retrieved from [https://web.sbe.hw.ac.uk/staffprofiles/bdgsa/temp/12th ICUD/PDF/PAP005301.pdf](https://web.sbe.hw.ac.uk/staffprofiles/bdgsa/temp/12th%20ICUD/PDF/PAP005301.pdf)
- Smith, M. J., Edwards, E. P., Priestnall, G., & Bates, P. (2006). *Exploitation of New Data Types to Create Digital Surface Models for Flood Inundation Modelling*. FRMRC Research report UR3. Retrieved from [https://web.sbe.hw.ac.uk/frmrc/downloads/UR3 signed off.pdf](https://web.sbe.hw.ac.uk/frmrc/downloads/UR3%20signed%20off.pdf)
- Stephens, E. M., Bates, P. D., Freer, J. E., & Mason, D. C. (2012). The impact of uncertainty in satellite data on the assessment of flood inundation models. *Journal of Hydrology*, 162–173. <https://doi.org/10.1016/j.jhydrol.2011.10.040>
- Teng, J., Jakeman, A. J., Vaze, J., Croke, B. F. W., Dutta, D., & Kim, S. (2017). Flood inundation modelling: A review of methods, recent advances and uncertainty analysis. *Environmental Modelling & Software*, 20, 201–216. <https://doi.org/10.1016/j.envsoft.2017.01.006>
- Twele, A., Cao, W., Plank, S., & Martinis, S. (2016). Sentinel-1-based flood mapping: a fully automated

- processing chain. *International Journal of Remote Sensing*, 31(13), 2990–3004.  
<https://doi.org/10.1080/01431161.2016.1192304>
- Van Dijk, E., Van Der Meulen, J., Kluck, J., Straatman, J. H. M., & Hydroconsultant, V. D. (2014). Comparing modelling techniques for analysing urban pluvial flooding. *Water Science & Technology*.  
<https://doi.org/10.2166/wst.2013.699>
- White, L., Brisco, B., Dabboor, M., Schmitt, A., & Pratt, A. (2015). *A collection of SAR methodologies for monitoring wetlands*. *Remote Sensing* (Vol. 7). <https://doi.org/10.3390/rs70607615>
- WRC. (2007). *WATER RESOURCES COMMISSION, GHANA DENSU RIVER BASIN - Integrated Water Resources Management Plan*. Accra.
- Xiong, B., & Chen, J. M. (2012). A change detection measure based on a likelihood ratio and statistical properties of SAR intensity images. *Remote Sensing Letters*, 3(3), 267–275.  
<https://doi.org/10.1080/01431161.2011.572093>
- Xu, H. (2006). Modification of normalised difference water index (NDWI) to enhance open water features in remotely sensed imagery. *International Journal of Remote Sensing*, 27(14), 3025–3033.  
<https://doi.org/10.1080/01431160600589179>

# Appendix A



Stage and Discharge curves of the Weija reservoir for discharge estimation

# Appendix B

Daily reservoir discharges within the flood window

Date	Time	Dam Level (ft.)	Gate opening width (ft.)					Reservoir Discharge (m3/s)
			G1	G2	G3	G4	G5	
13-6-2017	06:00:00	44	0	0	0	0	2	36
14-6-2017	06:00:00	44	0	0	0	2	2	71
15-6-2017	06:00:00	44	0	0	0	2	2	71
16-6-2017	06:00:00	44	0	0	0	2	0	36
17-6-2017	06:00:00	44	0	0	0	2	2	72
18-6-2017	06:00:00	45	0	2	0	0	0	36
19-6-2017	06:00:00	45	0	2	0	2	2	111
20-6-2017	06:00:00	45	0	2	0	2	2	111
21-6-2017	06:00:00	45	0	2	2	2	2	148
22-6-2017	06:00:00	46	0	2	0	2	2	112
23-6-2017	06:00:00	46	0	2	0	3	2	129
24-6-2017	06:00:00	46	0	2	0	2.4	2.7	129
25-6-2017	06:00:00	46	0	2.6	0	3	2.6	149
26-6-2017	06:00:00	46	0	2.6	0	3	2.6	149
27-6-2017	06:00:00	46	0	2.5	0	3	2.5	146
28-6-2017	06:00:00	46	0	2.5	0	3	2.5	146
29-6-2017	06:00:00	46	0	3	0	2.5	2.5	146
30-6-2017	06:00:00	46	0	3	0	2	2.5	138
1-7-2017	06:00:00	46	0	3	0	2	2.5	139
2-7-2017	06:00:00	47	0	2	0	1.5	2.5	114
3-7-2017	06:00:00	47	0	2.5	0	3	2.5	149
4-7-2017	06:00:00	47	0	2.5	0	3	2.5	150
5-7-2017	06:00:00	47	0	2.5	0	3	2.5	150
6-7-2017	06:00:00	47	0	3	0	3	3	168
7-7-2017	06:00:00	47	0	3	0	3	3	168
8-7-2017	06:00:00	47	0	3	0	3	3	168
9-7-2017	06:00:00	47	0	3	0	3	3	168
10-7-2017	06:00:00	47	0	3	0	3	3	169
11-7-2017	06:00:00	47	0	3	0	3	3	170
12-7-2017	06:00:00	47	0	3	0	3	3	168
13-7-2017	06:00:00	46	0	3	0	3	3	165
14-7-2017	06:00:00	46	0	1.5	0	1.5	0	56
15-7-2017	06:00:00	46	0	1.5	0	0	0	28
16-7-2017	06:00:00	46	0	1.5	0	0	0	28
17-7-2017	06:00:00	46	0	1.5	0	0	0	28
18-7-2017	06:00:00	46	0	2	0	0	1.7	69
19-7-2017	06:00:00	46	0	2	0	0	1.5	65
20-7-2017	06:00:00	45	0	0	0	1	0.5	28

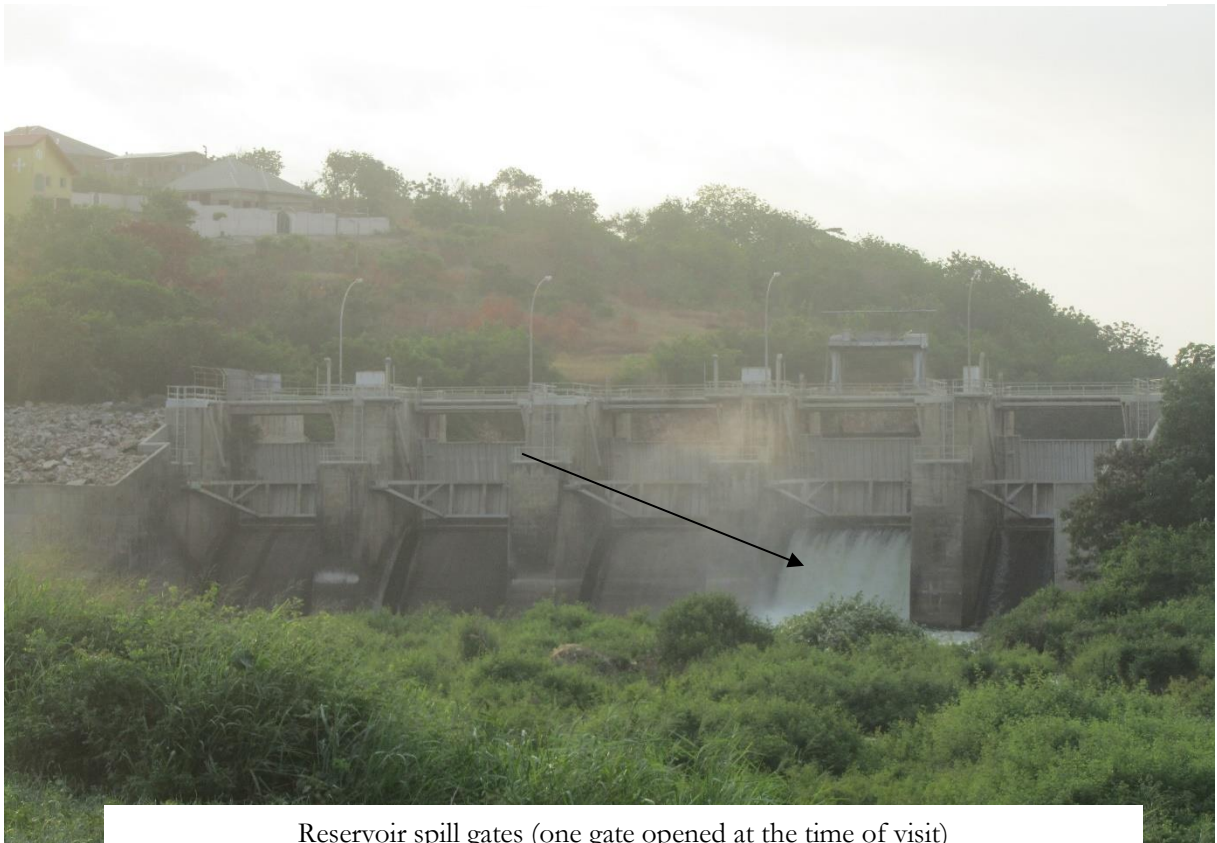


# Appendix C

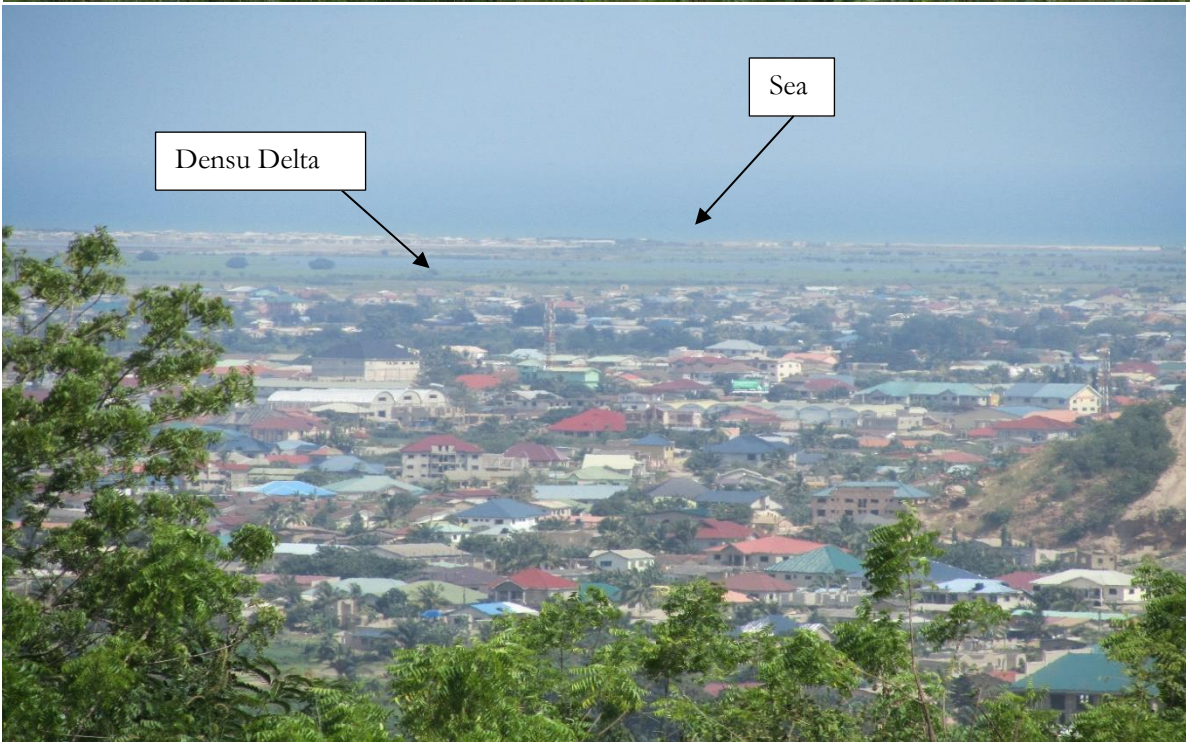
## Field Pictures



Reservoir water level gauge



Reservoir spill gates (one gate opened at the time of visit)



Urban settlement downstream of the reservoir





Sections along the river channel

